

# Suprathermal ion transport in turbulent magnetized plasmas

THÈSE N° 6527 (2015)

PRÉSENTÉE LE 13 FÉVRIER 2015

À LA FACULTÉ DES SCIENCES DE BASE  
CRPP - PHYSIQUE DES PLASMAS DE BASE  
PROGRAMME DOCTORAL EN PHYSIQUE

ÉCOLE POLYTECHNIQUE FÉDÉRALE DE LAUSANNE

POUR L'OBTENTION DU GRADE DE DOCTEUR ÈS SCIENCES

PAR

Alexandre Dominique BOVET

acceptée sur proposition du jury:

Prof. M. Q. Tran, président du jury  
Prof. A. Fasoli, Dr I. Furno, directeurs de thèse  
Prof. P. Ricci, rapporteur  
Prof. F. Skiff, rapporteur  
Prof. F. Zonca, rapporteur



ÉCOLE POLYTECHNIQUE  
FÉDÉRALE DE LAUSANNE

Suisse  
2015



Le véritable voyage de découverte ne consiste pas à chercher de nouveaux paysages,  
mais à avoir de nouveaux yeux.

— Marcel Proust



# Abstract

Suprathermal ions, which have an energy greater than the quasi-Maxwellian background plasma temperature, are present in many laboratory and astrophysical plasmas. In fusion devices, they are generated by the fusion reactions and auxiliary heating. Controlling their transport is essential for the success of future fusion devices that could provide a clean, safe and abundant source of electric power to our society. In space, suprathermal ions include energetic solar particles and cosmic rays. The understanding of the acceleration and transport mechanisms of these particles is still incomplete.

Basic plasma devices allow detailed measurements that are not accessible in astrophysical and fusion plasmas, due to the difficulty to access the former and the high temperatures of the latter. The basic toroidal device TORPEX offers an easy access for diagnostics, well characterized plasma scenarios and validated numerical simulations of its turbulence dynamics, making it the ideal platform for the investigation of suprathermal ion transport.

This Thesis presents three-dimensional measurements of a suprathermal ion beam injected in turbulent TORPEX plasmas. The combination of uniquely resolved measurements and first-principle numerical simulations reveals the general non-diffusive nature of the suprathermal ion transport. A precise characterization of their transport regime shows that, depending on their energies, suprathermal ions can experience either a superdiffusive transport or a subdiffusive transport in the same background turbulence. The transport character is determined by the interaction of the suprathermal ion orbits with the turbulent plasma structures, which in turn depends on the ratio between the ion energy and the background plasma temperature.

Time-resolved measurements reveal a clear difference in the intermittency of suprathermal ions time-traces depending on the transport regime they experience. Conditionally averaged measurements uncover the influence of field elongated turbulent structures, referred to as blobs, on the suprathermal ion beam.

A theoretical model extending the Brownian motion to include non-Gaussian (Lévy) statistics and long-range temporal correlation is developed. This model successfully describes the evolution of the radial particle density from the numerical simulations and provides information on the microscopic processes underlying the non-diffusive transport of suprathermal ions.

Key words: plasma physics, astrophysics, nuclear fusion, turbulence, transport, suprathermal ions, fast ions, ion beam, blobs, non-diffusive transport, superdiffusion, subdiffusion, anomalous transport, continuous time random walk, Lévy flight, Lévy walk, fractional Lévy motion,

---

fractional derivatives, intermittency

# Résumé

Les ions suprathermiques, qui ont une énergie supérieure à la température du plasma d'arrière-plan, sont présents dans de nombreux plasmas de laboratoires et d'astrophysique. Dans les dispositifs de fusion, ils sont générés par les réactions de fusion et par le chauffage auxiliaire. La maîtrise de leur transport est essentielle pour le succès des futurs réacteurs à fusion qui pourraient fournir une source d'énergie électrique propre, sûre et abondante notre société. Dans l'espace, les ions rapides comprennent les particules solaires énergétiques et les rayons cosmiques. La compréhension des mécanismes de leur accélération et de leur transport est encore incomplète.

Les machines à plasmas de base permettent des mesures détaillées qui ne sont pas possibles dans les plasmas d'astrophysique et de fusion à cause de la difficulté d'accès des premiers et des températures élevées des seconds. La machine toroïdale de base TORPEX offre à la fois un accès facile aux diagnostics, des scénarios de plasmas bien caractérisés et des simulations de turbulence validées. Cela en fait la plate-forme idéale pour l'étude du transport des ions suprathermiques.

Dans cette Thèse, des mesures tridimensionnelles d'un faisceau de ions injecté dans les plasmas turbulents de TORPEX sont présentées. La nature généralement non-diffusive du transport des ions suprathermiques est révélée par le truchement de mesures de haute résolution et de simulations numériques basées sur des principes premiers. Une caractérisation précise du régime de transport montre que, selon leur énergie, les ions suprathermiques subissent soit un transport supra-diffusif, soit un transport sous-diffusif, dans le même plasma d'arrière-plan. Le caractère du transport est déterminé par l'interaction des orbites des ions avec les structures turbulentes du plasma. L'importance de cette interaction dépend du rapport entre l'énergie des ion et la température du plasma.

Des mesures résolues dans le temps révèlent une différence claire dans l'intermittence des traces temporelles des ions selon le régime du transport qu'ils subissent. Des mesures moyennées conditionnellement montrent l'influence des structures turbulentes allongées le long des lignes de champs, appelées blobs, sur le faisceau de ions suprathermiques.

De plus, un modèle théorique qui généralise le mouvement Brownien pour y inclure une statistique non-Gaussienne (de Lévy) et des corrélations temporelles à longue distance est développé. Ce modèle décrit correctement l'évolution de la densité radiale de particule calculée avec les simulations numériques et délivre des informations sur les processus microscopiques sous-jacents au transport non-diffusif des ions suprathermiques.

---

Mots clefs : physique des plasmas, astrophysique, fusion nucléaire, turbulence, transport, ions suprathermiques, ions rapides, faisceau de ion, blob, transport non-diffusif, supra-diffusion, sous-diffusion, transport anormal, marche aléatoire en temps continu, vols de Lévy, marche de Lévy, mouvement fractionnaire de Lévy, dérivées fractionnaires, intermittence

# Contents

<b>Abstract (English/Français)</b>	<b>v</b>
<b>1 Introduction</b>	<b>1</b>
1.1 Plasma and fusion reactions . . . . .	1
1.2 Plasma confinement and fusion devices . . . . .	3
1.3 Suprathermal ions . . . . .	5
1.4 Transport of suprathermal ions . . . . .	6
1.5 Motivation and outline . . . . .	7
<b>2 Experimental setup</b>	<b>11</b>
2.1 TORPEX device . . . . .	11
2.1.1 Plasma production . . . . .	12
2.1.2 Main diagnostics . . . . .	13
Langmuir probe theory on TORPEX . . . . .	14
Triple probe on TORPEX . . . . .	16
2.1.3 Turbulence regimes . . . . .	16
2.2 Production and detection of suprathermal ions . . . . .	20
2.2.1 Suprathermal ion source . . . . .	21
2.2.2 Suprathermal ion detection . . . . .	24
Gridded energy analyzers . . . . .	24
Synchronous detection of the suprathermal ion current signal . . . . .	27
Gain of the detection chain . . . . .	28
<b>3 Experimental technique</b>	<b>29</b>
3.1 Poloidal cross section of the suprathermal ion current . . . . .	29
3.2 Mean position and standard deviation of the suprathermal ion current profiles	30
3.3 Evaluation of the measurement errors . . . . .	33
3.4 Motion of the suprathermal ions . . . . .	35
3.5 Measurements with and without plasmas . . . . .	38
<b>4 Non-diffusive transport</b>	<b>41</b>
4.1 Classical diffusion and the random walk model . . . . .	42
4.2 Non-diffusive transport . . . . .	45
4.2.1 Continuous time random walk . . . . .	46

## Contents

---

Lévy flight . . . . .	49
Lévy walk . . . . .	50
4.2.2 Langevin approach . . . . .	51
Fractional Brownian motion . . . . .	53
Fractional Lévy motion . . . . .	56
<b>5 Numerical simulations</b>	<b>59</b>
5.1 Fluid simulations of the turbulence . . . . .	59
5.1.1 Comparison of GBS simulations with TORPEX plasmas . . . . .	62
5.2 Suprathermal ion simulation model . . . . .	62
5.2.1 Numerical investigation of the suprathermal ion transport . . . . .	65
5.2.2 Lévy walk description of the suprathermal ion transport in TORPEX . . .	69
5.2.3 Considerations for the comparison with experiment . . . . .	70
5.2.4 Fitting the transport exponent . . . . .	72
<b>6 Fractional Lévy motion analysis</b>	<b>75</b>
6.1 Asymmetric fractional Lévy motion . . . . .	75
6.2 Numerical simulations of suprathermal ions transport in TORPEX . . . . .	77
6.3 Least-squares fit of the radial distribution . . . . .	80
6.3.1 Superdiffusive case . . . . .	80
6.3.2 Subdiffusive case . . . . .	82
6.4 Conclusions . . . . .	83
<b>7 Comparison between experiment and simulations</b>	<b>85</b>
7.1 Experimental and numerical parameters . . . . .	85
7.2 Synthetic diagnostic . . . . .	86
7.3 Comparison of the experiments with the synthetic diagnostic . . . . .	87
7.4 Identification of the transport regimes . . . . .	90
7.5 Discussion . . . . .	92
<b>8 Time-resolved measurements</b>	<b>95</b>
8.1 Experimental set-up for the time-resolved measurements . . . . .	95
8.2 Suprathermal ion current times traces . . . . .	96
8.3 Time-averaged, skewness and kurtosis profiles of the suprathermal ion current	97
8.4 Conditionally averaged suprathermal ion current profiles . . . . .	99
8.5 Analysis of the suprathermal ion beam displacement . . . . .	102
8.6 Conclusions . . . . .	105
<b>9 Conclusions</b>	<b>107</b>
<b>A Stable distributions</b>	<b>111</b>
<b>B Fractional differential operators</b>	<b>113</b>
<b>C GBS simulations</b>	<b>115</b>

<b>D Suprathermal ion collision frequencies</b>	<b>117</b>
<b>Acronyms</b>	<b>119</b>
<b>Repeatedly used symbols</b>	<b>121</b>
<b>Bibliography</b>	<b>135</b>
<b>Acknowledgements</b>	<b>137</b>
<b>Curriculum Vitae</b>	<b>139</b>



# 1 Introduction

## 1.1 Plasma and fusion reactions

The vast majority of the visible matter in the universe is in the state of plasma, the “fourth state” of matter together with solid, liquid and gas. The plasma consists of partially or totally ionized gas creating an ensemble of positively charged ions, negatively charged electrons, and neutral molecules, where collective interactions dominate over binary interactions and which is quasineutral [1]. It is the collective behavior, resulting from the long-range Coulomb force existing between charged particles, which makes the plasma behave in a different, sometimes complex, manner.

Plasma is ubiquitous in space, it fills the space between planets, star systems and galaxy in a very tenuous form such that binary collisions are extremely rare and can be neglected. Solar wind is also made of plasma streaming from the Sun surface and drifting with a typical velocity of 300 km/s and temperature of tens of eVs ( $1 \text{ eV} \approx 11\,000 \text{ K}^\circ$ ) [1]. Stars such as the Sun are also made of extremely dense and hot plasma. For example, the temperature in the core of the Sun is of the order of 1 keV and its density of  $150 \text{ g/cm}^3$  (about 10 times the density of gold). In such conditions, hydrogen ions have very high velocities and collisions between them are frequent. When two ions collide with large enough energy, they can overcome their Coulomb repulsion and get sufficiently close to each other, so that the nuclear attractive force makes them form a new, heavier, nucleus. This process is called fusion reaction. Elements heavier than hydrogen are created within stars or supernovae through this process. All the energy emitted by the Sun that we receive on Earth, is carried by photons released by fusion reactions that took place in the Sun. Fusion reactions provide the energy necessary for life on Earth.

It is less common to find matter in the form of plasma on Earth. A gas at a standard density on Earth becomes ionized only when its temperature reaches values above  $10\,000 \text{ }^\circ\text{C}$ . However, there are spectacular examples of plasmas on Earth, such as auroras that are due to the arrival of solar wind, released by a coronal mass ejection on the Sun, in the magnetosphere of the Earth. Lightnings, flames and the gas inside neon tubes are other examples of plasmas on Earth. Plasmas are also widely used in industry processes, mainly to modify the physical properties



**Figure 1.1** | Examples of plasmas in the Universe. From left to right: an image of the Sun from the Extreme Ultraviolet Imaging Telescope (EIT) installed on the SOHO spacecraft showing a coronal mass ejection event; photograph of aurora australis taken from the International Space Station; Photograph of lightnings.

of surfaces (etching, cleaning, thin layer deposition, etc.). One of the recent applications of plasmas is in medicine, where cold atmospheric plasmas are used to improve wound healing or selectively eradicate cancer cells [2].

Scientists have been thinking to build power plants harnessing fusion energy since the 1920s, when they discovered that the combined mass of four hydrogen nuclei weights more than the mass of one helium atom with four nucleons. This discovery led them to understand the mechanism by which fusion reactions in the Sun release energy. The mass difference between reactants and products of fusion reactions is converted in kinetic energy according to the law  $E = mc^2$ . This mass difference comes from the binding energy of the nuclei, due to the strong nuclear force, which is greater in the combined reactants than in the products. This holds for all atoms as heavy as iron. When heavier atoms than iron fuse, energy is consumed by the reaction and it is the opposite nuclear reaction that releases energy, the fission reaction. In fusion power plants, the fuel is necessarily in the state of a plasma as it has to be sufficiently hot and dense for the fusion reactions to occur frequently and overcome the losses inevitably present. Research in fusion energy started in the 1950s with the invention of the first experiments trying to confine a hot plasma in order to allow the fusion of its nuclei. In a reactor, a simple power balance shows that, not only the temperature and the density have to be sufficiently high, but also the confinement time of the energy has to be long enough.

Many fusion reactions are possible, but the one involving the two hydrogen isotopes, deuterium and tritium, is the one that occurs the most easily at the lowest energy:



The reaction releases an alpha particle ( ${}^4_2\text{He}$ ) and a neutron with very high kinetic energies. A plasma where the fusion reactions are sustained purely by the heating of the alpha particles, i.e. the plasma self-heating, is in a state called *ignition*, this is the case for the plasma inside stars. A fusion reactor does not necessarily need to reach such a state to be economically viable, but

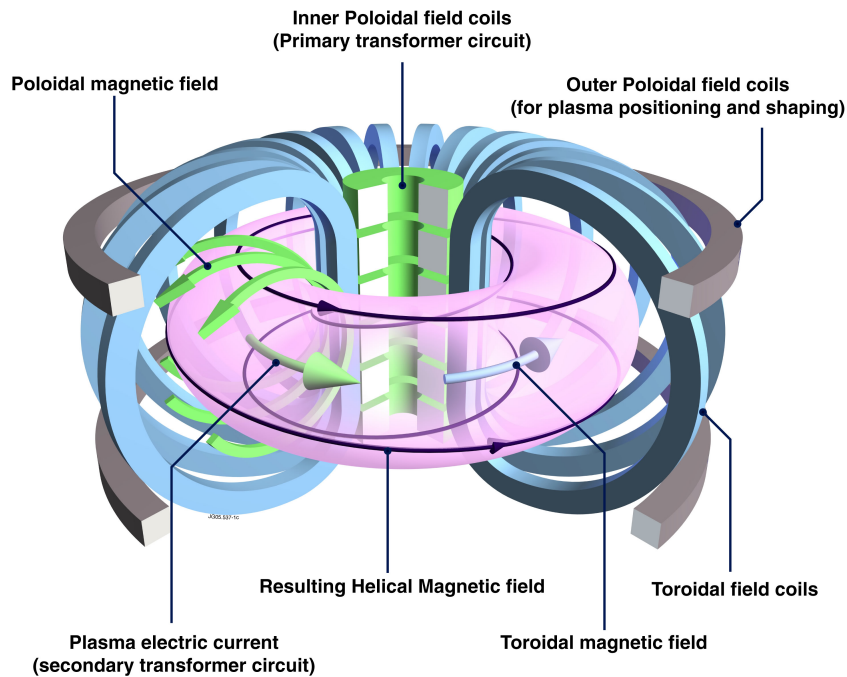


**Figure 1.2** | Schematic view of a tokamak.

the closest it is to ignition, the better. The alpha particles need to be confined during a long enough time so that they can transmit their energy back to the plasma. The power gain factor of fusion reactors is characterized by the ratio,  $Q$ , of the fusion power produced to the power input. This can be expressed as a function of the fraction of the heating power provided by the alpha particles to the total heating power, which comprises the heating provided by auxiliary systems, as [3]

$$Q = 5 \frac{f_\alpha}{1 - f_\alpha} \quad (1.2)$$

For an ignited plasma,  $f_\alpha = 1$  and therefore  $Q = \infty$ . If the self-heating by the alpha particles dominates over other forms of heating, i.e.  $f_\alpha \geq 1/2$ , the plasma is said to be in the *burning plasma regime*. This condition corresponds to  $Q \geq 5$ .

## 1.2 Plasma confinement and fusion devices

In stars, the plasma is confined by its own gravitational pull. The gravitational pull of plasmas created in laboratories is extremely small compared to that of stars and other means must be used to confine the plasma in a vacuum chamber. Inertial confinement aims at compressing and heating a fuel target by creating shock waves symmetrically directed towards its center, usually with the help of high-energy lasers, to initiate fusion reactions [4]. Magnetic confinement uses magnetic fields to trap the charged particles constituting the plasma. Under the influence of the Lorentz force exerted by the magnetic field, charged particles perform a

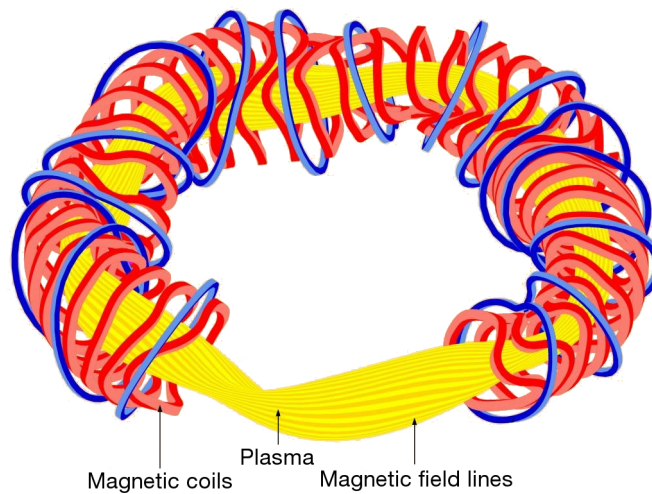


**Figure 1.3** | Schematic view of a stellarator configuration.

circular motion around the magnetic field lines referred as *gyromotion*. A multitude of magnetic configurations have been investigated since the early days of plasma physics research. Linear devices, such as Z-pinch [5],  $\theta$ -pinches [6] or mirror machines [7] have the simplest magnetic configurations but suffer from large losses at the two ends of the open magnetic field lines. Closing the magnetic field lines leads to torus-shaped configurations [8]. Two important versions of devices with a closed magnetic configuration are the tokamak and the stellarator.

In a tokamak, coils surrounding a torus-shaped vacuum vessel create a toroidal and a vertical magnetic field. A toroidal current is induced in the plasma by a set of inner poloidal field coils that act as the primary of a transformer, the secondary being the plasma. The plasma current in turn generates a poloidal magnetic field (i.e. perpendicular to the toroidal direction), which results in helical magnetic field lines (Fig. 1.2). These provide the topological configuration counterbalancing the tendency of particles to drift outside of the tokamak [9]. A stellarator (Fig. 1.3) consists of a vacuum vessel isomorphic to a torus in which a helical magnetic field is created by external coils without inducing a toroidal current in the plasma. While tokamaks are intrinsically pulsed devices due to the fact that the toroidal current is generated by a transformer action, stellarators are steady-state. Wendelstein 7-X (Fig. 1.4), currently under construction in Germany, will be the world's largest fusion device of the stellarator type [10]. It has the objective of investigating the suitability of the stellarator concept for a power plant.

ITER, currently under construction in Cadarache in France, is the result of an intense international collaboration of the controlled fusion research community. The objective of ITER is to provide an integrated demonstration of the scientific and technological feasibility of fusion energy, and of its safety [11]. It will be the largest tokamak ever constructed, with a major radius of 6.2 m and a toroidal magnetic field of 5.3 T. One of the goals of ITER is to attain a fusion gain  $Q \geq 10$  during inductively driven operation and  $Q \geq 5$  during steady-state operation. It will therefore be the first burning plasma ever produced.

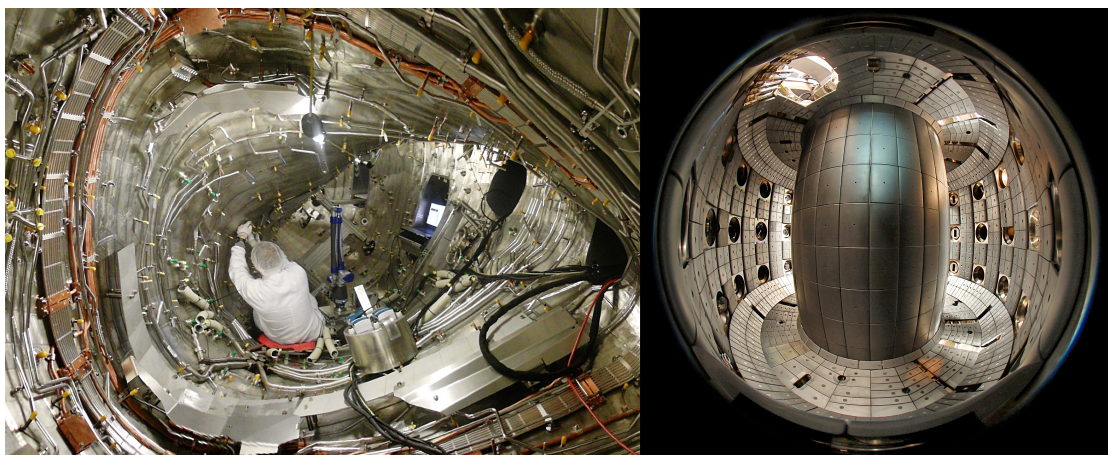


**Figure 1.4** | On the left, photograph of the interior of the stellarator Wendelstein 7-X currently being built in Greifswald, Germany by the Max-Planck-Institut für Plasmaphysik (IPP). On the right, photograph of the interior of the Tokamak à Configurations Variables (TCV) operated at the Centre de Recherches en Physique des Plasmas (CRPP) at École Polytechnique Fédérale de Lausanne (EPFL) in Switzerland.

### 1.3 Suprathermal ions

Suprathermal ions, also referred to as fast ions, are characterized by energies larger than the quasi-Maxwellian background plasma temperature. Many laboratory and astrophysical plasmas are characterized by the presence of suprathermal ions.

In magnetic fusion reactors, the alpha particles generated by the D-T fusion reactions (Eq. (1.1)) are suprathermal ions that will provide the dominant fraction of the heating and regulate the burning plasma regime [12]. Auxiliary heatings such as neutral beam injection (NBI) and ion cyclotron resonance heating (ICRH), which are widely used in present-day devices and will play a crucial role in future fusion devices, also generate a population of suprathermal ions that transfer their energy to the bulk plasma via Coulomb collisions.

ICRH typically heats a minority ion species that is injected in the plasma by injecting electromagnetic waves with a frequency of the order of the cyclotron frequency<sup>1</sup> of the minority ions. A resonant interaction transfers energy from the wave to the particles. The bulk plasma ions are then heated by collisions with the energetic minorities [13].

NBI consists of injecting highly energetic neutral atoms in the plasma. The neutral atoms are ionized by interacting with the plasma particles and become confined by the magnetic field. These confined energetic ions transfer their energy and momentum to the background plasma as they are slowing down due to the collisions. Consequently, they increase the plasma temperature and can also drive a current if the injection direction is carefully chosen.

In space, cosmic rays are an example of suprathermal charged particles, mostly protons,

<sup>1</sup>The cyclotron frequency  $\Omega_c = \frac{qB}{m}$ , where  $q$  is the particle charge,  $m$  its mass and  $B$  is the magnetic field intensity, is the frequency of the gyromotion of charged particles around the magnetic field lines.

with energies varying from  $\sim 1$  GeV to  $\sim 1 \times 10^{11}$  GeV and with Larmor radius ranging from  $\sim 1 \times 10^7$  km to a size larger than the size of the Galaxy [14]. Recently, measurements by the Fermi Large Area Telescope [15] and the Very Large Telescope [16] confirmed that the acceleration of cosmic rays to velocities close to the speed of light takes place in supernovae remnants, the expanding shells of material created in stellar explosions. An other sort of suprathermal ions in space are solar energetic particles, emitted by the Sun and accelerated to very high energies (up to  $\sim 1$  GeV) during solar flares or in interplanetary space by the shocks associated with coronal mass ejections. These energetic particles can be harmful to spacecraft functioning, disrupt radio transmissions on Earth and cause damage to electrical transmission line facilities. The details of the processes that lead to the acceleration of particles are not yet fully understood.

### 1.4 Transport of suprathermal ions

In fusion reactors, the transport of suprathermal ions, created by fusion reactions or auxiliary heating, plays a key role. Losses or internal redistributions of the suprathermal ions can quench fusion energy production and lead to dramatic damages to the reactor structure, hence they need to be kept under control.

In tokamaks, losses and redistribution of suprathermal ions can arise due to their interaction with macroscopic instabilities. For example, Alfvén waves, which can bend and compress the magnetic field, have a phase velocity that can be close to the velocity of suprathermal ions. As a consequence, suprathermal ions can resonate with the waves, destabilize them [17, 18], and in turn be expelled by them outside of the plasma. On the other hand, by carefully controlling auxiliary heatings, suprathermal ions can have a stabilizing effect on certain large scale instabilities [19]. The study of the interaction between energetic particles and large scale modes in tokamaks has been an ongoing field of research for several decades and is still the focus of intense theoretical, experimental and numerical efforts [20].

Fusion plasmas are also characterized by the presence of small-scale turbulence produced by electric and magnetic fluctuations with length scales of the order of the thermal ion Larmor radius and responsible for the major part of thermal particle and heat transport [21, 22]. Due to their high velocities, suprathermal ions perform their gyromotion around the magnetic field lines with much larger radii than the thermal ions. Because of their large orbits, it was initially expected that suprathermal ions would not interact with the small-scale turbulence due to the effects of orbit-averaging [23–25]. Recent tokamak results indicate that redistribution of suprathermal ions can be induced by turbulence, at least in some ranges of energy and of the ratio between suprathermal ion energy and background plasma temperature [26–29].

At present, most predictions of the turbulent transport of energetic and thermal particles are based on the assumptions of the diffusion paradigm [28–33], i.e. a local and Markovian transport. However, several experimental [34–41] and numerical [42–47] studies have shown that the transport of particles in turbulent magnetized plasmas is generally non-diffusive, and

that it cannot be described by a simple diffusion equation.

The leading explanation of the acceleration of cosmic rays and solar energetic particles is based on the diffusive shock acceleration theory, which was originally developed by Fermi [48]. In this theory, the particles are accelerated by the shocks waves present in supernovae remnants, during coronal mass ejections or at the solar wind termination [49]. Because of their random, diffusive motion, they cross the shock many times. At each shock crossing they gain energy and momentum. However, observations are not fully explained by the diffusive theory. For example, the fluxes of energetic ions and electrons accelerated at interplanetary shocks, measured by the spacecrafts Ulysses and Voyager 2 [50], show a power-law dependence in time that is in disagreement with the exponential decay predicted by diffusive theory. Also, the energy spectra of cosmic rays and solar energetic particles predicted by this theory do not always match observations [51]. Non-diffusive transport is thought to play a role in the energetic particle acceleration [42, 49–58].

### 1.5 Motivation and outline

The process of diffusion is the most elementary stochastic transport process. Brownian motion, the representative model of diffusion, played a important role in the advancement of scientific fields such as physics, chemistry, biology and finance. However, in recent decades, non-diffusive transport processes with non-Brownian statistics were observed experimentally in a multitude of scientific fields<sup>2</sup>. Examples include human travel [59, 60], in-cell dynamics [61], the motion of bright points on the solar surface [62], the transport of charge carriers in amorphous semiconductors [63], the propagation of contaminants in groundwater [64] and the search patterns of foraging animals [65]. Recently, a theoretical model provided a unified explanation for the prevalence of non-diffusive transport [66].

Understanding the physical mechanisms underlying the transport of suprathermal ions in turbulence is a major challenge for fusion reactors and astrophysical plasmas. Several observations indicate that transport in plasmas, under certain circumstances, may be explained by non-diffusive models. However, direct measurements of suprathermal ion transport in fusion and astrophysical plasmas are limited by the high temperatures of the former and the difficulty to access the later. In addition, detailed knowledge of the turbulence characteristics and of the background plasma is necessary to realistically model the transport of suprathermal ions. Thanks to easy diagnostic access and well characterized plasma scenarios, basic plasma devices, such as TORPEX, offer the ideal framework to investigate the transport of suprathermal ions.

At the beginning of this Thesis, a numerical investigation of the transport of suprathermal ions in TORPEX had shown that their transport was generally non-diffusive [47, 67] and the

---

<sup>2</sup>We note that non-diffusive transport in fields different than fusion plasma research is often referred to as *anomalous* diffusion, which has a different meaning in the fusion community (see Chapter 4). To avoid any confusion, we use the term *non-diffusive*.

## Chapter 1. Introduction

---

installation of a suprathermal ion source had started [68]. In this Thesis, we perform experimental measurements of a suprathermal ion beam in TORPEX and verify the agreement between the measurements and the propagation of the suprathermal ions in experimentally validated numerical simulations of the turbulent plasma. A non-diffusive model that explains the measurement is also developed. The experimental measurements, the numerical simulations and the theoretical model presented in this Thesis contribute to advancing the understanding of the fundamental mechanisms responsible for the transport of suprathermal ions in magnetized toroidal plasmas. The structure of the Thesis is as follows.

Chapter 2 introduces the toroidal device TORPEX and the specific setup developed for the injection and detection of suprathermal ions. The main features of the TORPEX plasmas investigated in this thesis are also presented.

Chapter 3 describes in details the data analysis methods applied to the suprathermal ion measurements. The estimate of the errors due to the measurements and data analysis is also presented. Finally, we present experimental measurements revealing the motion of the suprathermal ion beam.

In Chapter 4, the classical diffusion model and its assumptions are recalled, followed by a review of two of the main theoretical non-diffusive models, namely the continuous time random walk (CTRW) and the fractional Lévy motion (fLm).

Chapter 5 exposes the numerical simulations used to model the plasma dynamics in TORPEX and the propagation of suprathermal ions in the turbulent plasma. We present the results of an investigation of the suprathermal ion transport in TORPEX and some considerations about the simulations used for the comparison with the experiment.

Chapter 6 presents the application of the fractional Lévy motion (fLm) model to the numerical simulations of the suprathermal ions in TORPEX. We generalize one of the models presented in Chapter 4 to allow for an asymmetric propagator. We show that asymmetric fLm can be described by a transport equation using space-fractional differential operator with non-zero skewness. The time evolution of the radial particle position distribution is shown to be described by solutions of the fractional diffusion equation corresponding to asymmetric fLm.

Chapter 7 presents the comparison between experimental time-averaged measurements of the suprathermal ion beam dynamics and numerical simulations. In the first case, the suprathermal ions have an energy  $E \simeq 70$  eV and in the second they have an energy  $E \simeq 30$  eV. We compare the evolution of the radial width of the suprathermal ion beam with the results of numerical simulations to which a synthetic diagnostic is applied. The transport exponent is computed from the numerical simulations for the two cases. During the interaction phase, we find that the 30 eV ions experience a superdiffusive transport, while the 70 eV experience a subdiffusive transport.

In Chapter 8, the first time-resolved measurements of the cross-field transport of suprathermal

ions in a turbulent magnetized plasma are presented. We consider the same two cases than in Chapter 7, with suprathermal ion energies of 30 eV and 70 eV, for which the transport was identified to be superdiffusive and subdiffusive, respectively [40, 69]. We show that the time traces of the suprathermal ion current show a clear difference in the intermittency level. Using the technique of conditional average sampling (CAS) [70, 71], we identify the effect of turbulent structures on the suprathermal ion beam confirming the efficiency of gyroaveraging, depending on the ion energy, to decrease transport.

Finally, Chapter 9 summarizes the achievements of this Thesis and offers an outlook on possible future developments.



## 2 Experimental setup

In this Chapter, the toroidal device TORPEX is presented, together with the specific setup developed for the injection and detection of suprathermal ions, namely the suprathermal ion source on its toroidally movable system and the gridded energy analyzers. The main features of TORPEX plasmas investigated in this thesis are also presented.

### 2.1 TORPEX device

The TORoidal Plasma EXperiment (TORPEX) is a toroidal plasma device [72] with a major radius  $R_0 = 1$  m and a minor radius  $a = 0.2$  m (Fig. 2.1). It is being operated at the CRPP at EPFL since 2003 with the purpose of investigating turbulence and theory-experiment comparisons. The stainless steel vessel consists of 12 sectors, each having several ports accessible for the installation of multiple diagnostics. Four of the twelve sectors can be moved radially on rails to open the vessel and facilitate the installation of devices inside the torus. Although different magnetic configurations are possible using different sets of coils, such as the Ohmic coils for tokamak-like discharges [73] or the recently installed in-vessel toroidal conductor creating closed flux surfaces [74], all the experiments investigated in this Thesis are conducted in the so-called simple magnetized torus (SMT) configuration. In this configuration, the magnetic field is produced by 28 water-cooled toroidal coils (in red in Fig. 2.1) and 4 vertical coils (in orange in Fig. 2.1). The resulting magnetic field configuration has a main toroidal component and a weaker vertical component creating helical field lines. The return field line vertical distance is given by  $\Delta = 2\pi R \frac{B_v}{B_t}$ , where  $B_t$  and  $B_v$  are the values of the toroidal and vertical magnetic field at the center of the poloidal cross section. This configuration created a radial gradient and a curvature of the magnetic field that are key ingredients for the plasma instabilities developing in TORPEX and for the motion of suprathermal ions. These features along with open field lines are also characteristic of the magnetic field in the scrape-off layer (SOL) of tokamak plasmas.

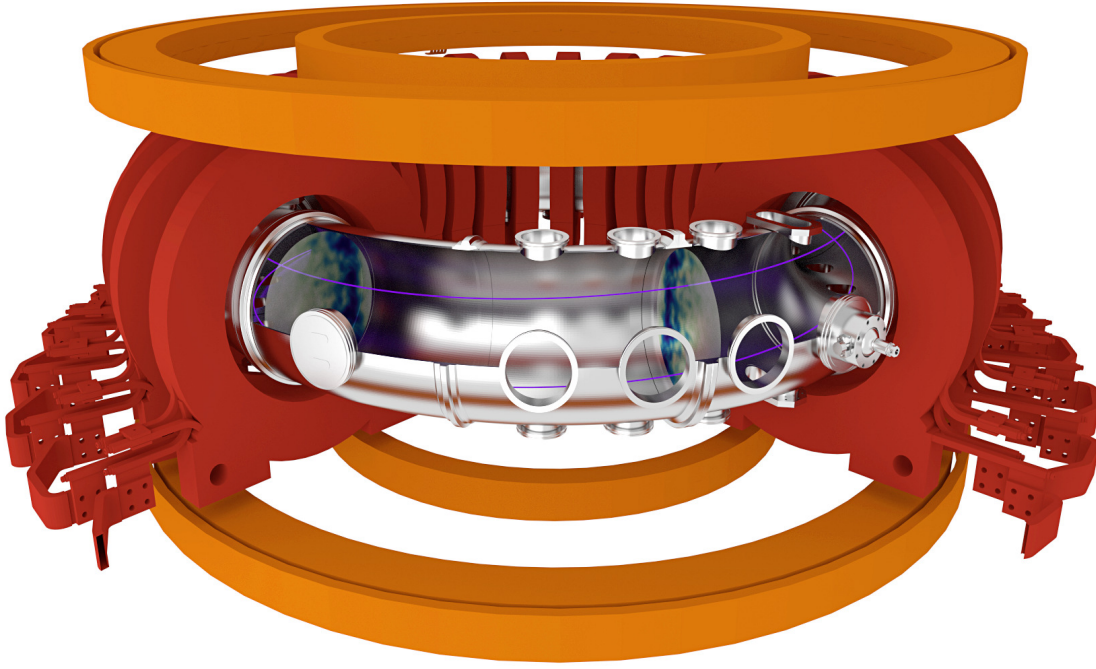


**Figure 2.1 | View of the TORPEX vessel with the copper coils producing the magnetic field.** The toroidal coils are in red and the vertical coils are in orange. In the SMT, magnetic field lines (violet) are open and helical, terminating on the bottom and the top of the vessel. Simulated snapshots of the plasma potential are also displayed at two toroidal positions.

### 2.1.1 Plasma production

TORPEX is equipped with two magnetrons, injecting microwaves in the O-mode polarization in the electron cyclotron (EC) range of frequencies ( $f_{\text{mw}} = 2.45 \text{ GHz}$ ), that are used to produce and sustain a stationary plasma. The first magnetron injects microwaves from the outboard of the device, called the low field side low field side (LFS), with a maximum power  $P_{\text{mw}} < 50 \text{ kW}$  and permits to modulate the injection power. The second magnetron injects microwaves from the bottom of the device with a smaller maximum power of  $P_{\text{mw}} = 1 \text{ kW}$  and allows to sustain plasmas during long period ( $\sim 15 \text{ min}$ ). The microwaves are absorbed at the EC resonance and the upper hybrid (UH) resonance layers, which act as particle and heat sources for the plasma [75]. The radial position of the EC layer (defined by  $f_{\text{mw}} = f_{\text{EC}}$ ) is controlled by the strength of the toroidal magnetic field, as the EC frequency is given by  $f_{\text{EC}} = eB/m$ , where  $e$  and  $m$  are the charge and mass of electrons. The position of the UH layer ( $f_{\text{mw}} = f_{\text{UH}} \simeq (f_{\text{EC}}^2 + f_{\text{p}}^2)^{1/2}$ ) also depends on the plasma density profile,  $n(R)$ , through the dependence of  $f_{\text{UH}}$  on the density in the plasma frequency  $f_{\text{p}} = (ne^2/m\epsilon_0)^{1/2}$ . For a detailed explanation of the plasma production in TORPEX, we refer the reader to Mario Podesta's PhD Thesis [76]. In the experiments addressed here, plasmas are sustained with the second magnetron over relatively long durations to allow statistically significant measurements of the suprathermal ion current. The plasma source is always located on the inboard of the device, called the high field side (HFS).



**Figure 2.2** | Photographs of some of the main diagnostics used on TORPEX

### 2.1.2 Main diagnostics

The low temperature of TORPEX plasmas, the presence of movable sectors and the large number of ports on the vacuum vessel offer easy access for diagnostics. Most measurements are performed with electrostatic probes, magnetic probes and a fast framing camera. Photographs of some of the main diagnostics are shown in Fig. 2.2. The *Bdot* probe is an array of magnetic pick-up coils that measures three components of the magnetic field at three locations, yielding the tangential component of the local current density [77]. The hexagonal turbulence imaging probe (HEXTIP) consists of 86 Langmuir probes (LPs) arranged in an hexagonal grid with a grid constant  $d = 35$  mm [73] that covers the entire plasma cross-section. The array of 8 LPs

that can be moved radially (SLP) and the five-tip triple probe (FRIPLE) are other examples of electrostatic LPs used in TORPEX. A fast framing Photron-APX-RS camera used with an image intensifier unit complements the electrostatic probe measurements. A tomographic reconstruction of the line-integrated camera images allows to study plasma structures smaller than the spatial resolution of electrostatic probes array in a non-perturbative manner with a high temporal resolution [78–80].

### Langmuir probe theory on TORPEX

In the next paragraphs, we present the basic theory of the electrostatic LPs used in TORPEX. Electrostatic probes are routinely used in TORPEX as they are one of the simplest and cheapest diagnostics in plasma physics, particularly suited for low temperature plasmas. However, the interpretation of their data can be delicate. When the electrostatic potential applied on the probe,  $V_{\text{pr}}$ , is held below the plasma potential,  $V_{\text{pl}}$ , the potential drop between the plasma and the probe is mostly confined in a region, called *sheath*, having a thickness of the order of a few Debye length  $\lambda_D = \sqrt{\epsilon_0 T_e / (n e^2)}$ . In the sheath, ions are attracted to the probe tip and electrons are partially repelled. Therefore, quasi-neutrality is broken and strong electric fields exist in the sheath. The simplest model considers a collisionless unmagnetized plasma with cold ions, Maxwellian electrons and a probe radius that satisfies  $r_p \gg \lambda_D$ . Such model allows one to express the current measured by the probe,  $I_{\text{pr}}$ , as a function of its electric potential [81]

$$I_{\text{pr}}(V_{\text{pr}}) = \frac{1}{2} e n c_s A_{\text{eff}} \left[ 1 - \exp\left(\frac{e(V_{\text{pr}} - V_{\text{fl}})}{T_e}\right) \right] = I_{\text{sat}} \left[ 1 - \exp\left(\frac{e(V_{\text{pr}} - V_{\text{fl}})}{T_e}\right) \right], \quad (2.1)$$

where  $n$  is the plasma bulk density,  $c_s = \sqrt{T_e / m_i}$  the sound speed for cold ions,  $A_{\text{eff}}$  the effective probe surface at the sheath boundary and  $V_{\text{fl}}$  the floating potential. If the probe voltage is strongly negative, only ions are collected. In this case  $e(V_{\text{pr}} - V_{\text{fl}}) / T_e \ll 1$  and Eq. (2.1) yields the *ion saturation current*  $I_{\text{pr}} = I_{\text{sat}} = \frac{1}{2} e n c_s A_{\text{eff}} \propto n \sqrt{T_e}$ . Time traces of  $I_{\text{sat}}$  provide straightforward access to a fluctuating plasma quantities and are therefore commonly used to study fluctuations properties such as power spectra or to perform statistical [82] or multifractal analysis [83]. They also provide an estimate of the plasma density by neglecting the square root dependence upon temperature. When the probe is floating,  $V_{\text{pr}} = V_{\text{fl}}$ , no current can flow and  $I_{\text{pr}} = 0$ . The floating potential is also commonly measured to characterize fluctuations in the plasma. It can be used to estimate the plasma potential since  $V_{\text{pl}} \simeq V_{\text{fl}} + \mu T_e / e$ , where  $\mu \simeq 3$  for hydrogen plasmas [75]. As the potential on the probe potential increases, electrons become gradually attracted and the current on the probe exponentially decreases as given by Eq. (2.1) and as can be seen in Fig. 2.3 between  $V_{\text{fl}}$  and  $V_{\text{pl}}$ . When the probe potential reaches the plasma potential the sheath disappears and Eq. (2.1) is no longer valid. If the probe voltage is biased over  $V_{\text{pl}}$ , the current measured by the probe is the electron saturation current. Measuring this transition provides a way to evaluate the value of  $V_{\text{pl}}$ , however, as seen in Fig. 2.3, the transition to the electron saturation does not occur sharply and this method is

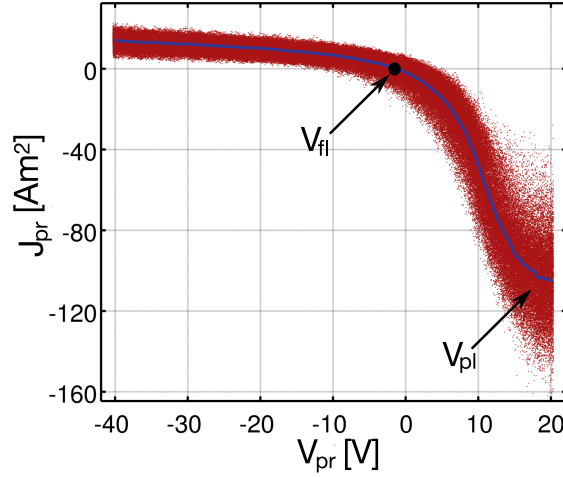


**Figure 2.3** | I-V characteristics from the SLP probe in TORPEX. The red dots represents the data from many voltage ramps and the blue line is the averaged characteristic. The floating potential is attained when  $J_{pr} = 0$  and the plasma potential is situated around 15 V. The imperfect ion saturation due to the ion sheath expansion is visible for  $V_{pr} \lesssim -10$  V.

accompanied with large uncertainties.

In order to compute the values of the density, temperature and plasma potential from Eq. (2.1), a complete I-V characteristics is measured. This is done by sweeping the voltage applied to the probe while measuring the current reaching the probe. The voltage range for the sweep is chosen to cover the ion saturation branch and the exponentially growing part of the I-V characteristics, typically from  $-40$  V to  $20$  V. As the plasma parameters vary rapidly, the sweep is done at a slow frequency (330 Hz) compared to the fluctuations frequency. The average of many sweeps provides a measure of the background profiles. Figure 2.3 shows an example of such measurements. A least-square fit of Eq. (2.1) to the averaged I-V curve gives the time-averaged values of  $n$ ,  $T_e$  and  $V_{pl}$ . A more refined theory taking into account the expansion of the sheath, which depends on the probe potential, is used on TORPEX [84]. The sheath expands when the probe potential is decreased, increasing the effective collection area of the probe and leading to an imperfect saturation of the ion current. This effect is modeled with a linear term with parameter  $\alpha$  [84]

$$I_{pr} = I_{sat}^0 \left[ 1 - \alpha(V_{pr} - V_{fl}) - \exp\left(\frac{e(V_{pr} - V_{fl})}{T_e}\right) \right], \quad (2.2)$$

where  $I_{sat}^0$  is the value of the ion saturation current extrapolated to the floating potential. The four parameters  $I_{sat}^0$ ,  $T_e$ ,  $V_{fl}$  and  $\alpha$  are fitted to the averaged I-V characteristics. Then, the density is evaluated from the value of  $I_{sat}^0$  and the plasma potential from  $V_{pl} = V_{fl} + \mu T_e / e$ . The parameters  $A_{eff}$  and  $\mu$  are determined experimentally for each probe. The effective size of the probe,  $A_{eff}$ , is taken such that the measured density at the UH resonance matches the value computed from theory. The value of  $\mu$  is evaluated by measuring I-V curves that cover both the ion and the electron saturation current branches [75], allowing to measure  $V_{pl}$ ,  $V_{fl}$  and

$T_e$ . The probes are then swept over a reduced voltage range, limiting the perturbations to the plasma. For example, for the probe SLP in hydrogen plasmas,  $\mu \simeq 3.1 \pm 0.6$  [75].

### Triple probe on TORPEX

In order to measure time traces of  $n$ ,  $V_{pl}$  and  $T_e$  on TORPEX, a five-tip triple probe called FRIPLE (Fig. 2.2) was developed [84, 85]. FRIPLE is based on the principle of the triple probe and has five tips that allow to reduce phase delay errors. The standard triple probe consists of three nearby probes that simultaneously measure three points of the I-V characteristics. One tip measures  $V_{fl}$ , while a constant potential difference  $\Delta V \gg T_e/e$  is applied between the two other tips, forming a double probe circuit. The current flowing between the two probes,  $I$ , and the potential at each tip,  $V_+$  and  $V_-$ , are measured. These quantities, together with the value of  $V_{fl}$ , permit to evaluate  $n_e$ ,  $T_e$  and  $V_{pl}$ , provided that the three tips all see the same plasma conditions. The tips are generally arranged perpendicularly to the background plasma gradients in order to come close to this situation. However, phase delay between the tips, for example if a wave propagates along the tip alignment direction, leads to errors in the measurements. To overcome this issue, a design with five tips is used in the FRIPLE probe. The fourth and fifth tips also measure  $V_+$  and  $V_{fl}$ , providing conjugate phase information to reduce phase delay errors [85]. The values of the electron temperature, density and plasma potential are then given by

$$T_e = \frac{e(V_+ - V_{fl})}{\ln 3}, \quad n = \frac{I}{ec_s A} \quad \text{and} \quad V_{pl} = V_{fl} + \mu T_e/e, \quad (2.3)$$

where  $A$  is the tip area. Ion-sheath expansion and stray capacitance due to the coaxial cables connecting the probe to the acquisition module are also taken into account when analyzing the data acquired on TORPEX. FRIPLE also features a novel guarding circuit reducing the stray capacitance [85]. We refer the reader to reference [85] for an explanation of these refinements.

### 2.1.3 Turbulence regimes

Extensive numerical investigations of the plasma instabilities in the SMT configuration have been performed using the three-dimensional (3D) fluid code global Braginskii solver (GBS) [86–89]. These have showed that three turbulence regimes can exist, each driven by an instability of different nature: the ideal interchange instability, the resistive-interchange instability and the drift-wave instability [89]. Numerical simulations validated against probe data in TORPEX [90, 91], show a transition from an ideal interchange regime to a resistive interchange regime, depending on the pitch of the magnetic field lines. The pitch depends upon the number  $N = L_v/\Delta$  of field lines toroidal turns from the bottom to the top of the vessel, where  $L_v$  is the vessel height. For low values of  $N$ , the pitch angle of the field line is large and the turbulent regime is characterized by the presence of ideal interchange modes with parallel wave number  $k_{||} = 0$  and vertical wave number  $k_v = 2\pi/\Delta$ . In this regime, the dominant

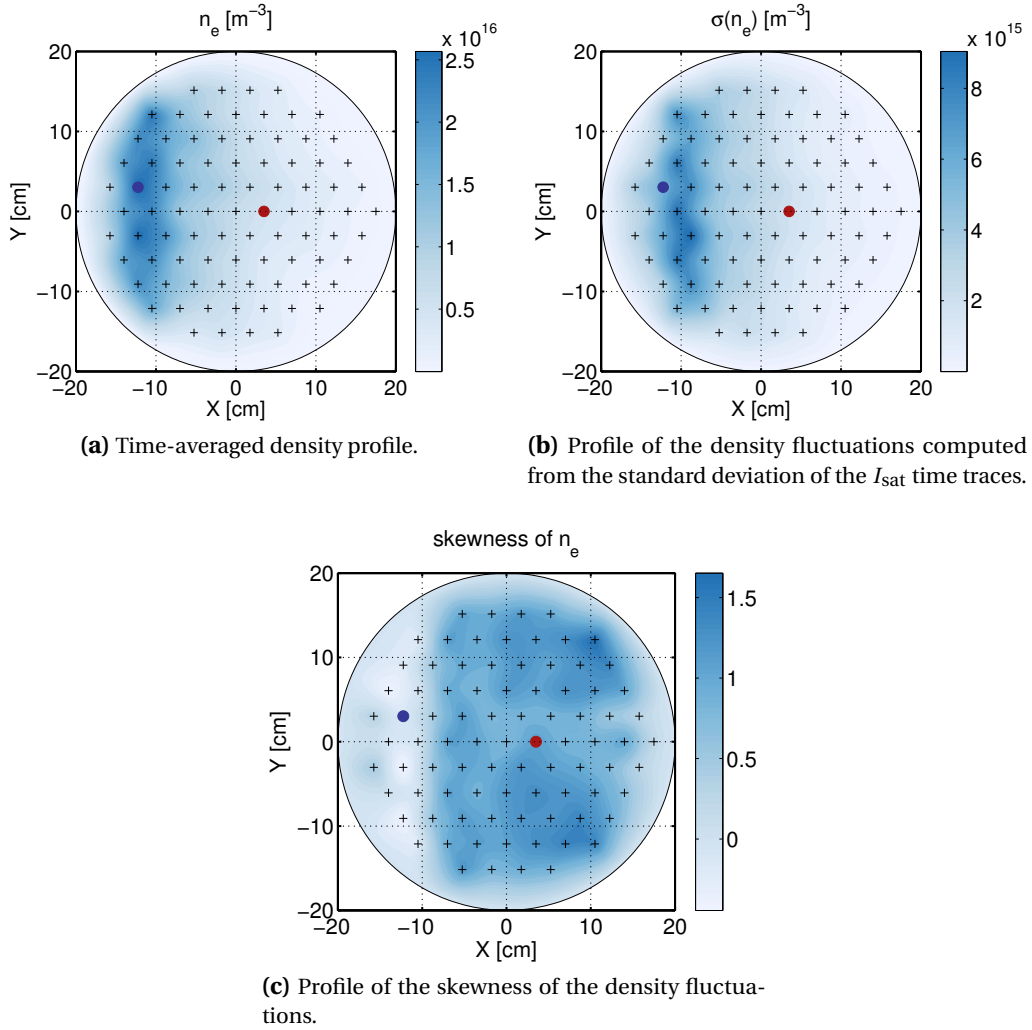
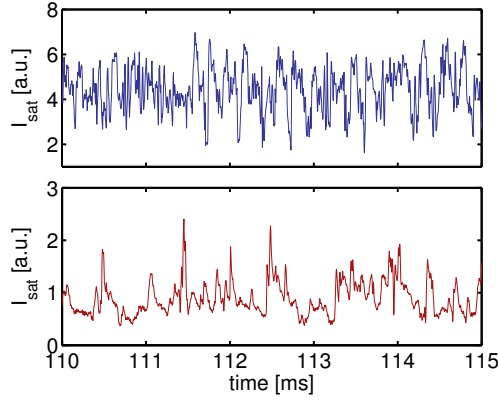


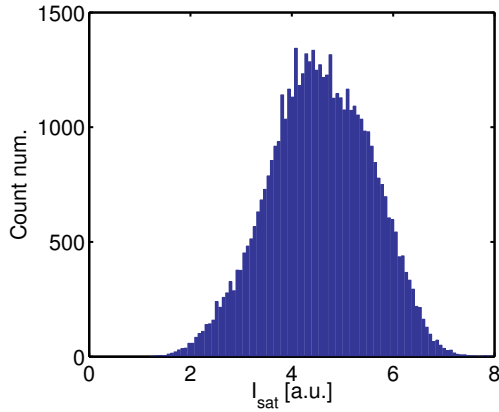
**Figure 2.4** | Poloidal profiles of the time-average, fluctuations and skewness of the electron density computed from the ion saturation current time traces, assuming  $T_e = 2.5$  eV. Two regions with different statistical signatures are visible, on the HFS, the *mode* region and on the LFS the *blob* region.

ideal interchange mode has a toroidal mode number  $n = 1$  and a vertical mode number  $l = L_v / \lambda_v = L_v / \Delta = N$ . Measurements reveal a transition, predicted by numerical simulations, for  $N \gtrsim 7$  to a state dominated by resistive interchange fluctuations with  $l \simeq 1$ ,  $k_v \simeq 2\pi / L_v$ ,  $n = 0$  and  $k_{\parallel} \simeq 1 / (RN)$  [89]. The drift-wave regime is obtained for sufficiently steep radial pressure gradient. However, the simulations suggest that, at the relatively high collisionalities of the TORPEX experiments, the transport driven by interchange modes prevents the gradient scale lengths from ever steepening into the drift-wave dominated regime [89].

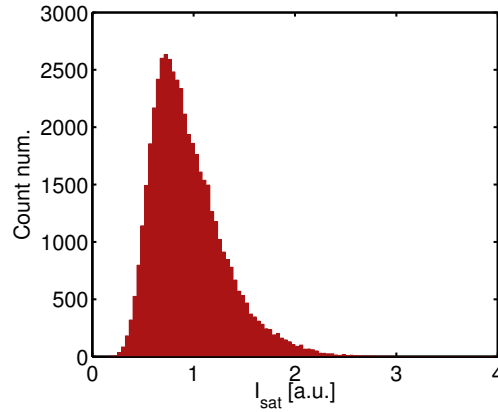
In this Thesis, all experiments have been conducted with hydrogen plasmas in conditions corresponding to the ideal-interchange regime. The main parameters characterizing these plasma discharges are indicated in Table 2.1. Figure 2.4 shows the time-averaged density



(a) Time traces of  $I_{\text{sat}}$  at the two positions indicated by the correspondingly colored dots on the profiles.



(b) Probability distribution functions of the  $I_{\text{sat}}$  time traces from the probe located in the mode region.



(c) Probability distribution functions of the  $I_{\text{sat}}$  time traces from the probe located in the blob region.

**Figure 2.5** | Time traces and PDF of the  $I_{\text{sat}}$  signal from two probes located in the mode (blue) and blob (red) region of the poloidal plane. The positions of the probes are indicated in Fig. 2.4.

profile in a poloidal cross section, computed from the array of 86 Langmuir probes (indicated by the black crosses) HEX TIP [92], measuring the ion saturation current,  $I_{\text{sat}}$ , and assuming a constant temperature  $T_e = 2.5 \text{ eV}$ . Two main regions are visible in Fig. 2.4. The plasma production takes place in the region defined by  $X \lesssim -5 \text{ cm}$ , as the EC resonance is located at  $X \approx -15 \text{ cm}$ . In this region, the plasma density forms a vertically elongated slab (Fig. 2.4a). The ideal-interchange mode is located at the position of the maximum of the pressure gradient ( $X \approx -10 \text{ cm}$ ), corresponding to the position where the density fluctuations are maximum, visible on Fig. 2.4b. On the other side of the device, the LFS, the plasma density is much lower as no plasma production occurs in this region. However, the profile of the skewness<sup>1</sup> of the fluctuations (Fig. 2.4c) reveals a clear difference compared to the mode region. Figure 2.5a shows the two time traces of the  $I_{\text{sat}}$  signals from two probe tips positioned in the two different

<sup>1</sup>The skewness of a random variable is the third standardized moments of a PDF. It is a measure of the asymmetry of a PDF, indicating the presence of a long tail on the right, or on the left, of the PDF if it is positive, or negative, respectively. The Gaussian distribution has a skewness equal to zero.

**Table 2.1** | Plasma parameters for the reference hydrogen plasma discharge.

Quantity	Symbol	Value
Major radius	$R_0$	1 m
Minor radius	$a$	0.2 m
Toroidal magnetic field	$B_t$	74 mT
Vertical magnetic field	$B_v$	2 mT
Field line return vertical distance	$\Delta$	18 cm
Number of toroidal field turns	$N$	2.2
Microwave power	$P_{\text{rf}}$	150 W
Neutral pressure	$p_n$	$5 \times 10^{-5}$ mbar
Electron density	$n_e$	$10^{16} \text{ m}^{-3}$
Electron temperature	$T_e$	2.5 eV
Ion temperature	$T_i$	< 1 eV
Neutral density	$n_n$	$1 \times 10^{18} \text{ m}^{-3}$
Ionization degree	$n_e/n_n$	0.7 %
Density gradient scale length	$L_n$	6 cm
Electron Debye length	$\lambda_D$	0.12 mm
Electron plasma frequency	$f_{\text{pe}}$	897 MHz
Ion plasma frequency	$f_{\text{pi}}$	21 MHz
Electron thermal velocity	$v_{\text{the}}$	$6.6 \times 10^5$ m/s
Ion thermal velocity	$v_{\text{thi}}$	< $9.8 \times 10^3$ m/s
Sound speed	$c_s$	$1.5 \times 10^4$ m/s
Electron Larmor radius	$\rho_e$	0.05 mm
Ion Larmor radius	$\rho_i$	< 1.4 mm
Ion Sound Larmor radius	$\rho_s$	2 mm
Electron cyclotron frequency	$f_{\text{ce}}$	13 GHz
Ion cyclotron frequency	$f_{\text{ci}}$	7 MHz

regions. While the time trace from the probe in the mode region reveals coherent, periodic, fluctuations, the probe on the LFS displays a bursty time trace with intermittent spikes. These are responsible for the large skewness of the fluctuations in this region. As can be seen in Fig. 2.5c, the PDF of the time trace of the LFS probe is positively skewed, while the PDF of the other probe (Fig. 2.5b) is almost Gaussian. The bursts in the time traces in this region are caused by intermittent convective particle transport. Bunches of particles are ejected from the main plasma and travel radially outward [84]. This phenomenon is commonly observed at the edge of magnetically confined plasmas, such as in the low-latitude ionosphere [93] or at the edge of tokamaks [94]. These plasma structures are generally called *blobs* or *filaments* because of their shape which is elongated and aligned with the magnetic field lines.

In TORPEX, an in-depth investigation of blob creation and propagation [71, 77, 95–101] has revealed that blobs are generated from an interchange wave that increases in amplitude and extends radially in response to a decrease of the radial pressure scale length. The radially elongated plasma density structures are then sheared off by the  $\mathbf{E} \times \mathbf{B}$  flows and propagate

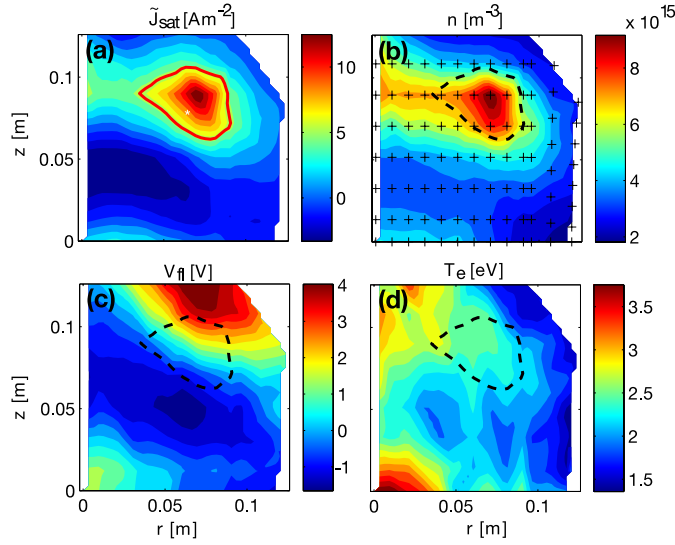


**Figure 2.6** | Example of the 2D profile of  $J_{\text{sat}}$ ,  $n$ ,  $V_{\text{fl}}$ , and  $T_e$  for a  $\text{H}_2$  blob obtained with the conditional sampling method (taken from [95]).

radially outwards. Blob motion is caused by the electric field created by the charge separation arising inside blobs because of the  $\nabla B$  and curvature drifts. The  $\mathbf{E} \times \mathbf{B}$  convection resulting from this vertical electrical field gives rise to the radial motion of the blob. An experimentally verified analytical formula predicts the blob velocity by taking into account parallel currents, ion polarization current, inertia and ion-neutral collisions that can damp charge separation [100]. Due to charge separation and sheath boundary conditions, parallel current and plasma potential dipoles are associated with the blob density monopole. Figure 2.6 shows the density monopole, floating potential ( $V_{\text{fl}} \approx V_{\text{pl}} - 3T_e/e$ ) dipole and temperature associated with a blob, measured using conditional sampling [70]. A comprehensive study of blobs in TORPEX can be found in Christian Theiler’s PhD Thesis [84].

## 2.2 Production and detection of suprathermal ions

In this section, we describe the experimental setup (Fig. 2.7) designed and built at the CRPP to study the transport of suprathermal ions in TORPEX. It was specifically designed to identify the transport regime in a turbulent interchange-mode plasma by measuring the spreading of a suprathermal ion beam. This setup allows measurements of the time-averaged three-dimensional (3D) profile of the suprathermal ion beam as it interacts with the plasma turbulence [40]. The first versions of the suprathermal ion source and detector were developed in collaboration with the group from the University of California at Irvine (UCI) working on the Large Plasma Device (LAPD) at UCLA [68, 102] in the context of G. Plyushchev PhD Thesis [68]. This setup demonstrated the feasibility of the suprathermal ion measurements in TORPEX, however, it also revealed their difficulty due to the extremely low signal-to-noise ratio. During my Thesis, several improvements were brought to the design of the source and detector, and to

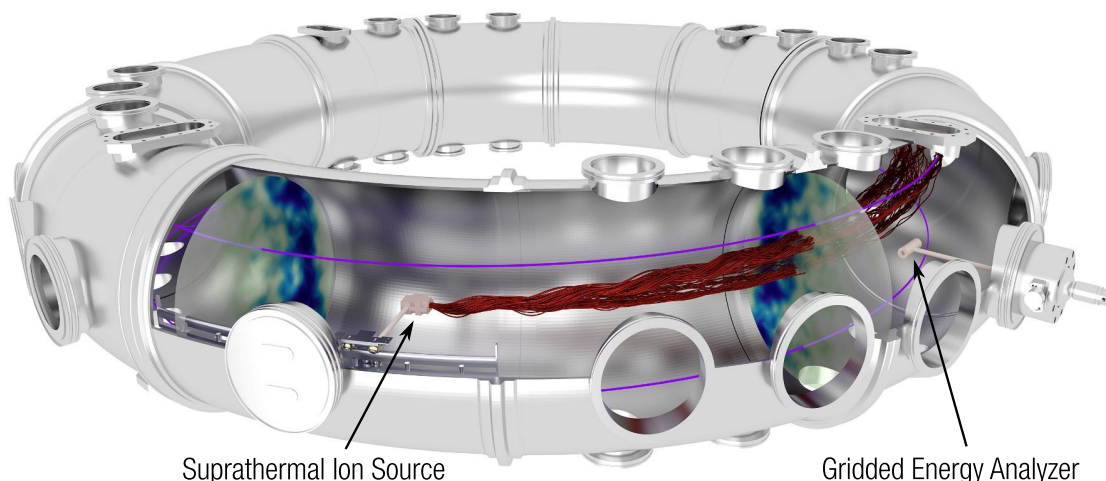


**Figure 2.7 | View of the TORPEX vessel with magnetic field line and suprathermal ion detection system.** TORPEX contains open, helical magnetic field lines (violet) with a radial gradient in field strength that terminate on the vessel. Also shown are the suprathermal ion source on a toroidal sliding track and one detector mounted on a 2D moveable system that can also be displaced toroidally. This combination allows measurement of a 3D suprathermal ion current profile. Computed examples of simulated suprathermal ion trajectories with an initial energy of 30 eV are shown in red, emitting from the source. Gyromotion and the irregular spreading of the ion beam due to interaction with the plasma turbulence is apparent. Simulated snapshots of the plasma potential are also displayed at two toroidal positions.

the measurement technique. An issue with the suprathermal ion source is the relatively short life of its emitter and its sensitivity to exposition to atmospheric pressure. In order to overcome this issue, the design of the suprathermal ion source was improved to facilitate and accelerate its assembly. Furthermore, a movable system was developed, allowing to move the source inside the vessel along the toroidal direction. An analog lock-in was developed in order to use synchronous detection in real-time. This device has the possibility to remove capacitive effects with the addition of a *dead-time* in the demodulation of the signal. A second detector was also built to perform measurements at different toroidal locations, without opening TORPEX and therefore breaking the vacuum.

### 2.2.1 Suprathermal ion source

The source is based on a two-grid accelerating system with a thermionic emitter similar to the one used in the LAPD at UCLA [39, 103]. The emitter is made of an aluminosilicate layer doped with lithium 6 ions deposited onto a cylindrical molybdenum body purchased from HeatWave Labs Inc [104]. Figure 2.10 shows a schematics of the source. A current  $I \approx 2.5\text{A}$  and a voltage  $U \approx 8.5\text{V}$  ( $P \approx 21\text{W}$ ) are used to heat the emitter by Joule effect up to a temperature of the order of  $1000\text{ }^\circ\text{C}$  [103] to start the thermionic emission. At this heating power, the suprathermal ion current is  $\sim 10\mu\text{A}$ . For its first usage, each emitter is slowly heated, typically over a period of 6 hours, to avoid the deterioration of its surface and the deposition of impurities. The following heating procedures can be faster, lasting typically 3 to 4 hours. Figure 2.8 shows the

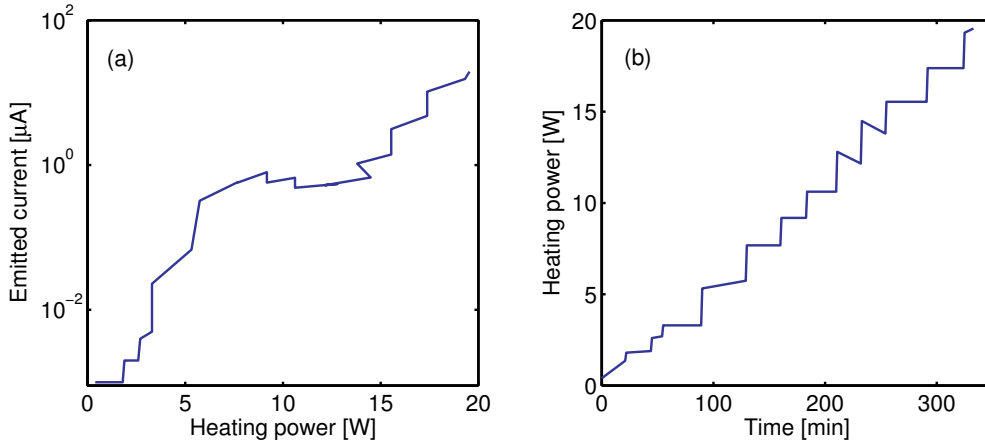


**Figure 2.8** | (a) Emitted current as a function of the heating power of the source emitter. (b) Evolution of the heating power as a function of time.

emitted current as a function of heating power measured during a test made in a vacuum chamber where the emitter is held at 1.5 mm from a metallic plate and a voltage difference of 300V is imposed between the emitter and the plate.

The emitters are heated inside TORPEX and are kept in its vacuum ( $p \lesssim 1 \times 10^{-6}$  mbar) until they are depleted. The extracted current is increased by applying an accelerating electric field between the emitter and the inner grid (Schottky effect) reducing the potential energy barrier at the surface of the emitter [105]. Figure 2.9 shows the voltage biasing scheme of the source. In order to sustain the high temperature of the emitter, the metallic parts of the source are made of molybdenum and the grids of tungsten (Fig. 2.10). The outer grid is grounded so that ions are decelerated between the inner and the outer grids. The exit ion energy is given by the voltage difference between the emitter and the outer grid. The voltage on the inner grid is biased typically at  $-20$  V, not too negatively to avoid the acceleration of electrons thermo-emitted from the heated tungsten or secondary electrons emitted by the grid. The mesh of the grids has 150 wires per inch with a wire diameter of 0.02 mm resulting in a nominal aperture size of 0.15 mm which is of the order of the Debye length. The optical transparency of the grids is 75 %. Thus, the grids prevent the plasma from entering into the source and let a significant fraction of the suprathermal ions pass through them.

The original design of the suprathermal ion source [68, 102] has been improved to have a better electrical insulation of the different components by carving paths for the different electric wires directly in the boron nitride casing (Fig. 2.11). In addition, to facilitate the assembly of the source, the original design of the boron nitride casing, consisting of a cylinder with a screwcap, has been modified to a design with two boron nitride pieces encasing the emitter and the grids, held by ceramic screws (Fig. 2.10). Speeding up the mounting of the source is important since the  ${}^6\text{Li}$  ions emitter has a relatively short life expectancy ( $\sim 40$  hours).

In order to perform 3D measurements of the suprathermal ion beam, the source is mounted

## 2.2. Production and detection of suprathermal ions

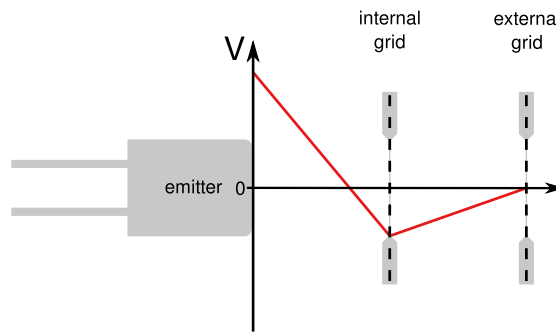
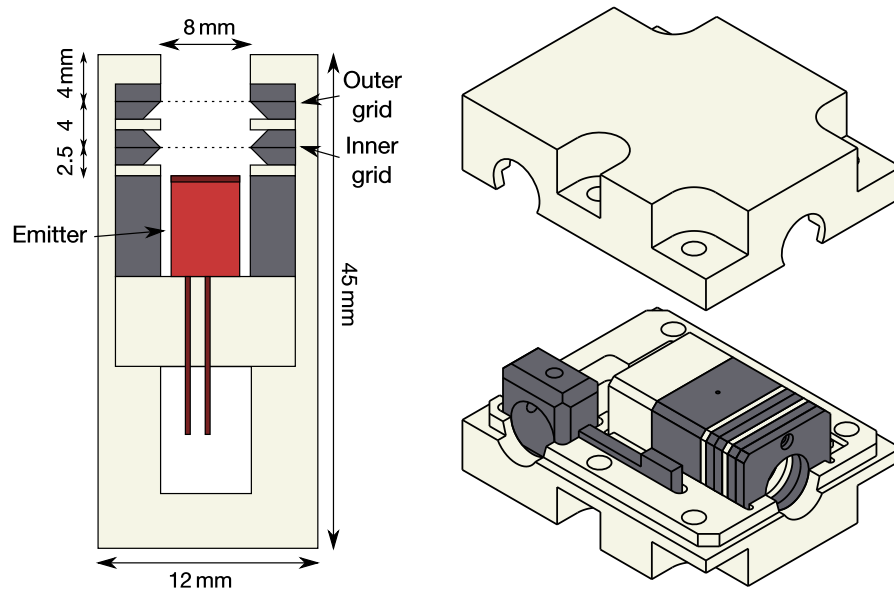


**Figure 2.9** | Voltage biasing scheme of the suprathermal ion source used to accelerate the ions and prevent the plasma from entering into the source.



**(a)** Side view of the suprathermal ion source showing the emitter, the molybdenum pieces holding the grids and the emitter, and the boron nitride pieces.

**(b)** Open view of the suprathermal ion source showing the two nitride boron pieces encasing the emitter and the grids.

**Figure 2.10** | Schematic of the suprathermal ion source. Nitride boron pieces are in white, molybdenum pieces in gray and the emitter is in red.

on a rail that allows it to be moved in the toroidal direction (Fig. 2.12). The rail is installed in one of the movable sector of TORPEX and permits to move the source continuously along the toroidal direction over a distance of  $\sim 48$  cm. The source is moved between discharges and a high-resolution poloidal cross-section of the suprathermal ion current profile is measured by the detector for each toroidal position of the source. The complete system is contained inside the vacuum chamber of TORPEX. The possibility of moving the source without having to open TORPEX, and breaking the vacuum, is essential for the experimental campaign. Indeed, the lifetime of the emitter is greatly diminished when it is exposed to atmospheric pressure. An ultrasonic piezoelectric motor was chosen to move the source along the rail. Ultrasonic

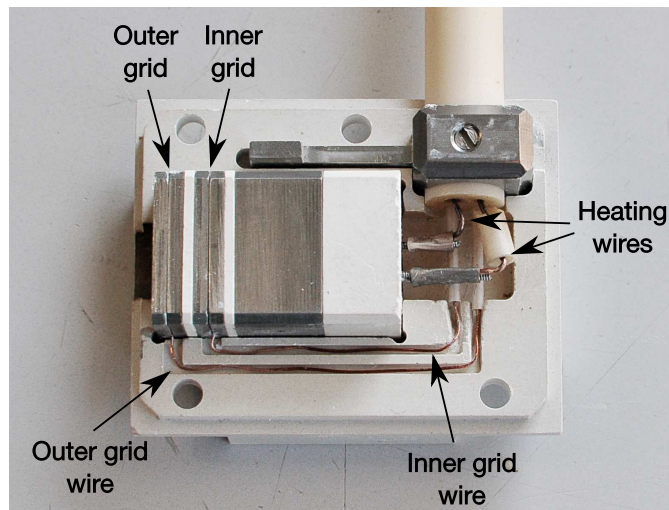


**Figure 2.11** | Photograph of the inside of the suprathermal ion source showing the paths for the electric wires carved in the boron nitride casing.

motors are particularly well suited to work in vacuum and magnetized environments since they do not need any greasing and do not embed permanent magnets. The source motion was measured with a system tracking infrared LEDs attached to the cart moving on the rail [106]. The 3D translation and the 3D rotation were recorded during several motions along the rail and a resulting maximum deviation of the source from its expected vertical position of 4.5 mm was recorded.

### 2.2.2 Suprathermal ion detection

#### Gridded energy analyzers

Gridded energy analyzers (GEAs), also called retarding-field or retarding-potential energy analyzers, are widely used in plasma physics to measure electron or ion energy distribution functions or fluxes. For examples, they are used in industrial plasma processing [107] to measure ion fluxes impinging onto substrates or in space plasmas, installed on satellites for *in-situ* measurements [108]. GEAs allow to discriminate the measured particles depending on their energy. Electrostatic potentials on metallic grids and on the collector create electrostatic “retarding” fields that let only ions, or only electrons, with an energy above a certain value reach the collector [81]. The simplest GEAs have just one grid in front of the collector, while more advanced models can have four or five grids that limit the collection of secondary electrons that can disturb the measurements [109].

In TORPEX, the suprathermal ion detector consists of two identical miniaturized GEAs, each having two grids, allowing the measurement of the suprathermal ion current [39, 68, 102]. The two GEAs face opposite directions so that differential detection is used to remove a significant part of the background noise. During this thesis, a second detector was build, based on

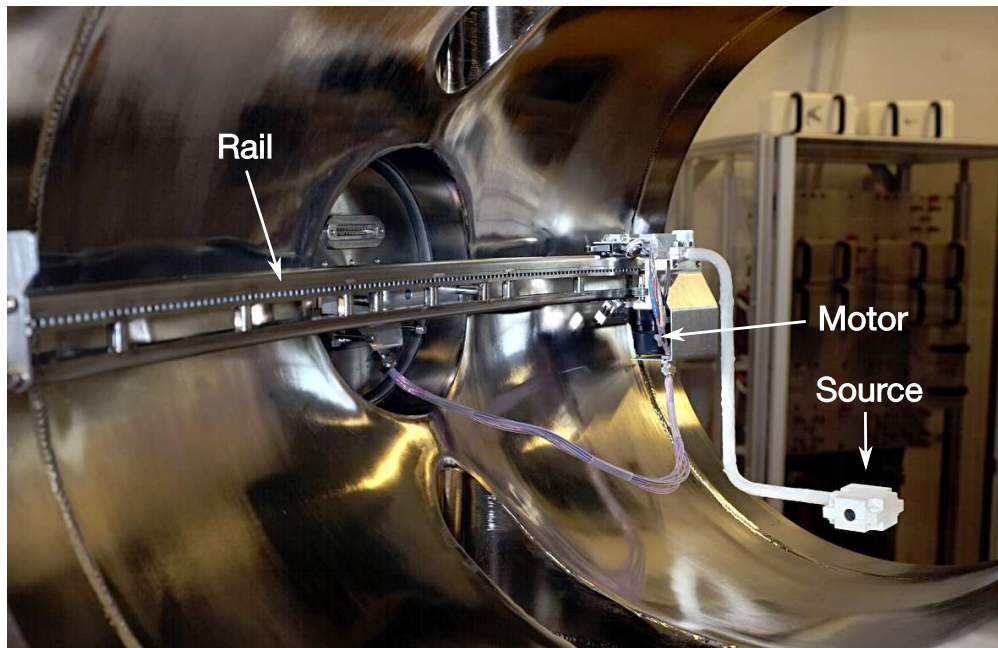
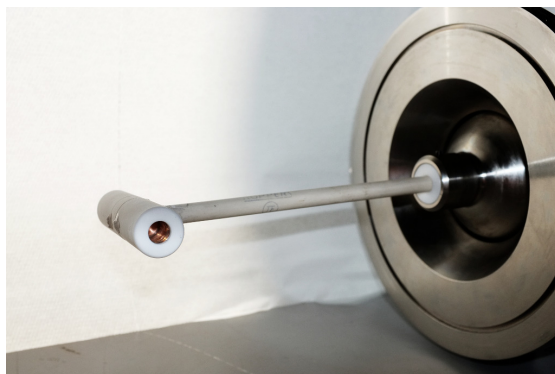
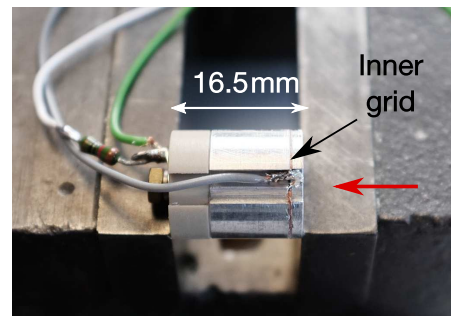


**Figure 2.12** | Photograph of the suprathreshold ion source mounted on the toroidally-movable system in one of the TORPEX sectors. The source is positioned in the lower part of the device to maximize the distance traveled by the ions before they reach the upper wall because of their vertical drift.



**(a)** Photograph of one of the detectors mounted on the poloidal movable system.



**(b)** Photograph of a part of one of the GEAs inside a detector. The red arrow indicates the direction of entry of the detected particles.

**Figure 2.13** | Photographs of the inside and outside of one of the detectors consisting of two GEAs facing opposite direction.

the same design that the one used previously on TORPEX [68]. Using two detectors allows doubling the number of measurements without having to open TORPEX. The two detectors are positioned at different toroidal positions along the suprathreshold ion beam.

Figures 2.13 and 2.14 show photographs and a schematics of the new detector. Metallic parts holding the grids are in aluminum, insulating pieces are in plastic, the casing is made of Macor glass-ceramic and, the grids and collectors are made of copper. The mesh of the grids has

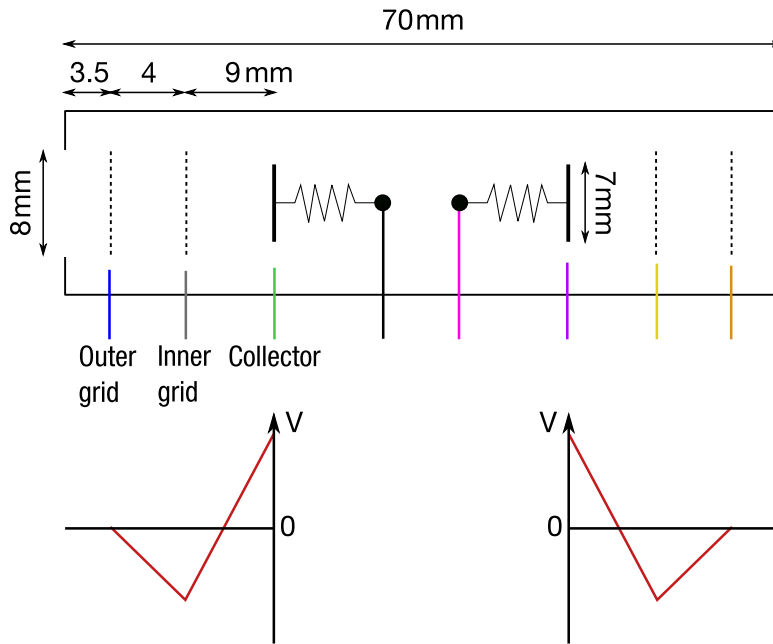


**Figure 2.14** | Drawing of the detector indicating the distances between each element and the size of the inlet and of the collector. The color scheme represents the actual colors of the connection cables. The voltage biasing scheme is represented on the bottom.

200 wires per inch and 0.02 mm wire diameter. The bias voltage on the collector is chosen to repel thermal ions from the bulk plasma. As plasma ions in TORPEX are cold ( $T_i \ll 10$  eV), a value of 10 V is sufficient to ensure that only ions emitted by the source are detected. Resistors with a resistance of 10 k $\Omega$  are connected to the collectors and embedded inside the detector (Fig. 2.14) to convert the collected current in a voltage difference. The inner grid is biased to a negative voltage to repel plasma electrons. The outer grid is grounded to zero potential and serves as a first barrier preventing the plasma to enter the detector. Measurements of the ion energy distribution can be done by varying the voltage on the collector. However, GEAs with only two grids cannot repel secondary electrons liberated by the inner grids as suprathermal ions collides on them. This effect obscures the ion signal and does not allow to reliably measure the energy distribution of the collected particles. For this purpose, GEAs have typically three or more grids. Nevertheless, this is not in issue for the measurement of suprathermal ion current profile, since the collector voltage is not varied in this case. For GEAs with three or more grids, the selection of the ions is done by positively biasing one of the inner grid and an other placed between this grid and the collector is negatively biased in order to repel the secondary electrons [81, 109]. Here, we use the detector to selectively measure the current due to suprathermal ions and not to measure their energy distribution. As we do not vary the potential on the collector, the collection of secondary electrons only affects the absolute value of our measurements.

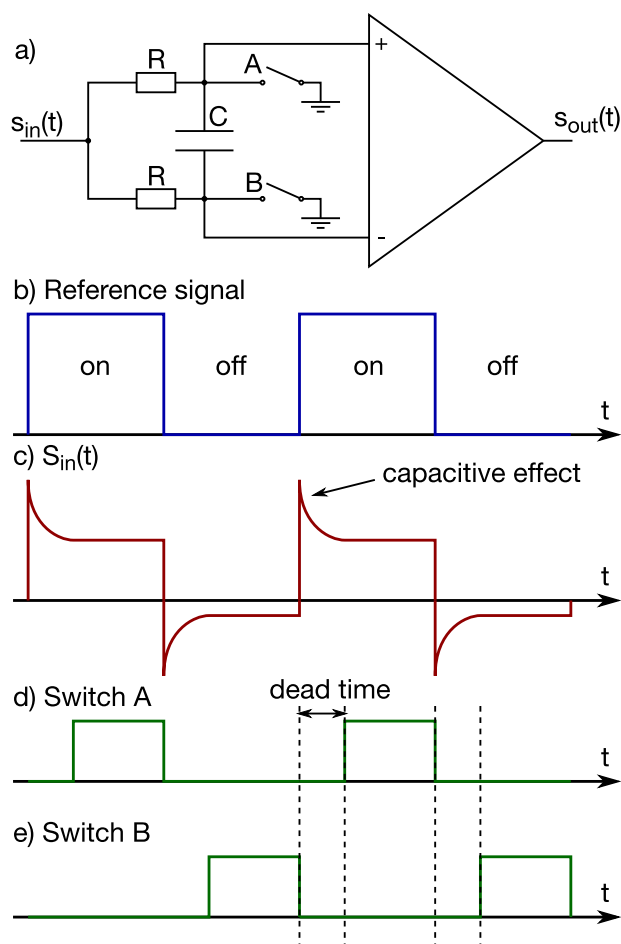


**Figure 2.15** | a) Electronic diagram showing the principle of a lock-in amplifier with a dead-time. The system consists of two switches operated in a staggered pattern, a RC low-pass filter and a differential amplifier. b) Time trace of the reference signal used to modulate the source bias voltage. c) The resulting signal in the detector with capacitive effects due to the voltage modulation of the source. d) and e) Switching pattern for the two switches. On these time traces, a signal value equal to zero represents an open switch.

### Synchronous detection of the suprathreshold ion current signal

As the suprathreshold ion current is extremely weak ( $\sim 10 \mu A$ ) and its signal is small compared to the background noise, a synchronous detection scheme is used to improve the signal-to-noise ratio [110]. In our case, the emitter bias is square-modulated by a reference signal (Fig. 2.15b) at a frequency,  $f_{ref} = 1073 \text{ Hz}$ , chosen to avoid harmonics of the electric grid (50 Hz). The suprathreshold ion current is therefore “switched” on and off at this frequency, while the background noise remains independent of this modulation.

The detection is made using a phase-sensitive detector (PSD), also called a “lock-in” amplifier, consisting of a switch operated at the reference frequency, a RC low-pass filter ( $R = 220 \text{ k}\Omega$ ,  $C = 1 \mu\text{F}$ ,  $\tau = RC \approx 0.2 \text{ s}$ ) and a differential amplifier (Fig. 2.15a). The switch inverts the signal

periodically resulting in a signal consisting of the suprathreshold ion current component and the background noise, during the “on” phase, and only the *inverted* noise during the “off” phase. The low-pass filter averages the resulting signal over many periods of the reference signal, effectively averaging-out the noisy part of the signal and giving a DC signal proportional to the suprathreshold ion current. Unfortunately, in our setup, the modulation of the emitter results in undesired space-dependent capacitive effects in the detector (Fig. 2.15c). In order to remove this capacitive noise, a new lock-in amplifier allowing to set a dead-time has been developed. The dead-time is introduced with the help of a second switch (Fig. 2.15a). The two switches are opened and closed according to the pattern shown in Fig. 2.15d and Fig. 2.15e. During the dead-time, the two switches are open and the common-mode rejection of the differential amplifier removes the capacitive effects from the output signal. The duration of the dead-time is adjusted to optimize the removal of these capacitive effects. The final signal is then integrated to obtain a DC output proportional to the suprathreshold ion current.

### Gain of the detection chain

The detection chain comprises different elements that each amplify the collected current with a certain gain. The first element is an analog circuit connected on the output of the detector with a theoretical gain  $G_1 = 56 \times 10^3$ . Then, there is a differential amplifier used to subtract the signal of the detector measuring the background noise to the one measuring the suprathreshold ion current that has a variable gain  $G_2 = \{10, 20, 50, 100, 200, 500\}$ . And finally, the lock-in amplifier has a gain,  $G_3$ , that depends on the value of the dead-time and which is measured to be  $1.4 < G_3 < 12$ . The value of the entire amplification chain is measured to take into account the imperfections due to the cables and electronics and a correction factor  $C = 0.88$  is found between the theoretical gain and the real gain. The factor is almost independent upon the test signal frequency between 10 Hz and 10 kHz. The total gain is given by  $G = G_1 G_2 G_3 C$  and varies between  $G_{\min} \approx 784 \times 10^3$  and  $G_{\max} \approx 336 \times 10^6$ , depending on the value of  $G_2$ .

## 3 Experimental technique

This Chapter describes in details the data analysis to reconstruct the time-averaged 3D suprathermal ion current profile. The quantity used to measure the spreading of the suprathermal ion beam due to its interaction with the plasma turbulence, namely the standard deviation of the suprathermal ion profiles, is discussed. The estimate of the errors due to the measurements and data analysis is also presented. Finally, we present experimental measurements revealing the motion of the suprathermal ion beam. Measurements of the radial spreading of the beam are presented in Chapter 7.

### 3.1 Poloidal cross section of the suprathermal ion current

Poloidal cross sections of the suprathermal ion current are reconstructed from the time-averaged current measurements. The detector is mounted on a motorized two-dimensional (2D) movable system [102]. In the configuration used for these experiments, a typical discharge lasts several minutes, during which the plasma is continuously sustained by microwave power. The detector is moved in the poloidal plane allowing measurements at several positions. Figure 3.1 shows an example of the time trace of the 2D position and of the signal measured by the detector during a plasma discharge. Several scans allow to recover the entire suprathermal ion current profile. The resolution of the measurements is adapted to the shape of the profile. For example, the gray circles shown on Fig. 3.2 represent the measurement positions used to reconstruct the poloidal suprathermal ion current profile in the chosen example. The detector is moved in steps and remains at each position for at least 10 seconds to provide a statistically-relevant time average. The time average is obtained using the analog lock-in amplifier presented in section 2.2.2. The poloidal current profile is then reconstructed by interpolating the scattered data points onto a 2D uniform grid with 1 mm spacing using the natural-neighbors method [111]. The offset arising from the analog lock-in amplifier is finally removed by computing its value as the average of all the interpolated data points that have a value smaller than the 5% of the maximum ion current value anywhere on the profile.

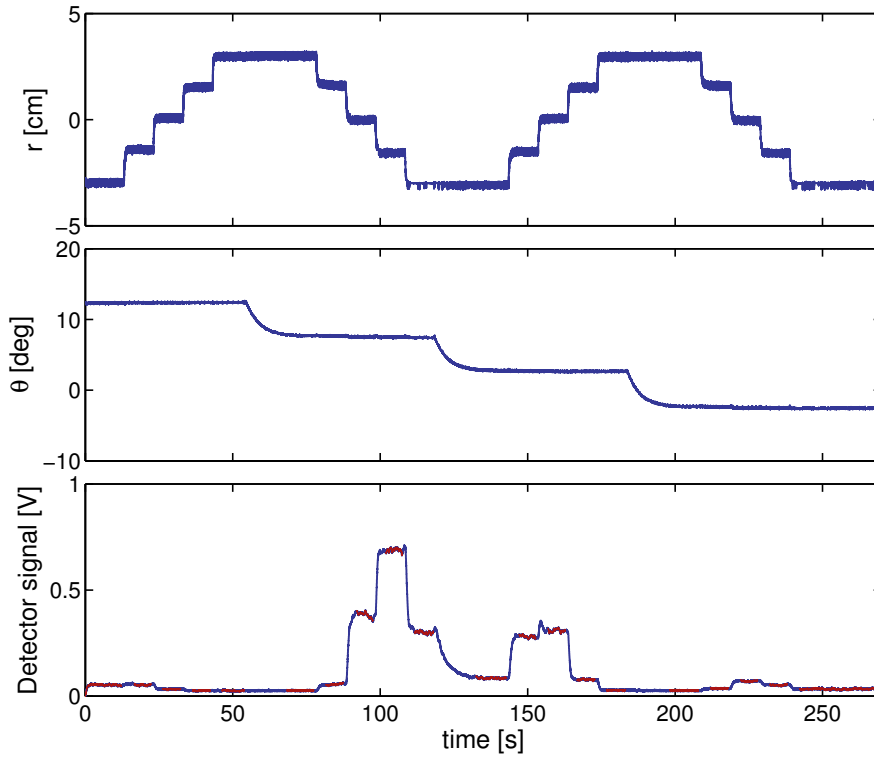


**Figure 3.1** | Example of a time trace from a poloidal scan with the suprathermal ion detector for 70 eV ions at a toroidal distance of 2.2 m from the source. The radial position,  $r$ , and the angle,  $\theta$ , defining the position of the detector in polar coordinates shown in Fig. 3.2 are also recorded. The period during which the detector is at rest are indicated in red on the detector time trace. The displacement of the detector is reported on the poloidal plane in Fig. 3.2.

### 3.2 Mean position and standard deviation of the suprathermal ion current poloidal profiles

To quantify the displacement and the broadening of the suprathermal ion beam, the mean position and the standard deviation of the suprathermal ion current profile are computed. Different methods can be employed to evaluate these quantities. The position of the maximum value of the profile and the full width half maximum can be used. Alternatively, fitting a 2D Gaussian on the profile can also provide a value for the mean position and width of the profile. However, these methods assume that the profile is smooth and regular. The assumption that the profile is Gaussian, and therefore that it can be described by only two parameters, is very strong. Here, we decided to use the general definition of the mean and of the standard deviation of a distribution, making no assumptions on the shape of the profiles. It must be noted that, ultimately, we want to compare the experimental profiles with profiles computed from numerical simulations with a synthetic diagnostic (Chapter 5). Different methods could be used to compute the position and width of the profiles, but the important point is to use the same method for both, experimental and simulated profiles. In the following, we detail the method used to compute these quantities. We are mostly interested by the radial width of the

### 3.2. Mean position and standard deviation of the suprathermal ion current profiles

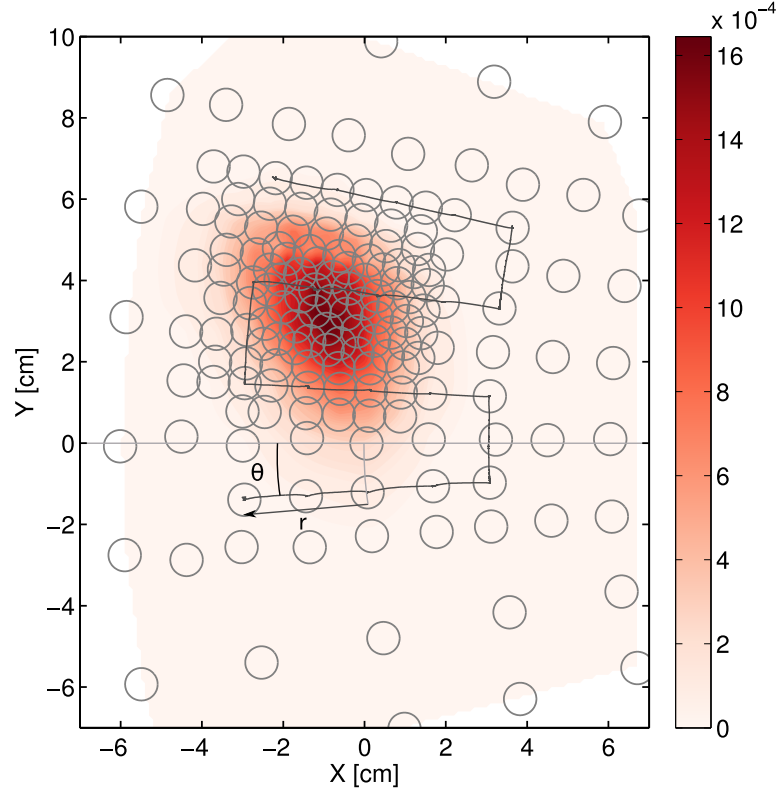


**Figure 3.2** | Reconstructed poloidal suprathermal ion time-averaged current density [ $A/m^2$ ] profile for 70 eV ions at a toroidal distance of 2.2 m from the source. The gray circles represents the positions of the detector used to reconstructed the poloidal profile. The size of the circle represents the aperture size of the detector. The black line shows the displacement of the detector corresponding to the measurement shown in Fig. 3.1, measured by  $r$  and  $\theta$ .

profile as we are investigating the radial transport of suprathermal ions. The vertical position of the beam is also computed, since it allows to verify the displacement of the beam, which is mostly vertical due to the curvature and  $\nabla B$  drifts. The radial position and the vertical width of the profiles can naturally be computed using the same method.

The mean vertical position of the suprathermal ion current distribution is computed from the interpolated profiles (Fig. 3.2) by taking vertical slices of the profile every millimeter. In order to select the relevant portion of the profile, only slices that have a maximum value greater than 30% of the global maximum value of the current are taken into account. Selecting more slices by choosing a smaller ratio than 30% do not significantly change the result. Then, the mean vertical position is computed for each selected slice  $j$  as

$$\bar{y}_j = \frac{\sum_i y_i \cdot I_i}{\sum_i I_i}, \quad (3.1)$$

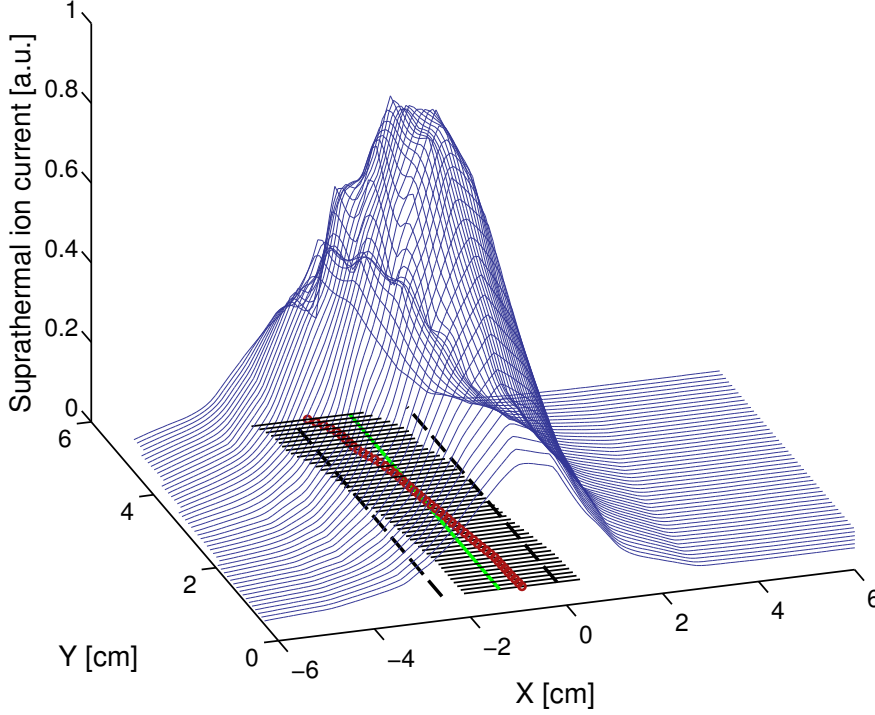


**Figure 3.3** | Example of the evaluation of the mean radial position and radial width of a suprathermal ion current profile. The blue lines represents the selected horizontal slices of the profile in Fig. 3.2. The red points indicates the radial position of the mean of each  $j$  slice,  $\bar{x}_j$ . The black lines under each  $j$  slice have a length  $2\sigma_j$ , representing their width. The green line show the position of the mean radial position of the entire profile,  $\mu_x \approx -1$  cm, and the dashed black lines are separated from the green line by a distance  $\sigma \approx 1.2$  cm, showing the mean width of the entire profile.

where the  $y_i$  are the vertical positions along the  $y$  axis and the  $I_i$  are the corresponding ion current values. Finally the mean vertical position of the beam profile,  $\mu_y$ , is computed as the average of all the  $\bar{y}_j$ :  $\mu_y = \langle \bar{y}_j \rangle_j$ . Figure 3.3 shows the computation of the mean radial position and of the radial width of a typical profile.

To quantify the radial transport, the standard deviation of the ion current distribution profiles, is computed using a similar technique. Relevant *horizontal* slices are selected using the same criteria as for the vertical slices (Fig. 3.3) and the radial standard deviation of each slice is computed as

$$\sigma_{R,j} = \left[ \frac{\sum_i (x_i - \bar{x}_j)^2 \cdot I_i}{\sum_i I_i} \right]^{1/2}. \quad (3.2)$$

Here,  $x_i$  represents the radial positions and  $\bar{x}_j$  the mean radial position of the slice  $j$ . The radial standard deviation of the entire profile is given as the average of the standard deviation of all the slices:  $\sigma_R = \langle \sigma_{R,j} \rangle_j$ .

### 3.3 Evaluation of the measurement errors

The errors arising from the measurements of the position and width of the 2D profiles depend on the size of the detector, the height and the shape of the profile, the resolution of the measurements and the accuracy of the detector positioning system.

To take into account the size of the detector, the resolution of the measurements and the accuracy of the positioning system, a simulation of the measurements and of the data analysis is done on prescribed profiles. The results are then compared with the actual values. Gaussian profiles with different standard deviations,  $\sigma$ , are created on a high resolution 2D grid with 0.5 mm spacing. An example is shown in Fig. 3.4a. A synthetic detector is displaced over the profile on a coarser grid (4 mm spacing), representing the typical resolution of our measurements. At each step, an error on the position of the detector is created by a random variable with a Gaussian distribution with zero mean and a standard deviation  $\sigma_{\text{pos}} = 2$  mm, representing the uncertainty in the position of the movable system. The value at each point of the coarser grid is computed as the average of all the points of the 2D Gaussian contained in a circle of the size of the detector (radius of 4 mm), centered on the point position (Fig. 3.4b). This profile is then interpolated by using the same method used to reconstruct the suprathreshold ion current profiles from the experiments (Section 3.1). The resulting profile is shown in Fig. 3.4c. Finally, the standard deviation of the interpolated profile,  $\sigma_{\text{mes}}$ , is computed by using the technique detailed in Section 3.2. In order to average the effect of the random error on the position, this procedure is repeated 50 times for each profile width and the average of the standard deviation off all profiles is taken. The convergence of the average was verified.

The relative error,  $\epsilon_r = |\sigma_{\text{mes}} - \sigma|/\sigma_{\text{mes}}$ , is shown in Fig. 3.5 as a function of the measured standard deviation of the profiles. The error is smaller than 10% for profiles having a standard deviation larger than 0.65 cm and increases rapidly when the width of the profiles decreases. For measured standard deviations of 0.25 cm, the error is 95%. This shows the limitation of our measurement set-up due to the size of the detector aperture. However, this is only an estimate. In reality, the resolution of the measurements can be increased and the error associated with the positioning system has a systematic part due to the motion of the detector and depends on the direction of the motion, which changes during the scan (Fig. 3.1). Modeling it with a Gaussian random variable does not capture this complexity but it gives an estimate of its importance.

Another source of errors comes from the fact that the suprathreshold ion current profiles are not perfectly Gaussian. In this case, using only the mean position and the standard deviation of the profile is not enough to completely describe them. Higher moments, such as the skewness and the kurtosis, could be used. In order to take into account this effect without using higher moments we compute the error associated with this effect. For a 2D Gaussian profile, the method described in Section 3.2 to measure the standard deviation of the profile provides the same value for the standard deviation  $\sigma_{R,j}$  of all slices. Therefore, the standard deviation of all the  $\sigma_{R,j}$  provides a measure of the deviation of the profile shape from a perfect Gaussian.

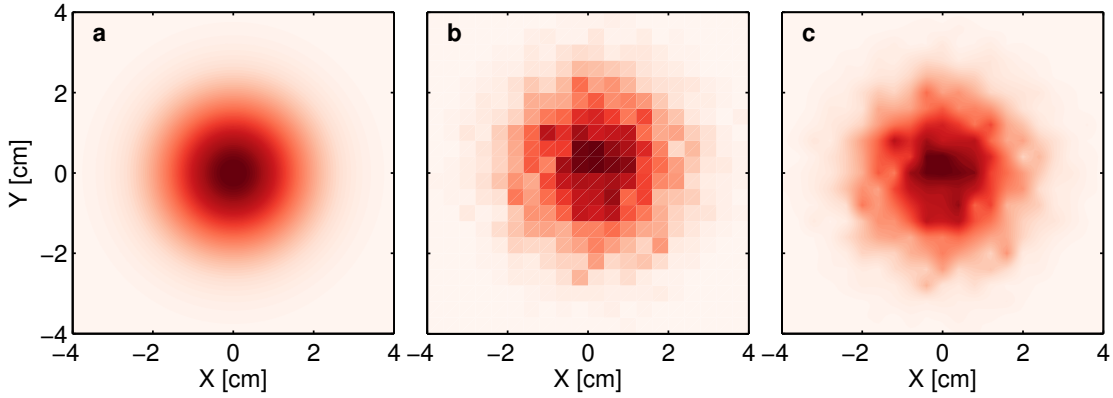


**Figure 3.4** | Profiles showing the technique used to evaluate the error due to the measurement with a finite size detector. **a:** 2D Gaussian with a standard deviation  $\sigma = 0.95$  cm computed on a high resolution grid. **b:** Profile resulting from the displacement of a synthetic detector over the 2D Gaussian with a step size of 4 mm. **c:** Profile reconstructed from the synthetic detector measurements with a standard deviation  $\sigma = 0.98$  cm.

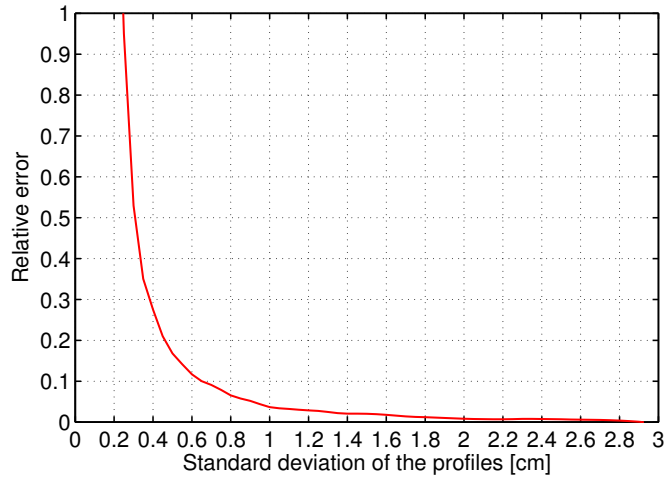


**Figure 3.5** | Relative error associated to the finite size of the detector and the uncertainty of its position as a function of the standard deviation of the ion current density profiles.

We note here that an arbitrary 2D elliptic Gaussian that can be tilted with respect to the  $x$  and  $y$  axes, has the same standard deviation, along the  $x$  axis, for all value of  $y$  regardless of its tilt. Indeed, a general expression for a 2D Gaussian, centered at the origin, is given by

$$f(x, y) = Ae^{-(ax^2+2bx+cy^2)}, \tag{3.3}$$

where  $\begin{pmatrix} a & b \\ b & c \end{pmatrix}$  is a positive-definite matrix. The variance along the  $x$  axis is given by

$$\sigma_x^2(y) = \frac{\int (x - \mu_x(y))^2 f(x, y) dx}{\int f(x, y) dx} = \frac{1}{2a} \quad (3.4)$$

where the mean along  $x$  is given by

$$\mu_x(y) = \frac{\int x f(x, y) dx}{\int f(x, y) dx} = -\frac{by}{2a}. \quad (3.5)$$

The variance along the  $x$  axis does not depend on  $y$ . The standard deviation of all the  $\sigma_{R,j}$ , which is equal to zero for a 2D Gaussian profile, provide therefore a measure of the irregularity of the profiles.

To conclude this section, the error on the vertical mean position is given by the standard deviation of all the  $\bar{y}_i$ , and takes into account the size of the detector as well as the irregularity of the rail:

$$e_{\mu_y} = \left[ \frac{1}{N-1} \sum_{j=1}^N (\bar{y}_j - \mu_y)^2 \right]^{1/2} + \frac{d}{2} + r, \quad (3.6)$$

where  $N$  is the number of slices,  $d = 8$  mm is the diameter of the detector aperture and  $r = 4.5$  mm represents the deviation due to the irregularity of the rail.

The error on the width of the profiles is given by the standard deviation of all the  $\sigma_{R,j}$  added to the error,  $\epsilon_r$ , computed with the method detailed above:

$$e_{\sigma_R} = \left[ \frac{1}{N-1} \sum_{j=1}^N (\sigma_{R,j} - \sigma_R)^2 \right]^{1/2} + \epsilon_r \sigma_R. \quad (3.7)$$

### 3.4 Motion of the suprathreshold ions

In this section, we evaluate the motion of the suprathreshold ions in the absence of the perturbations due to their interaction with the turbulence. We compute the vertical position of the suprathreshold ion beam as a function of the toroidal distance it travels and of its energy.

In the absence of a plasma, the motion of suprathreshold ions in TORPEX is a combination of the cyclotron motion around the magnetic field lines and the vertical drift of the guiding center due to the curvature and gradient of the magnetic field. The cyclotron frequency for Lithium 6 ions is given by

$$f_{si} = \frac{\Omega_{\text{fi}}}{2\pi} = \frac{1}{2\pi} \frac{qB}{m} \simeq 188 \text{ KHz}, \quad (3.8)$$

### Chapter 3. Experimental technique

---

where  $m$  and  $q$  are the mass and the electric charge of the particle,  $B$  is the magnitude of the magnetic field, and the Larmor radius of the suprathermal ion orbits is

$$\rho_L = \frac{mv_{\perp}}{qB}, \quad (3.9)$$

where  $v_{\perp}$  is the component of the particle velocity perpendicular to the magnetic field. The guiding centers drift due to the gradient and the curvature of the magnetic field are expressed as [1]

$$\mathbf{v}_{\nabla B} = \frac{1}{2} \frac{mv_{\perp}^2}{qB} \frac{\mathbf{B} \times \nabla B}{B^2}, \quad (3.10)$$

$$\mathbf{v}_R = \frac{mv_{\parallel}^2}{qB} \frac{\mathbf{R}_c \times \mathbf{B}}{R_c^2}, \quad (3.11)$$

where  $v_{\parallel}$  is the component of the velocity parallel to the magnetic field and  $\mathbf{R}_c$  is the curvature radius. The grad- $B$  drift direction depends on the charge of the particles. For ions in TORPEX, it is directed upwards.

Considering cylindrical coordinates  $(r, \phi, z)$ , in TORPEX the magnetic field can be written as  $\mathbf{B} = B_0 \frac{R_0}{R} \mathbf{e}_{\phi} + B_z \mathbf{e}_z$ , where  $B_0$  is the value of the toroidal magnetic field at the injection position  $R_0$ . The pitch angle of the magnetic field,  $\theta = \arctan \frac{B_z}{B_0} \simeq 0.027$  rad, being very small, we consider that the drift velocities perpendicular to the magnetic field can be taken along the vertical axis. In the following we consider first order approximations in  $\theta$ . We also neglect the contribution of the vertical component of the magnetic field to the value of its norm ( $|\mathbf{B}| \simeq B_0$ ).

In this geometry, the vertical drift due to grad- $B$  and curvature is

$$\mathbf{v}_{\text{up}} = \mathbf{v}_{\nabla B} + \mathbf{v}_R = \frac{m}{qB_0R_0} \left( v_{\parallel}^2 + \frac{1}{2} v_{\perp}^2 \right) \mathbf{e}_z. \quad (3.12)$$

Defining the velocity pitch angle as  $\lambda = v_{\perp} / v_{\parallel}$  and recalling the definition of the suprathermal ion energy  $E = \frac{1}{2} m (v_{\perp}^2 + v_{\parallel}^2)$ , the upward drift can be written as

$$\mathbf{v}_{\text{up}} = \frac{E}{qB_0R_0} \left( \frac{2}{\lambda^2 + 1} + \frac{1}{1 + \frac{1}{\lambda^2}} \right) \mathbf{e}_z = \frac{E}{qB_0R_0} \frac{2 + \lambda^2}{1 + \lambda^2} \mathbf{e}_z. \quad (3.13)$$

A supplementary vertical velocity of the guiding center,  $\mathbf{v}_p$ , appears in cylindrical coordinates because of the vertical pitch angle of the magnetic field lines  $\theta$ ,

$$\mathbf{v}_{\text{pitch}} = v_{\parallel} \theta \mathbf{e}_z = \left( \frac{2E}{m(\lambda^2 + 1)} \right)^{\frac{1}{2}} \theta \mathbf{e}_z. \quad (3.14)$$

### 3.4. Motion of the suprathermal ions

**Table 3.1** | Parameters of the suprathermal ions.

Quantity	Symbol	Value
Lithium 6 mass	$m$	$1.0036 \times 10^{-26}$ kg
Lithium 6 ion charge	$q$	$1.6022 \times 10^{-19}$ C
Injection position	$R_0$	1 m
Toroidal magnetic field at the injection position	$B_0$	0.074 T
Magnetic field pitch angle	$\theta$	0.027 rad
Velocity pitch angle	$\lambda$	0.1 rad
Mean radial electric field	$\bar{E}_r$	40 V/m
Energy of the suprathermal ions	$E$	70 eV
Cyclotron frequency	$f_{si}$	188 KHz
Cyclotron period	$\tau_{si}$	5 $\mu$ s
Larmor radius	$\rho_L$	8 mm
Velocities		
Initial	$v_0$	47.3 km/s
Parallel	$v_{\parallel}$	47.0 km/s
Perpendicular	$v_{\perp}$	4.7 km/s
Curvature drift	$v_R$	1.9 km/s
Grad- $B$ drift	$v_{\nabla B}$	9 m/s
Mean $\mathbf{E} \times \mathbf{B}$ drift	$v_{E \times B}$	540 m/s
Vertical magnetic pitch	$v_{pitch}$	1.3 km/s

In the presence of a plasma, a mean radial electric field,  $\bar{\mathbf{E}} = \bar{E}_r \mathbf{e}_r$ , is present in TORPEX due to the gradient of the plasma potential [75]. This field gives rise to an additional vertical drift velocity

$$\mathbf{v}_{E \times B} = \frac{\mathbf{E} \times \mathbf{B}}{B^2} = \frac{\bar{E}_r}{B_0} \mathbf{e}_z. \quad (3.15)$$

The unperturbed vertical velocity of the suprathermal ion guiding center can be written as  $v_z = v_{up} + v_{pitch} + v_{E \times B}$  and the vertical position as a function of the toroidal distance,  $R_0 \phi$ , is given by

$$z = z_0 + v_z t = z_0 + v_z \frac{R_0 \phi}{v_{\parallel}} = z_0 + v_z R_0 \phi \left( \frac{2E}{m(\lambda^2 + 1)} \right)^{-\frac{1}{2}}. \quad (3.16)$$

Typical values of each drift velocity term are reported in Table 3.1 along with the suprathermal ion parameters. We see that, except for the grad- $B$  drift, all the upward drifts are important.

Figure 3.6 shows measurements of the vertical position of the beam along with the position computed from Eq. (3.16) and computed from numerical simulations detailed in Chapter 5. A very good agreement is shown. An oscillation of the vertical position, caused by the cyclotron

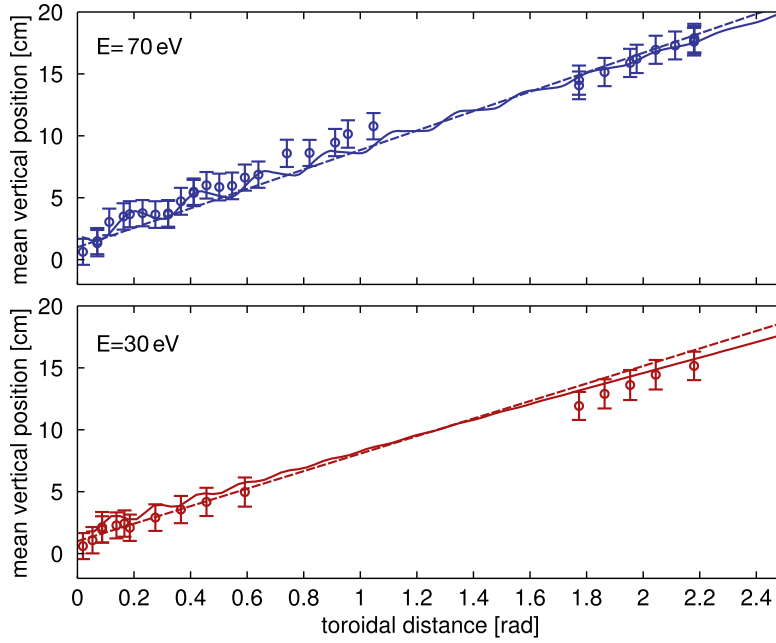


**Figure 3.6** | Vertical position of the suprathermal ion beam as a function of the toroidal distance for two ion energies. The dots represent experimental data, the dashed lines are computed with Eq. (3.16) and the continuous lines are obtained with a synthetic diagnostic from numerical simulations detailed in Chapter 5. The vertical drift experienced by the suprathermal ions is visible.

motion of the ions, is visible in the experimental measurements as well as in the simulation results. Indeed, the toroidal distance traveled by 70 eV ions during one gyromotion,  $v_{\parallel} \tau_{si} \approx 23$  cm, corresponds to the observed oscillation period.

### 3.5 Measurements with and without plasmas

Here, we present an example of measurements of the suprathermal ion beam width made with and without plasma, in the presence of a magnetic fields [39]. The radial and vertical standard deviations of the current profiles are shown as a function of the toroidal angle  $\phi$  in Fig. 3.7. Together with the experimental measurements, the standard deviation of the beam profiles obtained with the synthetic diagnostic from numerical simulations is shown (Chapter 5 details the numerical simulations and the synthetic diagnostic).

Figure 3.7 reveals an oscillation of the beam width at the cyclotron frequency. A small spreading in the initial parameters creates a small spreading of the ion Larmor radii and a small initial phase difference in the gyromotion among the ions. This induces an oscillation of the beam width at the cyclotron frequency [37, 39]. In the presence of plasma (Fig. 3.7 right), one can notice, on top of the oscillations, a broadening of the beam width due to its interaction with the plasma. This turbulent broadening will be investigated and characterized in Chapter 7. The agreement between simulations and experiments is remarkable, although a small mismatch in the phase of the oscillations between experiment and simulation is observed for the case

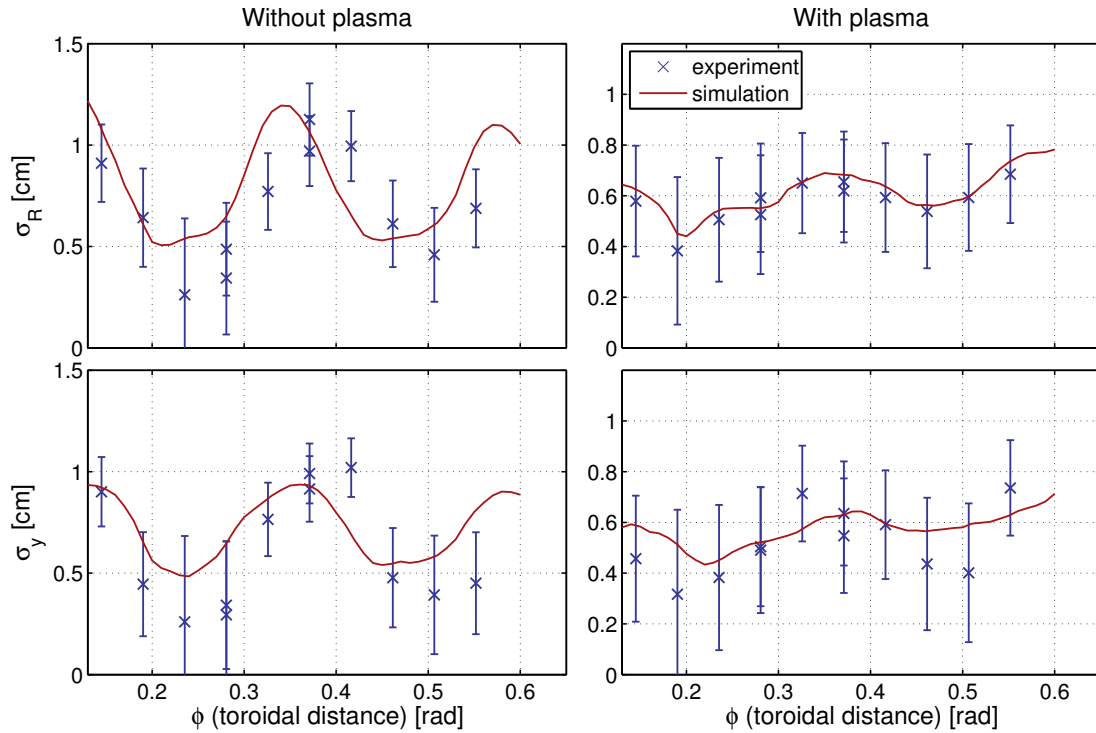


**Figure 3.7** | Radial (top row) and vertical (bottom row) standard deviation of the suprathermal ion current density profiles as a function of toroidal distance for ions with an energy of 70 eV, in the absence (left) and with a plasma (right). The blue crosses represent the experimental data and the red lines represent the value obtained from profiles computed from numerical simulations with a synthetic diagnostic (Chapter 5). The oscillations due to the gyromotion is visible. In the case where a plasma is present, a spreading on top of the oscillation is revealed.

without plasma. The absolute value of the standard deviation is also decreased in the presence of plasma. Those differences between the operation of the source with and without plasma could be explained by the fact that the functioning of the source is affected by the surrounding plasma. In the absence of a plasma, an accumulation of ions on the surface of the source outlet can deviate the ions exiting the source, increasing their perpendicular velocity and, therefore, their Larmor radii. When the source is surrounded by a plasma, the ions accumulated on the source surface are neutralized and the beam is more focused.



## 4 Non-diffusive transport

Transport of particles, heat and momentum in plasmas is generally described in the framework of the diffusion-advection paradigm [112–114]. Diffusion is the transport of a quantity in a medium down a concentration gradient due to random collisions with the particles of the medium. Advection is the transport of a quantity by a fluid due to the fluid’s bulk motion. At a microscopic level, the diffusion-advection paradigm assumes the existence of an underlying uncorrelated, Gaussian stochastic process, i.e. a Brownian random walk with a drift. This implies a number of restrictive assumptions such as the locality of transport and the lack of long-range correlations. For example, in Fick’s law, the fluxes are assumed to depend only on local quantities, i.e., the gradients of the fields. In the language of plasma physics and fusion, the term *classical transport* refers to the motion of charged particles that is due to Coulomb collisions. Across the magnetic field, such motion has step sizes that correspond to the charged particles’ Larmor radius. In toroidal magnetically confined plasmas, such as tokamaks and stellarators, the model of *neoclassical transport* extends the diffusion-advection paradigm of classical transport to complex magnetic geometries [115] to include complex orbit effects. Orbits in tokamaks are in fact characterized by particle trapping in local magnetic mirrors, due to the field non-uniformity in the toroidal direction, and guiding center drifts across the magnetic field lines. Both classical and neo-classical models assume that the plasma is in a quiescent state. When applied to tokamaks, these underestimate the observed transport by an order of magnitude or more [21]. This discrepancy is due to the transport caused by turbulent fluctuations in the plasma. Indeed, magnetized plasmas are often characterized by the presence of turbulence, which may transport or trap particles much more effectively than Coulomb collisions and therefore invalidate the classical or neo-classical models. The excess of measured loss rates compared to neoclassical predictions is what is called *anomalous transport* [21]. Anomalous diffusion coefficients are usually estimated by the means of quasilinear theory [22, 116], which investigates the diffusion in phase space due to the interaction between wave and particles, non-linear simulations [117, 118] and experiments [119]. These treatments are based on the validity of the diffusion paradigm. However, growing theoretical [120–122], numerical [34, 123] and experimental [124, 125] evidence suggest that, under certain circumstances, the diffusion-advection paradigm may not be valid and that its assumptions need to

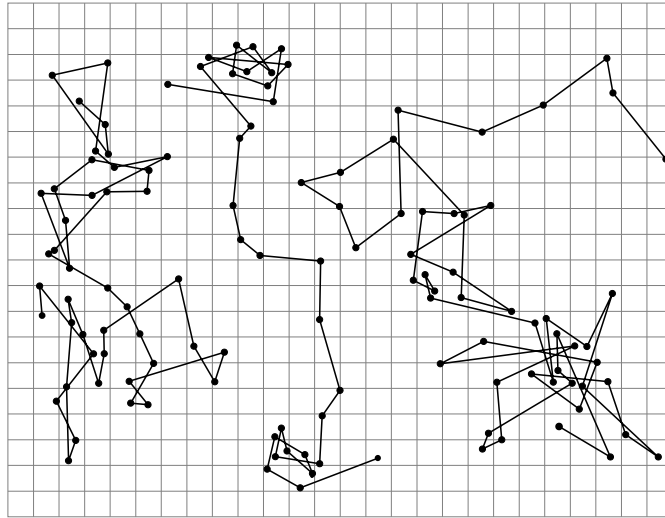


**Figure 4.1** | Example of trajectories of small particles (radius of  $0.53\ \mu\text{m}$ ) in suspension in a fluid measured by Jean Perrin [132]. The successive positions are marked every 30 s and joined by straight lines to guide the eye. The grid size is  $3.2\ \mu\text{m}$ .

be relaxed to describe the turbulent transport in magnetized plasmas, which can be non-local and can exhibit long-range temporal correlations.

In this Thesis, the transport of suprathermal ions in the turbulent plasma of TORPEX is investigated. It is shown that their transport is *non-diffusive*, meaning that it cannot be described in the context of the diffusion-advection paradigm. This Chapter does not aim at presenting a complete review of non-diffusive transport, but rather an introduction to the topic. For more in depth reviews, we recommend the references [126–129]. First, we recall the basics of the classical diffusion model and then we present two approaches of possible generalizations of this model: the CTRW and the fLm.

### 4.1 Classical diffusion and the random walk model

The model of the random walk was first developed by Einstein [112] in 1905 and, independently, by Smoluchowski [113] in 1906, to explain the observation made by a Scottish botanist, Robert Brown (1773-1858), of the random motion of pollen particles in suspension on water. The term *Brownian motion* has been coined in honors of Brown to designate the random walk. In 1913, in his book *Les Atomes* [130], Perrin verified the results of Einstein and Smoluchowski by measuring with a microscope the displacement of small particles in suspension in a liquid. Figure 4.1 reproduces some of his observations. Using Einstein's theory, he was able to measure the Avogadro Number [131]. This remarkable success bore the definite proof of the existence of the atom which awarded Perrin the Nobel Prize for physics in 1926.

Einstein's model of the random walk assumes that each individual particle motion is independent of the other's and that the displacements of the same particle at different times are also

#### 4.1. Classical diffusion and the random walk model

independent, provided that the interval separating the different times is not too small. Next, he introduces a time interval,  $\tau$ , very small compared to the observation time but sufficiently large so that the motions between two consecutive time intervals  $\tau$  can be considered as independent. In a one-dimensional (1D) model, considering  $n$  particles, during the time interval  $\tau$ , each particle position along the  $x$ -axis will increase by a value  $\Delta$ , different for each particle. The PDF of the step sizes  $\varphi(\Delta)$  is defined by the following relation: the number  $dn$  of particle experiencing a displacement lying between  $\Delta$  and  $\Delta + d\Delta$  is given by

$$dn = n\varphi(\Delta) d\Delta. \quad (4.1)$$

The step size probability satisfies the relation  $\varphi(\Delta) = \varphi(-\Delta)$  and differs from zero only for very small values of  $\Delta$ .

Let  $f(x, t)$  be the distribution of particles. Using Eq. (4.1), the number of particles at time  $t + \tau$  found between  $x$  and  $x + dx$  is written

$$f(x, t + \tau) dx = dx \int_{-\infty}^{+\infty} f(x + \Delta, t) \varphi(\Delta) d\Delta. \quad (4.2)$$

Since  $\tau$  is very small, we can write

$$f(x, t + \tau) = f(x, t) + \tau \frac{\partial f}{\partial t}, \quad (4.3)$$

and by expanding  $f(x + \Delta, t)$  in powers of  $\Delta$ , we find

$$f(x + \Delta, t) = f(x, t) + \Delta \frac{\partial f(x, t)}{\partial x} + \frac{\Delta^2}{2} \frac{\partial^2 f(x, t)}{\partial^2 x} + O(\Delta^3). \quad (4.4)$$

We note that, after the assumption of independent time steps and symmetrically distributed step sizes, we assume here that  $\tau$  and  $\Delta$  cannot take large values in order to perform the two previous expansions. This is, as we will see below, a fundamental restriction of the diffusive model which gives it its local character in time and space.

Since only very small values contribute to it, the expansion can be performed under the integral. We find

$$f(x, t) + \tau \frac{\partial f}{\partial t} = f \int_{-\infty}^{+\infty} \varphi(\Delta) d\Delta + \frac{\partial f}{\partial x} \int_{-\infty}^{+\infty} \Delta \varphi(\Delta) d\Delta + \frac{\partial^2 f}{\partial^2 x} \int_{-\infty}^{+\infty} \frac{\Delta^2}{2} \varphi(\Delta) d\Delta + O(\Delta^3). \quad (4.5)$$

All the terms with odd powers of  $\Delta$  vanish due to the fact that  $\varphi(\Delta) = \varphi(-\Delta)$ . Taking into account the fact that  $\int_{-\infty}^{+\infty} \varphi(\Delta) d\Delta = 1$ , defining the variance of the step sizes

$$\langle \Delta^2 \rangle = \int_{-\infty}^{+\infty} \Delta^2 \varphi(\Delta) d\Delta \quad (4.6)$$

and retaining the terms up to  $O(\Delta^3)$ , we find the well-known diffusion equation

$$\frac{\partial f}{\partial t} = D \frac{\partial^2 f}{\partial x^2}, \quad (4.7)$$

where  $D = \frac{\langle \Delta^2 \rangle}{2\tau}$  is the diffusion coefficient. The equation of diffusion had already been discovered experimentally by Fick in 1855, but Einstein was the first to derive it from this physical and atomistic model.

Let us now find the fundamental solution,  $G(x, t)$ , of Eq. (4.7), i.e. the solution of the equation with initial condition  $G(x, t = 0) = \delta(x)$ . This solution is also called the *Green function* or the *propagator* of the equation. Its convolution with an arbitrary initial condition  $f_0(x)$  provides the evolution of the initial condition at all times  $t > 0$

$$f(x, t) = (G * f_0)(x, t) = \int_{-\infty}^{+\infty} G(x - x', t) f_0(x') dx'. \quad (4.8)$$

As we will see later, it is interesting to take the Fourier transform in space of Eq. (4.7)

$$\frac{\partial \hat{G}(k, t)}{\partial t} = -k^2 D \hat{G}(k, t), \quad (4.9)$$

where

$$\hat{G}(k, t) = \int_{-\infty}^{+\infty} e^{-ikx} G(x, t) dx. \quad (4.10)$$

The solution of Eq. (4.9) is

$$\hat{G}(k, t) = C e^{-k^2 D t}. \quad (4.11)$$

As  $\hat{G}(k, 0) = \int_{-\infty}^{+\infty} e^{-ikx} \delta(x) dx = 1$ , we find that  $C = 1$ .

We find the solution by taking the inverse Fourier transform of the previous expression

$$G(x, t) = \frac{1}{2\pi} \int_{-\infty}^{+\infty} e^{-k^2 D t + ikx} dk = \frac{1}{2\pi} \int_{-\infty}^{+\infty} e^{-\left(Dt(k - \frac{ix}{2Dt})^2 + \frac{x^2}{4Dt}\right)} dk. \quad (4.12)$$

After a little effort, one finds that the solution is the Gaussian, or *normal*, distribution

$$G(x, t) = \frac{1}{\sqrt{4\pi D t}} e^{-\frac{x^2}{4Dt}}, \quad (4.13)$$

with a variance, or mean-squared displacement, given by

$$\langle x^2 \rangle = 2Dt. \quad (4.14)$$

The linear time dependence of the mean-square displacement of diffusive processes is a fundamental results of the random walk model.

The fact that the distribution of positions of the random walkers is a Gaussian distribution arises naturally from the central limit theorem (CLT). Indeed, the position of each particle is a sum of independent and identically distributed steps having the same mean and the same variance. Each step being independent, the diffusive process is also memory-less, i.e. Markovian.

## 4.2 Non-diffusive transport

Since its discovery, the model of diffusion and Brownian motion plays a crucial role not only in physics but also in biology, chemistry, sociology, economics and finance. However, numerous examples of transport show a deviation from the diffusive paradigm given by Eq. (4.14). Non-diffusive transport is in fact ubiquitous in nature. Examples range from the dispersal of bank notes [59], the motion of particles inside living cells [61] or the foraging movements of spider monkeys [65]. In plasma physics, examples are also multiple. The acceleration of electrons and ions by interplanetary shocks in the solar wind [50], ion transport across the magnetopause [133], the motion of magnetic bright points on the solar surface [62] or the transport of tracer particles in 3D pressure-gradient driven turbulence [134] are evidences indicating the presence of non-diffusive transport in magnetized plasmas.

Non-diffusive transport is characterized by a mean-squared displacement (variance of displacement) of an ensemble of individuals that does not necessarily scale linearly with time

$$\langle (\mathbf{r}(t) - \langle \mathbf{r}(t) \rangle)^2 \rangle \propto t^\gamma, \quad (4.15)$$

where  $\mathbf{r}(t)$  represents the positions of individuals and  $\gamma$  is called the *transport exponent*. When  $\gamma > 1$  or  $\gamma < 1$ , the transport is called superdiffusive or subdiffusive, respectively. For the special case of classical diffusion,  $\gamma = 1$  in accordance with Eq. (4.14). When  $\gamma = 2$ , the transport is ballistic. Non-diffusive transport is at the heart of many complex systems, such as turbulence, where well-defined scale-lengths or time-scales do not exist, and thus transport cannot be modeled as a classical diffusive process. In these systems, the transport is characterized by the presence of long-term memory and/or non-Gaussian (heavy-tailed) PDFs. Mandelbrot coined the terms Noah effect and Joseph effect [135], as a reference to the natural events experienced by these biblical figures, to describe those two effects in the context of hydrology. The great flood experienced by Noah and the seven years of abundance followed by seven years of famine experienced by Joseph are well known examples that reflect that extreme events with low probability and cycles or trend do, in fact, occur in nature.

In order to account for these effects, the hypotheses of the CLT need to be loosened. By removing the restriction on the finiteness of the variance of the random variables (here, the step sizes), we allow large fluctuations in the random walk. The limiting distributions in this case are given by the *generalized central limit theorem*, due to the work of Lévy, Khintchine, Gnedenko and Kolmogorov [126, 136, 137] in the 1930s. They are called  $\alpha$ -*stable distributions* and are presented

in Appendix A. They are characterized by their *index of stability*,  $\alpha \in (0, 2]$ , and include the Gaussian distribution as a special case, for  $\alpha = 2$ . When  $\alpha < 2$ , they have algebraically decaying heavy tails with exponent  $-(1 + \alpha)$ , and infinite variance. For this reason, they are particularly interesting to model stochastic processes with high variability, such as solar flare intermittency [138]. By removing the hypothesis on the independence of the steps of the CLT, we allow for long-time correlations in the Brownian motion.

In the next section, we introduce the model of the continuous time random walk (CTRW) which is a generalization of the random walk. We give two notable examples of this model, the *Lévy-flight* and the *Lévy-walk*. Finally, we introduce an other model of non-diffusive transport which is based on the Langevin equation of motion and includes long-range temporal correlations, the fractional Brownian motion (fBm) and its generalization to a non-Gaussian, heavy-tailed process, the fractional Lévy motion (fLm).

### 4.2.1 Continuous time random walk

The model of the CTRW was first developed in 1965 by Montroll and Weiss to describe the mobility of charges in amorphous semiconductors [139]. It has since then found a wide range of applications in physics, chemistry, biology, etc. The CTRW supposes that a particle, also called random walker, makes successive jumps interrupted by rests. The step sizes and the waiting times are drawn from a PDF, called the *jump PDF*,  $\psi(x, t)$ . Various choices of the form of  $\psi(x, t)$  lead to different situations. For example, if the step sizes and the waiting times are independent random variables, the CTRW is decoupled and the jump PDF can be written as  $\psi(x, t) = \lambda(x)w(t)$ , where  $\lambda(x)$  and  $w(t)$  are the step size PDF and the waiting time PDF, respectively. In the case of a coupled jump PDF, a jump of a certain length involves a certain duration. This is, for example, the case of the Lévy-walk.

The CTRW can be described by the equation [140]

$$\eta(x, t) = \int_{-\infty}^{+\infty} dx' \int_0^{+\infty} dt' \eta(x', t') \psi(x' - x, t - t') + \delta(x) \delta(t), \quad (4.16)$$

which links the PDF  $\eta(x, t)$  of arriving at position  $x$  at time  $t$  with the PDF  $\eta(x', t')$  of being arrived at position  $x'$  at time  $t'$  with a delta Dirac initial condition.

For the decoupled case, the PDF of the density of walkers is therefore given by

$$n(x, t) = \int_0^t dt' \eta(x, t') \Psi(t - t'), \quad (4.17)$$

where  $\Psi(t) = 1 - \int_0^t w(t') dt'$  is the probability for a walker of making no jumps between the time interval  $(0, t)$ .

By taking the space Fourier transform and time Laplace transform<sup>1</sup> of Eq. (4.17), one finds the

---

<sup>1</sup> In the following we use the notation  $\hat{f}$  for both the Fourier and the Laplace transforms of the function  $f$ . The

*Montroll-Weiss equation*

$$\hat{n}(k, s) = \frac{1 - \hat{w}(s)}{s(1 - \hat{w}(s)\hat{\lambda}(k))}. \quad (4.18)$$

Starting from this equation, the fluid limit, meaning that all details of the CTRW that are irrelevant at very large temporal and spatial scales are neglected, is usually sought to find an equation describing the temporal evolution of the density of random walker.

For example, classical diffusion is found by taking a Gaussian distribution of step sizes and a Poissonian waiting time PDF. In fact, the fluid limit is always found to be the classical diffusion, as long as the characteristic waiting time

$$\tau = \int_0^{+\infty} t w(t) dt \quad (4.19)$$

and the variance of step sizes

$$\Delta^2 = \int_{-\infty}^{+\infty} x^2 \lambda(x) dx \quad (4.20)$$

are finite [127]. In this case the diffusion coefficient is given by  $D = \Delta^2/\tau$ .

To describe non-diffusive transport,  $\lambda$  and  $w$  have to be chosen such that  $\tau$  or  $\Delta^2$ , or both, diverge. A natural choice is to draw both functions in the family of stable distributions (with certain restrictions) since they are the limit of sums of random variables [141]. The non-Gaussian property will arise from a divergent  $\Delta^2$  and the non-Markovianity from a divergent  $\tau$ . In the case where both characteristic scales diverge, we can choose a strictly symmetric stable distribution with characteristic exponent  $\alpha < 2$  for the step sizes distribution and a one-sided stable distribution with characteristic exponent  $\beta < 1$  for the waiting time distribution (see Appendix A):

$$\hat{\lambda}(k) = e^{-\sigma^\alpha |k|^\alpha} \simeq 1 - \sigma^\alpha |k|^\alpha \quad \text{for } k \rightarrow 0 \quad \text{with } \alpha < 2 \quad (4.21)$$

and

$$\hat{w}(s) = e^{-\mu^\beta s^\beta} \simeq 1 - \mu^\beta s^\beta \quad \text{for } s \rightarrow 0 \quad \text{with } \beta < 1, \quad (4.22)$$

with the following asymptotic behavior

$$\lambda(x) \sim x^{-(\alpha+1)}, \quad \text{when } |x| \rightarrow \infty \quad (4.23)$$

and

$$w(t) \sim t^{-(\beta+1)}, \quad \text{when } t \rightarrow \infty. \quad (4.24)$$

difference between the two transforms is indicated by their conjugate variables:  $x \xrightarrow{FT} k$  and  $t \xrightarrow{LT} s$ .

Using those expression in Eq. (4.18) and keeping terms up to first order, one finds

$$\hat{n}(k, s) = \frac{s^{\beta-1}}{s^{\beta} + \frac{\sigma^{\alpha}}{\mu^{\beta}} |k|^{\alpha}}, \quad (4.25)$$

which can be rearranged as

$$s^{\beta} \hat{n}(k, s) - s^{\beta-1} = -\frac{\sigma^{\alpha}}{\mu^{\beta}} |k|^{\alpha} \hat{n}(k, s). \quad (4.26)$$

If  $\alpha = 2$  and  $\beta = 1$ , one recognizes the Laplace transform of the first order time derivative of  $\hat{n}(k, t)$  on the left hand side (lhs) and the Fourier transform of the second order space derivative of  $\hat{n}(x, s)$  on the right hand side (rhs). Therefore, in this case, we recover the classical diffusion equation (Eq. (4.7)) with  $D = \sigma^2 / \mu$ .

In the case were  $\alpha < 2$  and  $\beta < 1$ , the lhs and rhs correspond to generalizations of the differential operator to fractional orders (see Appendix B)

$$\frac{\partial^{\beta}}{\partial t^{\beta}} n(x, t) = D_{\alpha, \beta} \frac{\partial^{\alpha}}{\partial |x|^{\alpha}} n(x, t), \quad (4.27)$$

where  $D_{\alpha, \beta} = \sigma^{\alpha} / \mu^{\beta} [m^{\alpha} / s^{\beta}]$  is a generalized diffusion coefficient. This equation is called the *space and time fractional diffusion equation* and describes the time evolution of the fluid limit of a CTRW with long-term memory (non-Markovian) and long-range spatial correlations (non-Gaussian). When  $\alpha \rightarrow 2$  and  $\beta \rightarrow 1$ , the classical diffusion equation (Eq. (4.7)) is recovered. We call  $\alpha$  the *spatial transport exponent* and  $\beta$  the *temporal transport exponent*. The time derivative operator is the *Caputo fractional derivative* and the space derivative is the *Riesz fractional derivative* (Appendix B).

By using the scaling properties of the Fourier and Laplace transform

$$\mathcal{F}[f(ax)] = |a|^{-1} \hat{f}(k/a) \quad \text{and} \quad \mathcal{L}[f(bu)] = b^{-1} \hat{f}(s/b), \quad b > 0, \quad (4.28)$$

on Eq. (4.25), the following scaling property of the propagator of Eq. (4.27) is inferred

$$G_{\alpha, \beta}(x, t) = t^{-H} K_{\alpha, \beta} \left( \frac{x}{t^H} \right), \quad (4.29)$$

where  $H = \beta / \alpha$  is the *self-similarity index* also called *Hurst exponent* [142],  $K_{\alpha, \beta}$  is called the *reduced Green function* and  $\frac{x}{t^H}$  is the *similarity variable* [129]. This scaling implies that the stochastic process associated with the propagator is *self-similar* with index  $H = \beta / \alpha$  (or  $H$ -self similar). Indeed, if we rescale the time by a factor  $\lambda > 0$ , we find

$$G_{\alpha, \beta}(x, \lambda t) = \lambda^{-H} t^{-H} K_{\alpha, \beta} \left( \frac{x}{t^H \lambda^H} \right) \propto G_{\alpha, \beta}(x \lambda^{-H}, t), \quad (4.30)$$

implying that the motion is invariant under the following transformation

$$(x, t) \mapsto (\lambda^H x, \lambda t). \quad (4.31)$$

The self-similarity of the process leads then to the following scaling of the moments of the distribution with time

$$\langle |x|^s \rangle \propto t^{sH}. \quad (4.32)$$

Indeed, if we assume  $\langle |x|^s \rangle \propto t^K$ , we have

$$\langle |\lambda^H x|^s \rangle \propto (\lambda t)^K \Rightarrow \lambda^{sH} \langle |x|^s \rangle \propto \lambda^K t^K \Rightarrow K = sH. \quad (4.33)$$

By identifying Eq. (4.15) with Eq. (4.32) we see that  $\gamma = 2H$ . The transport is therefore superdiffusive if  $2\beta > \alpha$  and subdiffusive if  $2\beta < \alpha$ . For the special case  $2\beta = \alpha$ ,  $\beta \neq 1$ ,  $\alpha \neq 2$  the transport is called *quasidiffusive* [59] and exhibits the same scaling as the classical diffusion despite the crucial difference of a non-Gaussian PDF and non-Markovian time increments. We would like to point out that only verifying the time dependence of the variance of displacements is not sufficient to conclude that a transport process is diffusive. Whenever possible, the temporal evolution of higher moments, or of the full distribution, should be examined to determine the presence of non-Gaussian features. Evaluating moments of the distribution can be delicate since the integrals that define them do not always converge. For example, the  $s$ -order moments of a  $\alpha$ -stable distributions converges only for  $s < \alpha$  [126]. However, in practice, the temporal scaling can be recovered by taking “truncated” moments or by computing moments of fractional order smaller than  $\alpha$  [127].

### Lévy flight

The Lévy flight is a particular case of the CTRW with a finite characteristic waiting time,  $\tau < \infty$ , but step size distribution given by a symmetric stable distribution with diverging variance,  $\Delta^2 \rightarrow \infty$ . The trajectories of Lévy flights have been shown to model the foraging motions of many living organisms [65, 143]. Mandelbrot also used this model to simulate the fractal galaxy distribution in the Universe [132]. In fact, a fractal dimension  $D = \alpha$  can be assigned to the trajectories. An example of a Lévy flight trajectory is shown in Fig. 4.2.

The Lévy flight can be modeled by taking a Poissonian distribution for the waiting time PDF  $w(t) = \tau^{-1} e^{-t/\tau}$ , with Laplace transform  $\hat{w}(s) = (1 + s\tau)^{-1} \simeq 1 - \tau s$ , for  $s \rightarrow 0$ . Using this in Eq. (4.18), we find

$$\hat{G}_\alpha(k, s) = \frac{1}{s + \frac{\sigma^\alpha}{\tau} |k|^\alpha}, \quad (4.34)$$

which, upon Fourier-Laplace inversion, shows that the propagator of the Lévy flight is a

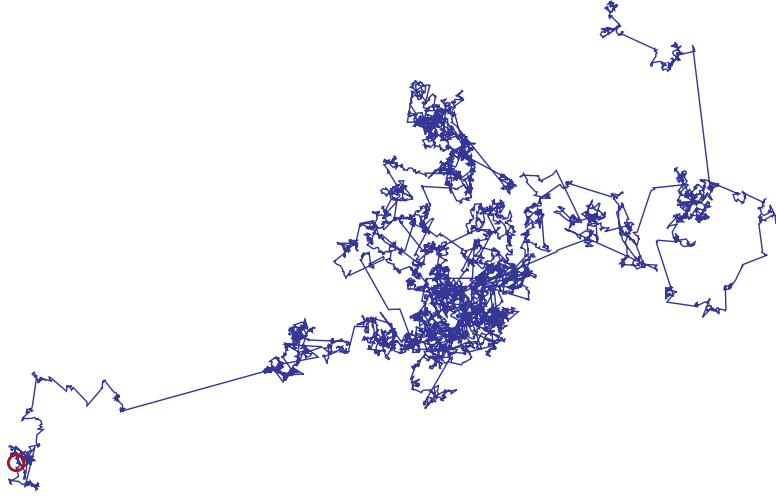


**Figure 4.2** | Example of a Lévy flight trajectory with  $\alpha = 1.5$ . Contrary to the Brownian motion (Fig. 4.1), arbitrary long steps can arise, on all scale length, leading to the clustering nature of the Lévy flight.

symmetric stable distribution

$$G(x, t) = t^{-H} L_{\alpha, \sigma} \left( \frac{x}{t^H} \right), \quad (4.35)$$

with a self-similar index  $H = 1/\alpha$ . Rearranging the terms of Eq. (4.34) and Fourier-Laplace inverting it, we find the *space fractional diffusion equation*

$$\frac{\partial}{\partial t} n(x, t) = D_\alpha \frac{\partial^\alpha}{\partial |x|^\alpha} n(x, t) \quad (4.36)$$

describing the Lévy flight.

The Lévy flight results in a superdiffusive process (with the exception of the case  $\alpha = 2$ ) with a diverging mean-square displacement  $\langle x^2 \rangle \rightarrow \infty$  for  $\alpha < 2$ .

The presence of arbitrary long jumps without any restriction on the step duration leads to rather unphysical situations [127, 128]. One way of solving this is introduced in the Lévy walk model, which is often more appropriate to describe physical systems.

### Lévy walk

Similarly to the Lévy flight, the Lévy walk model maintains a diverging variance of distribution of step sizes. However, a coupling between the step sizes and the step duration is included in the jump pdf such that [140]

$$\psi(x, t) = \lambda(x) \delta(|x| - vt^\nu), \quad (4.37)$$

where  $\lambda(x) \rightarrow |x|^{-\mu}$  as  $|x| \rightarrow \infty$  and  $v$  is a generalized velocity which penalizes long jumps such that the variance is finite [128]. Depending on the values of the two exponent  $\mu$  and  $\nu$  the transport can be either superdiffusive or subdiffusive. Due to the coupled form of the jump pdf, the derivation of a transport equation describing the evolution of the PDF has only been achieved recently in the case  $\nu = 1$ , by using a fractional version of the material derivative [144].

The Lévy walk model has been applied to the suprathreshold ion transport in TORPEX [145] and is presented in Section 5.2.2. However, important features of the transport of suprathreshold ions in TORPEX, such as its asymmetry and the temporal correlations, not present in the Lévy walk model as lead to the development of an other model, the fractional Lévy motion (fLm), presented in the following section.

### 4.2.2 Langevin approach

A microscopic description of Brownian motion equivalent to the one of Einstein presented in Section 4.1 was introduced by Langevin in 1908 [114]. An uncorrelated Gaussian noise, representing the random force due to the interaction with the fluid molecules, is used in the equation of motion of a test particle. The equation of motion becomes a stochastic equation, whose average motion shows the same diffusive scaling. Fractional Brownian motion (fBm) introduces long-range temporal dependence in the Gaussian noise, which can lead to a non-linear scaling of the positional variance. On the other hand, non-Gaussian statistics can be introduced by choosing a non-Gaussian noise. For example, stable Lévy motion [126] replaces the Gaussian noise with a random noise distributed according to a Lévy stable distribution with heavy-tails (Appendix A).

The classical Langevin equation is written [114]

$$m\ddot{x}(t) = -m\gamma\dot{x}(t) + \xi(t), \quad (4.38)$$

where  $m$  is the mass of the test particle,  $\gamma$  is the friction coefficient and  $\xi(t)$  is the random force due to the random collisions with the surrounding particles. In the case of the Brownian motion,  $\xi(t)$  is a white noise, i.e. a Gaussian noise with an infinitely short correlation time:  $\langle \xi(t_1)\xi(t_2) \rangle = C\delta(t_1 - t_2)$ , where  $C$  is a constant. In Eq. (4.38), the forces acting on the particle are separated in two groups, the macroscopic, slowly varying ones, represented by the dissipative force  $-m\gamma v$ , and the microscopic, rapidly varying ones, represented by the fluctuating force  $\xi(t)$ .

If the time scale of the particle motion is comparable to the time scale of the collisions, the assumption of a white noise and a constant friction have to be abandoned. This leads to the generalized Langevin equation (GLE) [146]

$$\ddot{x}(t) = - \int_0^t \beta(t-t')\dot{x}(t') dt' + \xi(t), \quad (4.39)$$

where  $m = 1$  is used for simplicity. Here,  $\beta(t)$  is the memory kernel and  $\xi(t)$  is the random force which is zero-centered and stationary, i.e.  $\langle \xi(t_1)\xi(t_2) \rangle = C(|t_1 - t_2|) = C(\tau)$ . The fluctuation-dissipation theorem [146–149] states that the dissipation is the macroscopic manifestation of the disordering effect of the fluctuations and relates the correlation function of the random forces  $C(t)$  with  $\beta(t)$  by

$$k_B T \beta(t) = C(t). \quad (4.40)$$

Assuming  $x(0) = 0$ ,  $v(0) = v_0$  and Laplace transforming Eq. (4.39), we find

$$\hat{x}(s) = \frac{v_0 + \hat{\beta}(s) + \hat{\xi}(s)}{s(s + \hat{\beta}(s))}, \quad (4.41)$$

where  $\hat{\beta}(s)$  and  $\hat{\xi}(s)$  are the Laplace transforms of  $\beta(t)$  and  $\xi(t)$ . Upon Laplace inversion, one finds the equation of the particle position

$$x(t) = v_0 H(t) + \int_0^t H(t-t') \xi(t') dt', \quad (4.42)$$

where  $H(t)$  is the relaxation function [149] defined by its Laplace transform

$$\hat{H}(s) = \frac{1}{s(s + \hat{\beta}(s))}. \quad (4.43)$$

We note that, in accordance with the classical Langevin equation, if  $\beta(t) = \gamma = \text{cste.}$ , the relaxation function,  $H(t) = \frac{1}{\gamma}(1 - e^{-\gamma t})$ , is exponentially decaying and the position is given by

$$x(t) = \frac{v_0}{\gamma}(1 - e^{-\gamma t}) + \frac{1}{\gamma} \int_0^t (1 - e^{-\gamma(t-t')}) \xi(t') dt'. \quad (4.44)$$

For  $t \rightarrow 0$  the ballistic motion  $x(t) = v_0 t$  is recovered and for  $t \gg \gamma^{-1}$ ,

$$x(t) = \frac{v_0}{\gamma} + \frac{1}{\gamma} \int_0^t \xi(t') dt'. \quad (4.45)$$

When  $v_0 = 0$ , Eq. (4.45) is referred to as ordinary Brownian motion (oBm).

If we take  $\xi$  as a white noise and  $\langle v_0 \rangle = 0$ , the variance of the displacement is given by

$$\begin{aligned}
 \langle x^2(t) \rangle &= \frac{1}{\gamma^2} \left\langle \int_0^t \xi(t-t_1) dt_1 \int_0^t \xi(t-t_2) dt_2 \right\rangle \\
 &= \frac{1}{\gamma^2} \left\langle \int_0^t dt_1 \int_0^t dt_2 \xi(t-t_1) \xi(t-t_2) \right\rangle \\
 &= \frac{1}{\gamma^2} \int_0^t dt_1 \int_0^t dt_2 \langle \xi(t-t_1) \xi(t-t_2) \rangle \\
 &= \frac{1}{\gamma^2} \int_0^t dt_1 \int_0^t dt_2 C \delta(t_2 - t_1) \\
 &= \frac{1}{\gamma^2} \int_0^t C dt_1 = \frac{C}{\gamma^2} t = \frac{k_B T}{\gamma} t,
 \end{aligned} \tag{4.46}$$

where we used Eq. (4.40). Thus, we recover the linear temporal scaling of the mean-squared displacement of the classical diffusion (Eq. (4.14)).

### Fractional Brownian motion

Fractional Brownian motion (fBm) was proposed by Mandelbrot and Van Ness in 1968 [150] to model the variations of cumulated water flows in the great lakes of the Nile river basin observed by Hurst [151]. Hurst studied the record of river level and other physical quantities such as rainfall, temperature, pressure, the growth of tree rings, sunspot numbers and wheat prices. He found that the range of those records, rescaled by their standard deviation, is proportional to  $t^H$ , where  $t$  is the time and  $1/2 < H < 1$  is, ever since, called the Hurst exponent. Since then, it has found a wide range of applications in systems showing long time interdependence.

Slightly different representations exists in the literature, here we use the following [152]

$$x_H(t) = \frac{1}{\Gamma(H + 1/2)} \int_0^t (t-t')^{H-1/2} \xi(t') dt', \tag{4.47}$$

where  $x_H(t)$  represents the position of a particle experiencing fBm,  $\xi(t)$  is a Gaussian uncorrelated noise,  $H \in (0, 1]$  and  $\Gamma(\cdot)$  is the gamma function. FBm is constructed as a moving averaged of the ordinary Brownian motion (oBm) (Eq. (4.45)), in which past increments are weighted by the power law kernel  $(t-t')^{H-1/2}$ . It has a zero mean  $\langle x_H(t) \rangle = 0$  for  $H < 1$ . From its definition and the fact that the Gaussian noise is self-similar with exponent  $1/2$ , it follows that  $x_H(t)$  is  $H$ -self similar (Eq. (4.31)) and that it has stationary increments,  $x_H(t) - x_H(s) = x_H(t-s)$  [126]. Using these two properties, we can show that the correlation function is

$$\begin{aligned}
 \langle x_H(t) x_H(s) \rangle &= K_H \frac{1}{2} \{ \langle x_H^2(t) \rangle + \langle x_H^2(s) \rangle - \langle (x_H(t) - x_H(s))^2 \rangle \} \\
 &= K_H \frac{1}{2} \{ \langle x_H^2(t) \rangle + \langle x_H^2(s) \rangle - \langle x_H^2(t-s) \rangle \} \\
 &= K_H \frac{1}{2} \{ t^{2H} + s^{2H} - |t-s|^{2H} \},
 \end{aligned} \tag{4.48}$$

where  $K_H$  is a positive constant and where we recall that for a  $H$ -self similar process, the variance scales with time as

$$\langle x_H^2(t) \rangle \propto t^{2H}. \quad (4.49)$$

We note that fBm is subdiffusive for  $0 < H < 1/2$ , superdiffusive for  $1/2 < H < 1$ , ballistic for  $H = 1$  and correspond to oBm for  $H = 1/2$ .

The increments of the fBm,  $\xi_H(t)$ , is a stationary Gaussian process known as fractional Gaussian noise (fGn) and defined as

$$x_H(t) = \int_0^t \xi_H(t') dt'. \quad (4.50)$$

The correlation function,  $C_H(t)$ , of  $\xi_H(t)$  is given by the derivative of equation (4.48) with respect to  $t$  and  $s$

$$C_H(|t-s|) = \langle \xi_H(t)\xi_H(s) \rangle = 2K_H H(2H-1)|t-s|^{2H-2} + 2K_H H|t-s|^{2H-1}\delta(t-s). \quad (4.51)$$

We note that  $C_H(|t-s|)$  behaves as a power law for  $\tau = |t-s| \rightarrow \infty$  and recovers the ordinary Brownian behavior,  $C_H(|t-s|) = K_{1/2}\delta(t-s)$ , for  $H = 1/2$ .

The function  $C_H(\tau)$  tends to zero for  $\tau = |t-s| \rightarrow \infty$  for  $0 < H < 1$ , but when  $1/2 < H < 1$ ,  $\xi_H(t)$  exhibits long-range dependence, i.e.  $C_H(\tau)$  tends to zero so slowly that  $\int_0^\infty C_H(\tau) d\tau = \infty$ . It is said to be *correlated*. For  $0 < H < 1/2$ , there is no long-range dependence, but the coefficient  $(2H-1)$  is negative [126]. In this case the  $\xi_H(t)$  is said to be *anti-correlated*. Figure 4.3 shows three examples of fBm trajectories.

In the framework of the generalized Langevin equation (GLE), it is possible to find the fBm as a solution by using a random force with long-range correlations, namely with a power-law correlation function. The memory kernel,  $\beta(t)$ , is then found with the fluctuation-dissipation theorem (Eq. (4.40)) and, consequently, also have a power-law form. When the random force is chosen to be the fractional Gaussian noise (fGn), the GLE can be written as a fractional differential equation [153], however, the solution of this equation is limited to the subdiffusive and diffusive case. From the physical point of view, the superdiffusive case is found only when the random force is “external”, meaning that the fluctuation-dissipation theorem does not hold and that the driving noise and the dissipation may have different origins, which may be the case in nonequilibrium systems [149].

It is possible to find the propagator of the fBm by using the method of path integrals [152], borrowed from quantum mechanics (note that Shrödinger’s equation resembles a diffusion equation with an imaginary diffusion coefficient). The propagator, given by

$$G_H(x, t) = \sqrt{\frac{H}{\pi}} \frac{\Gamma(H+1/2)}{t^H} \exp \left[ -H\Gamma^2(H+1/2) \frac{x^2}{t^{2H}} \right], \quad (4.52)$$

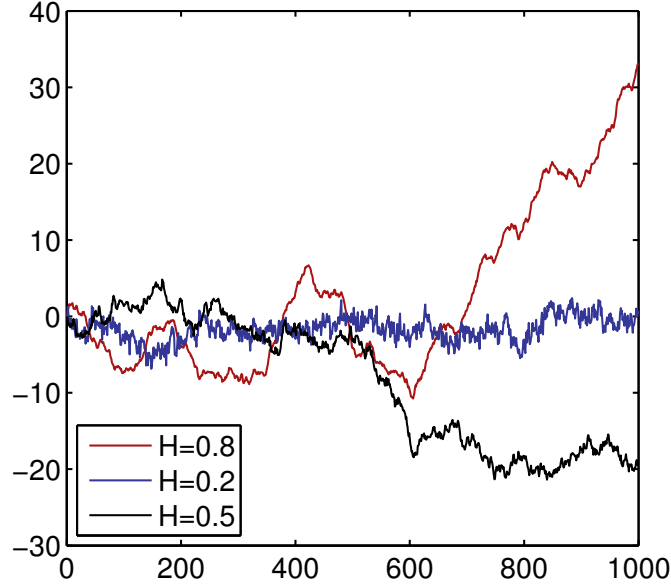


**Figure 4.3** | Examples of realizations of the fractional Brownian motion (fBm) for different values of the self-similar index  $H$ . For  $H = 0.8$ , the increments of the trajectory are positively correlated which results in a persistent motion. The oBm with uncorrelated increments is retrieved for  $H = 0.5$  and for  $H = 0.2$ , the increments of the trajectory are anti-correlated which results in a anti-persistent motion.

is a Gaussian function with a variance proportional to  $t^{2H}$ . It has the same form than the propagator of the oBm (Eq. (4.13)) but with a “stretched” time  $t^{2H}$ . The transport equation of the fBm is easily found from the Fourier transform of Eq. (4.52) to be

$$\frac{\partial}{\partial t} n(x, t) = D_{\beta} t^{\beta-1} \frac{\partial^2}{\partial x^2} n(x, t), \quad (4.53)$$

where  $0 < \beta = 2H < 2$  and  $D_{\beta} = (2\Gamma^2(H + 1/2))^{-1}$  is a stretched diffusion coefficient of dimensions  $[m^2/s^{\beta}]$ . This equation is called the *stretched time diffusion equation* [154]. By using the rule

$$\frac{\partial}{\partial t^{\beta}} = \beta t^{\beta-1} \frac{\partial}{\partial t}, \quad (4.54)$$

it can be interpreted as the result of the classical diffusion equation with a stretched time.

We note that the Langevin approach and the CTRW approach are not equivalent in the non-Markovian case. Equation (4.53) is local in time, whereas Eq. (4.27) with  $\alpha = 2, \beta < 1$ , the *time-fractional diffusion equation*, is not. In the fBm case, the non-Markovian character is provided by a time dependent diffusivity  $D = D_0 t^{\beta-1}$ . Moreover, The solution of Eq. (4.53) is Gaussian, while the solution of the time-fractional diffusion equation is not; it is given by the transcendental functions known as the M-Wright function which tends to the Gaussian function for  $\beta = 1$  [154].

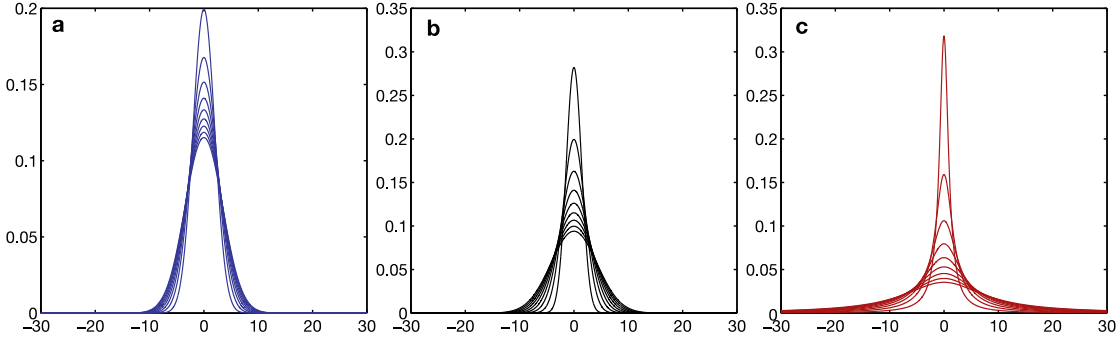


**Figure 4.4** | Examples of propagators for different parameters of the fLm for times  $t_i = 1, 2, \dots, 9$  and effective diffusivity  $K = 1$ . **a:** Subdiffusive case with  $\alpha = 2$  (Gaussian) and  $\beta = 0.5$  (anti-correlated) ( $H = 0.25$ ). **b:** Diffusive case with  $\alpha = 2$  (Gaussian) and  $\beta = 1$  (uncorrelated) ( $H = 0.5$ ). **c:** Superdiffusive case with  $\alpha = 1$  (Lévy stable) and  $\beta = 1$  (uncorrelated) ( $H = 1$ ).

### Fractional Lévy motion

Here, we discuss the fractional Lévy motion (fLm), which is a generalization of the fBm, including both long-range temporal dependence and non-Gaussian statistics.

The stochastic equation defining the fLm process is [155, 156]

$$x_{\alpha,H}(t) = \frac{1}{\Gamma(H - 1/\alpha + 1)} \int_0^t (t - t')^{H-1/\alpha} \xi_{\alpha,\sigma}(t') dt', \quad (4.55)$$

where  $\xi_{\alpha,\sigma}(t)$  is an uncorrelated noise distributed according to a Lévy symmetric, strictly stable distribution, with index of stability  $\alpha$ , ( $0 < \alpha \leq 2$ ) and scale parameter  $\sigma$ . From the properties of  $\alpha$ -stable random variable, we have  $x_{\alpha,H}(\lambda t) = \lambda^H x_{\alpha,H}(t)$ , with  $H = \beta/\alpha$ . Therefore, the fLm belongs to the important family of  $H$ -self similar process with stationary increments (also abbreviated  $H$ -*sssi*), like the fBm. Consequently, the moments of  $x_{\alpha,H}(t)$  exhibit the desired general non-classical feature

$$\langle |x_{\alpha,H}(t)|^s \rangle \propto t^{sH}, \quad (4.56)$$

where  $0 < s < \alpha$ , to ensure convergence of the moments. For a non-degenerated process, the values of  $H$  are restricted to [126]

$$\begin{cases} 0 < H \leq 1/\alpha & \text{if } \alpha < 1, \\ 0 < H \leq 1 & \text{if } \alpha \geq 1. \end{cases} \quad (4.57)$$

The long-term memory is engendered by the convolution with the power-law kernel and the non-Gaussian statistics by the Lévy noise. The fLm generalizes the fractional Brownian motion (fBm) [150]. Indeed, for  $\alpha = 2$ , the noise has a Gaussian distribution and the process is the fBm. When  $H = 1/\alpha$  the process is time-uncorrelated and when  $H < 1/\alpha$  or  $H > 1/\alpha$  the process exhibits negative or positive time correlations, respectively. Therefore, for  $\alpha = 2$  and  $H = 1/2$ , one recovers the oBm corresponding to classical diffusion (Eq. (4.45)).

Using path integrals, Calvo, Sánchez and Carreras have shown that the transport equation of the fLm process is a *space-fractional diffusion equation* with time dependent diffusivity [156]

$$\frac{\partial}{\partial t} n(x, t) = K t^{\beta-1} \frac{\partial^\alpha}{\partial |x|^\alpha} n(x, t). \quad (4.58)$$

Here  $n(x, t)$  is the density of particles,  $K$  is an effective diffusion coefficient and  $\alpha$  and  $\beta$  are the space and time transport exponents, respectively, with  $H = \beta/\alpha$ . The space derivative of order  $\alpha$  is the Riesz fractional differential operator [157] (Appendix B). The restriction on the range of permissible values for  $H$  (Eq. (4.57)) translates for  $\beta$  as

$$\begin{cases} 0 < \beta \leq 1 & \text{if } \alpha < 1, \\ 0 < \beta \leq \alpha & \text{if } \alpha \geq 1. \end{cases} \quad (4.59)$$

When  $\beta < 1$  or  $\beta > 1$  the process is negatively or positively time correlated,  $\beta = 1$  corresponding to an uncorrelated process.

The propagator of Eq. (4.58) is a Lévy distribution which depends on  $x/t^H$  [156]

$$G_{\alpha,\beta}(x, t) = \frac{C(\alpha, \beta)}{t^{\beta/\alpha}} L_{\alpha,\sigma} \left[ C(\alpha, \beta) \frac{x}{t^{\beta/\alpha}} \right], \quad (4.60)$$

where  $C(\alpha, \beta) = \beta^{1/\alpha} \Gamma\left(\frac{\beta-1}{\alpha} + 1\right)$  and  $\sigma = K^{1/\alpha} \Gamma\left(\frac{\beta-1}{\alpha} + 1\right)$ .

Again, for  $\alpha = 2$  the space-fractional derivative becomes a second order derivative and the propagator is a Gaussian corresponding to the case of the fBm (Eq. (4.52) and Eq. (4.53)). For  $\alpha = 2$  and  $\beta = 1$  ( $H = 1/2$ ), Eq. (4.58) becomes the classical diffusion equation and the propagator has the well known form of a Gaussian with variance growing linearly with time (Eq. (4.7) and Eq. (4.13)). Finally, for  $\beta = 1$  and  $\alpha < 2$ , Eq. (4.60) and Eq. (4.58) are Markovian and correspond to the propagator and transport equation of the Lévy flight (Eq. (4.35) and Eq. (4.36)). Examples of fLm propagators are shown in Fig. 4.4 and the different transport regimes of the fLm, as a function of  $\alpha$  and  $\beta$  are summarized in Fig. 4.5.

In this Thesis, we have compared the fLm model with the PDF of the suprathermal ion radial position (Chapter 6). The model that we developed allow the PDF to have a non-zero skewness. We have also derived, for the first time, the transport equation of the fLm with skewness.

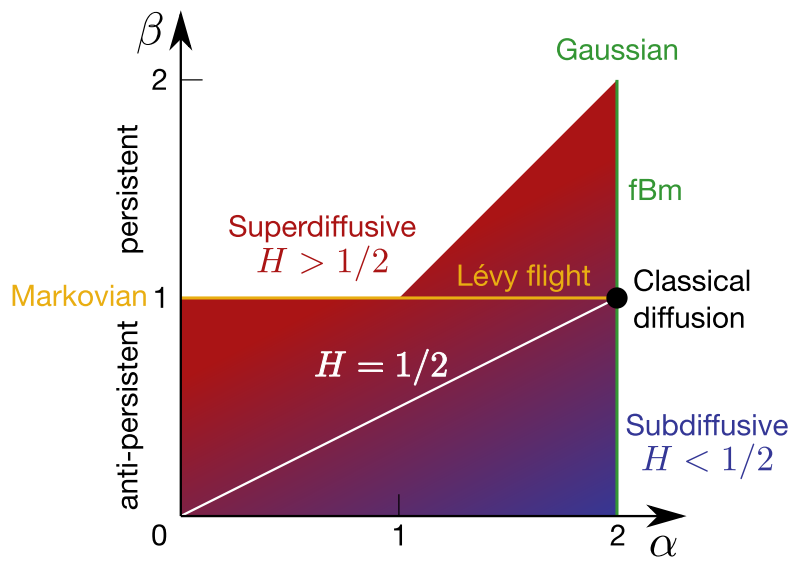


**Figure 4.5** | Parameter space for the fLm. The values of  $H = \beta/\alpha$  lie in the shaded region and depending on the values of the spatial transport exponent,  $\alpha$ , and the temporal transport exponent,  $\beta$ , the transport can be superdiffusive ( $H > 1/2$ ) or subdiffusive ( $H < 1/2$ ). Diffusive transport is found for  $H = 1/2$  (white line), the classical diffusion corresponding to the case  $\beta = 1$  and  $\alpha = 2$  (black dot). Gaussian transport is found for  $\alpha = 2$  and Markovian transport for  $\beta = 1$ . For  $\beta > 1$  the motion is persistent and for  $\beta < 1$  it is anti-persistent. The fBm (green line) is found for  $\alpha = 2$  and  $0 < \beta < 2$  and the Lévy flight (yellow line) for  $\alpha < 2$  and  $\beta = 1$ . A similar figure can be drawn for the CTRW, but with the difference that the non-Markovianity is not due to persistence or anti-persistence but to the non-locality in time and, in this case,  $\beta \leq 1$ .

## 5 Numerical simulations

This Chapter presents the numerical simulations used to model the plasma dynamics in TORPEX and the propagation of suprathermal ions in the turbulent plasma. The global Braginskii solver (GBS) code has been developed in the last few years to model the plasma turbulence in the tokamak SOL. It evolves full profiles of fluid quantities without separating the perturbations from the equilibrium by solving the drift-reduced Braginskii's equations. The suprathermal ion simulations are performed by injecting tracers in the turbulent electric field generated by the GBS simulations. The tracer trajectories are computed by solving the Newton equation of motion. We present the results of a investigation of the suprathermal ion transport in TORPEX and some considerations about the simulations used for the comparison with the experiment.

### 5.1 Fluid simulations of the turbulence

Owing to the open magnetic field lines of the SMT configuration and the low heating power, TORPEX plasmas are characterized by relatively low temperatures. Collisions usually play an important role in low temperature plasmas allowing the local thermodynamic equilibrium to be reached relatively rapidly. This motivates the use of a fluid model to describe the plasma dynamics. In a fluid model, instead of solving the Boltzmann equation for the full particle distribution functions as in kinetic models, the equations for a number of moments of the distribution functions are computed by taking moments of the Boltzmann equation. The first three moments of the particle distribution functions provide the density, velocity and temperature for each species. As each equation usually includes higher moments, an additional equation is usually needed to close the set of fluid equations.

For the fluid approximation to be valid, the time taken and the distance traveled by the particles between collisions must be small compared to the time and distance over which the macroscopic quantities vary. Under these conditions, the distribution functions can be approximated with Maxwellian distributions. In TORPEX, for hydrogen plasmas with the parameters reported in Table 2.1, the collision frequencies for energy and momentum transfer

(for thermalization and isotropization) are

$$\nu_i = \frac{1}{3} \frac{1}{\sqrt{\pi}} \frac{Z^2 e^4 \ln \Lambda}{4\pi\epsilon_0} \frac{n_i}{m_i^{1/2} T_i^{3/2}} \gtrsim 7 \text{ kHz}, \quad (5.1)$$

$$\nu_e = \frac{1}{3} \frac{1}{\sqrt{\pi}} \frac{Z^2 e^4 \ln \Lambda}{4\pi\epsilon_0} \frac{n_i}{m_e^{1/2} T_e^{3/2}} \simeq 72 \text{ kHz} \quad (5.2)$$

where  $\nu_i$  and  $\nu_e$  are the frequencies for ion-ion collisions and electron-electron collisions, respectively. We have  $\nu_e \gg \nu_i > f_{\text{int}}$  where  $f_{\text{int}}$  is the frequency of the interchange mode (of the order of magnitude of a few kHz) representing the typical frequency of the variation of macroscopic quantities. For strongly magnetized plasmas such as in TORPEX ( $f_{ce} \gg \nu_e, f_{ci} \gg \nu_i$ ), the distances perpendicular and parallel to the magnetic field between collisions are given by the Larmor radius of the particles and the mean free path between collisions, respectively. Looking at Table 2.1, we have  $\rho_{i,e} \ll L_{\perp}$  where  $L_{\perp} \simeq L_n \simeq 6 \text{ cm}$ . The parallel distances between collisions,  $\lambda_{\text{mfp},e} = \nu_{\text{th},e}/\nu^e \simeq 9 \text{ m}$  and  $\lambda_{\text{mfp},i} = \nu_{\text{th},i}/\nu^i \simeq 1.5 \text{ m}$  should be much smaller than the magnetic field connection length  $L_{\parallel} = L_c \simeq 2\pi R_0 N$ . For a number of field line turns  $N = 2$ ,  $L_{\parallel} \simeq 12.5 \text{ m}$ . The hypothesis justifying the use of a fluid model are not all perfectly satisfied. Indeed, suprathermal electrons are presents in TORPEX plasmas. Measurements of the electron energy distribution [68] show that a fraction of the electrons accelerated at the EC and UH resonances does not have time to thermalize. The collisions with neutrals are also important in TORPEX, which is in regime of weakly ionized plasmas. The ion-neutral and electron-neutral collision frequencies are [84]  $\nu_{in} \simeq 10 \text{ kHz}$  and  $\nu_{en} \simeq 1 \text{ MHz}$ . Their role in the thermalization of electrons has not been studied yet but, since the collisions between electrons and neutrals are almost elastic, they are thought to play a minor role. At present, the effect of neutrals are included in GBS only through the plasma resistivity. Despite these potentially significant departures from the conditions in which a fluid approximation would be fully justified, a thorough validation exercise of the GBS simulations with TORPEX experimental data has shown that the 2D version of the code correctly models the dynamics of the ideal-interchange regime and the 3D version captures the resistive-interchange regime [90, 91]. Effort to couple a kinetic model of the neutrals, that includes ionization, recombination and charge-exchange processes, to GBS has started [158].

Braginskii's equations [159] are a closed set of two-fluid equations describing the evolution of the electron and ion densities, velocities and temperatures on time scales ranging from the electron Larmor scale to the confinement time scale. The GBS code is based on the drift-reduced Braginskii equations [86, 87, 89, 160] in the cold ion limit (in TORPEX  $T_i \ll 10 \text{ eV}$ ) and for electrostatic fluctuations (in TORPEX, the ratio of the plasma pressure to the magnetic pressure is  $\beta \simeq 10^{-6}$ ). The drift-reduced approximation consists of eliminating the fastest time scale of the electron and ion gyromotion by assuming  $\frac{d}{dt} \ll f_{ci}$ , such that only the particle drifts remain in the equations describing the perpendicular motion [161]. The 3D GBS model consists of a set of five self-consistent equations describing the evolution of the plasma

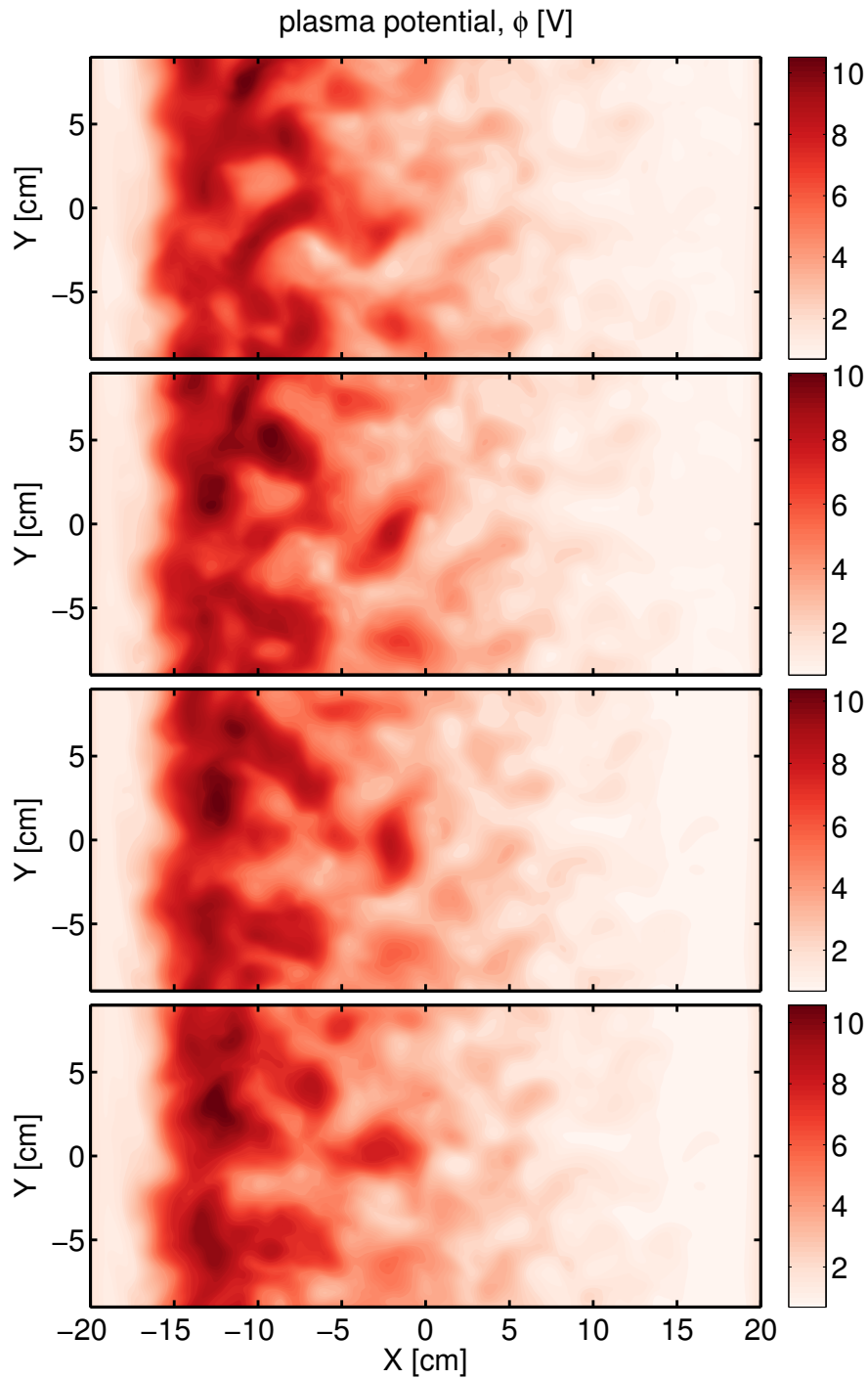


**Figure 5.1 | Consecutive snapshots of the plasma potential  $\phi$  [V] from 2D GBS simulations.** The ideal-interchange mode is located at  $X \sim -10$  cm with a maximum vertical wave-length equal to the vertical spatial domain length  $\lambda_v = 18$  cm and blobs moving radially outward are visible. Periodic boundary conditions are applied in the vertical direction.

density,  $n$ , the vorticity  $\omega = \nabla_{\perp} \phi$  (where  $\phi$  is the plasma potential), the electron and ion parallel velocities,  $V_{\parallel e}$  and  $V_{\parallel i}$ , and the electron temperature,  $T_e$ , which can be applied to different geometries with open field lines (SMT or tokamak SOL). The equations of the 2D version of GBS, reported in Appendix C, are obtained by integrating the 3D equations along the magnetic field lines. They evolve the line-integrated density, vorticity and electron temperature. They take into account diffusion, convection by the  $\mathbf{E} \times \mathbf{B}$  velocity and magnetic curvature. We refer the reader to Joaquim Loizu's PhD Thesis [161] for a detailed description of the model and its equations. Figure 5.1 shows snapshots of the plasma potential,  $\phi$  or  $V_{\text{pl}}$ , from a 2D GBS simulation for the SMT configuration in the ideal-interchange regime. Periodic boundary conditions are used in the vertical direction. The horizontal direction represents TORPEX radial direction. Similarly to TORPEX plasmas, the ideal-interchange mode is located in the HFS, at  $X \simeq -10$  cm, and the region defined by  $X \gtrsim -5$  cm is characterized by the presence of intermittent blobs.

### 5.1.1 Comparison of GBS simulations with TORPEX plasmas

To model the suprathermal ion transport, suprathermal ions are injected in the turbulent plasma potential modeled with GBS. Figure 5.2 shows time-averaged radial profiles and fluctuations profiles of  $V_{\text{pl}}$ ,  $T_e$  and  $n_e$ , measured with the five-tip triple probe FRIPLE, together with the same quantities computed from a GBS simulation. The particle and heat sources in GBS were varied to have the best match between the experimental and simulated plasma potential in the region where the suprathermal ions propagate:  $-5 \text{ cm} \lesssim X \lesssim 5 \text{ cm}$ . The details of the simulation parameters are reported in Appendix C. A very good match of the value, the gradient and the fluctuations is visible. The positions of the maxima of the experimental profiles match the position of the maxima of the simulated profiles. However, a discrepancy between the maximum values of the  $V_{\text{pl}}$  and  $T_e$  profiles is apparent. This is due to the presence of suprathermal electrons at the positions of the EC and UH resonances, which perturb the measurement with Langmuir probes.

## 5.2 Suprathermal ion simulation model

Numerical modeling of suprathermal ion transport in TORPEX is performed by computing the ion full trajectories in the turbulent electrostatic field generated by 2D GBS simulations. The equation of motion is

$$\frac{d\mathbf{v}}{dt} = \frac{q}{m} (\mathbf{E} + \mathbf{v} \times \mathbf{B}), \quad (5.3)$$

where the electrical field is time dependent,  $\mathbf{E}(x, y, t) = -\nabla\phi(x, y, t)$ , and the magnetic field is static,  $\mathbf{B} = \mathbf{B}(x, y)$ . Suprathermal ions are treated as tracers, i.e. they do not influence the fields through Poisson's equation or Ampere's Law. This is a reasonable approximation since in the experiments their density is very small compared to that of the plasma. Considering

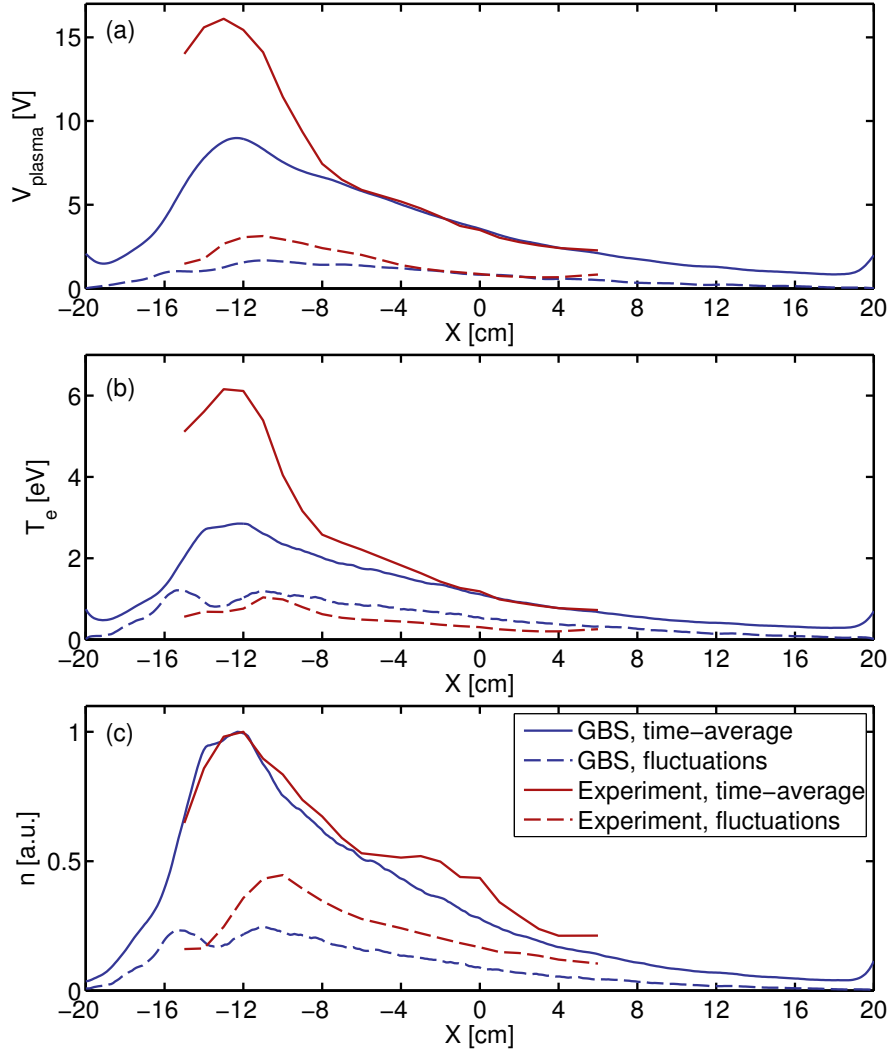


**Figure 5.2** | Comparison of the radial profiles of the time-averaged and fluctuating (computed as the standard deviation) of (a) plasma potential, (b) electron temperature and (c) density from the experiment and from the simulations.

70 eV ions, a current  $I = 10\mu\text{A}$  and a beam radius  $d = 2$  cm, an estimate of the suprathermal ion density is given by

$$n = \frac{I}{qvA} = \sqrt{\frac{m}{2E}} \frac{I}{q\pi r^2} \approx 1 \times 10^{12} \text{ m}^{-3} \ll n_e, \quad (5.4)$$

where  $E$  is the energy of the ions,  $m$  their mass,  $q$  their charge and  $v$  their velocity. Coulomb collisions with thermal ions and neutral particles are neglected. The computation of the respective collision frequencies and mean free paths is presented in Appendix D. The full gyro-orbit is computed to correctly describe the effects of turbulence on the suprathermal ions across spatial and temporal scales, including those comparable to their Larmor radii and cyclotron frequency. All initial parameters of the suprathermal ion injection, namely, position,

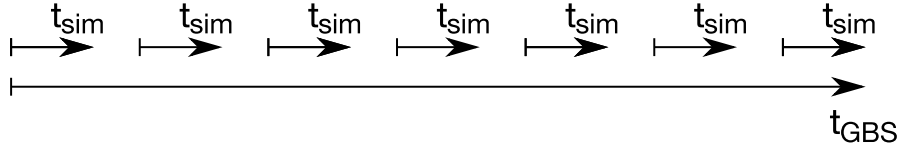


**Figure 5.3** | Representation of the method used to have the suprathermal ions sample different realizations of the GBS turbulence. The injected suprathermal ions are separated in different bins (represented by the arrows on the top) and each bin is injected at a different time in the turbulence (represented by the arrow on the bottom). The time of the GBS simulations is indicated by  $t_{\text{GBS}}$  and the time of the suprathermal ions simulations by  $t_{\text{sim}}$ .

energy and orientation, are modeled using Gaussian distributions. The averaged injection energy, normalized to the mean of the electron temperature at the injection position, is denoted by  $\mathcal{E} \equiv E/\bar{T}_e$ . The relative amplitude of the turbulent fluctuations is varied *a posteriori* in order to describe the dependence of the suprathermal ion transport on the turbulence amplitude. This is also motivated by the fact that, as revealed by validation exercises [87], TORPEX turbulence tends to have a different amplitude in the experiment compared to the two-dimensional simulations. The turbulent fluctuation amplitude is quantified by the parameter  $\xi = e\tilde{\phi}/\bar{T}_e$ , where  $T_e$  denotes the electron temperature at the ion injection site averaged over both time and vertical coordinate, and  $\tilde{\phi}$  is standard deviation of the electrostatic potential. The value of  $\xi$  is varied by redefining the electric potential

$$\phi(r, z, t) \rightarrow \bar{\phi}(r) + \xi/\xi_0(\phi(r, z, t) - \bar{\phi}(r)). \quad (5.5)$$

Here,  $r$  is the radial direction,  $z$  is the vertical direction and  $\bar{\phi}$  is the t- and z-averaged radial electric potential profile. Note that  $\xi$  decreases from the HFS to the LFS. In the investigation presented next, the value of  $\xi$  at  $R = R_0$ ,  $\xi_0 \approx 0.8$ , is taken as the reference value and  $\xi$  varies as a function of  $r$  ( $0.8 \lesssim \xi/\xi_0 \lesssim 1.2$ ).

The difference in the trajectories followed by different suprathermal ions has different sources of stochasticity. Firstly, the ions have slightly different initial parameters, which in a chaotic dynamical system such as the turbulence of TORPEX plasmas, can lead to very different trajectories. This effect could be characterized by a Lyapunov exponent which indicates the exponential rate at which the trajectories diverge [162]. Secondly, in the experiment, the source is continuously emitting. Ions emitted at different times sample different realizations of the turbulence which, comforted by the high reproducibility of TORPEX discharges, we suppose to be a stationary stochastic process. In order to take into account this effect in the simulations, the suprathermal ions are separated in a large number of bins and each bin is injected at different times in the GBS simulation such that there is no overlap between the realizations of the turbulence experienced by each bin as shown in Fig. 5.3. All the trajectories are then regrouped to compute the variance of the displacements.

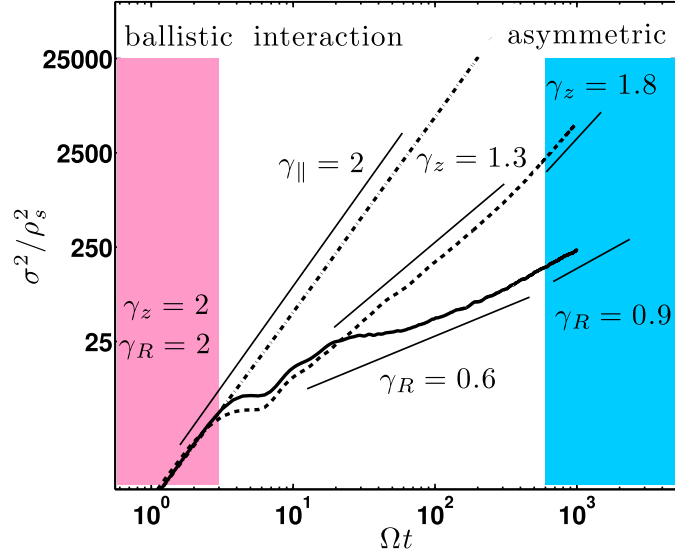


**Figure 5.4** | Variance of displacements of suprathermal ions in the radial (solid curve), vertical (dashed curve), and parallel (dashed-dotted curve) directions for  $\mathcal{E} = 50$  and  $\xi = 0.8$  from [67]. Dispersion exponents  $\gamma$  are fitted with solid line segments, which have error of  $\pm 0.1$ . An initial ballistic phase occurs (red-shaded region) with  $\gamma_R \approx \gamma_z \approx 2$ . This is followed by a fast transition to the turbulence interaction phase when  $\gamma_R$  remains nearly constant. Later, a slower transition to the asymmetric phase (blue-shaded region) shows an increased value of  $\gamma_R$ . For the parallel direction, since there are no forces,  $\gamma_{\parallel} \approx 2$  always. The z-directed spreading also shows three phases in which the superdiffusion is due to the vertical drift velocity.

### 5.2.1 Numerical investigation of the suprathermal ion transport

A comprehensive numerical study of the behavior of the suprathermal ions [47, 67] has shown that the dispersion of suprathermal ions in the radial direction is generally non-diffusive, with

$$\sigma_{\delta R}^2(t) \sim t^{\gamma_R}, \quad (5.6)$$

where  $0 < \gamma_R \leq 2$ . Here,  $\sigma_{\delta R}^2(t) = \langle (\delta R - \langle \delta R \rangle)^2 \rangle$  and  $\delta R(t) = R(t) - R(0)$ , where  $R$  is the ion radial positions. For this study, a point-like source is used with an isotropic injection cone with opening angle  $\sigma_\alpha = 0.1$  rad, directed parallel to the magnetic field lines. The Gaussian distribution of initial velocities is characterized by a mean,  $v_0$ , and a standard deviation  $\sigma_{v_0} = 0.1 v_0$ . A large number of tracers ( $10^4$  separated in 100 bins) is used.

This investigation revealed that the transport of suprathermal ions is characterized by three phases referred to as *the ballistic phase*, *the interaction phase* and *the asymmetric phase*. Figure 5.4 shows the evolution of the variance of displacements of the suprathermal ions in the radial, vertical and parallel directions for  $\mathcal{E} = 50$  and  $\xi = 0.8$  [67]. Initially, the dispersion of the suprathermal ions is ballistic, with  $\gamma_R = 2$ , analogous to the short ballistic transport phase in a typical collisional random walk predicted (see Eq. (4.44)) and observed in neutral fluids [163]. During this ballistic phase, which lasts approximately one gyroperiod, particles move relatively unperturbed with respect to the initial velocity, unaffected by the turbulent

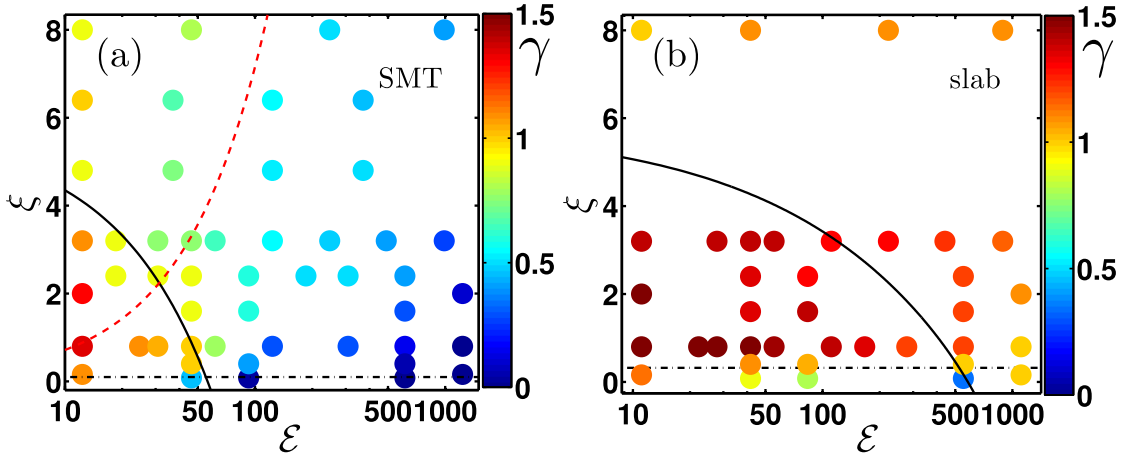


**Figure 5.5** | Dispersion exponents  $\gamma_R$  (colored dots) in the interaction phase are presented in the  $(\mathcal{E}, \xi)$  space for the SMT (a) and slab (b) (from [67]). Error on the value of  $\gamma_R$  is  $\pm 0.1$ . For  $\xi < 0.3$  (dashed-dotted horizontal lines), the turbulent fluctuations are too small for connected radial streamlines to form, therefore  $\gamma_R \rightarrow 0$  abruptly. Above the  $k_{\Delta}\rho = 2$  (solid black curves) gyroaveraging reduces  $\gamma_R$ . In the SMT case, drift-averaging is indicated by the dashed red curve. To the right of this curve, drift-averaging reduces  $\gamma_R$ .

electric field and the background magnetic field, and therefore have a uniform motion. Due to the prescribed spread in initial velocities, uniform motion leads to a spatial dispersion with  $\gamma_R \simeq 2$ .

The second phase begins when the interaction with the plasma becomes significant and is referred to as the interaction phase. The radial transport is due to the turbulent  $\nu_{\mathbf{E} \times \mathbf{B}}$  arising from the turbulence in the plasma potential  $\phi$ . A large number of suprathermal ion simulations have revealed that the transport during the interaction phase is set by two mechanisms that can reduce it: gyroaveraging and drift-averaging [47, 67]. The importance of these two effects was investigated as a function of the dimensionless quantities representing the suprathermal ion energy and the amplitude of the turbulent fluctuations:  $\mathcal{E}$  and  $\xi$ . It was seen that, depending on the values of these parameters, the value of  $\gamma_R$  can vary from superdiffusive ( $\gamma_R > 1$ ) to subdiffusive ( $\gamma_R < 1$ ). Figure 5.5 shows the value of  $\gamma_R$  in the interaction phase as a function of the two parameters  $\mathcal{E}$  and  $\xi$ , for the SMT case (a) and in the case of a plasma slab (b), corresponding to the limiting case of the SMT when  $R \rightarrow \infty$ . Studying the slab case allows highlighting the importance of the curvature and grad- $B$  drifts present in the SMT case and not in the slab case. We now review the main aspects of gyroaveraging and drift-averaging.

### Gyroaveraging

Gyroaveraging takes place when the suprathermal ion Larmor radii become comparable to the linear size of the turbulent structures and when the turbulence varies over a time scale that is large compared to the cyclotron frequency of the suprathermal ions. In this case, the effective electric potential that the suprathermal ion guiding centers experience

is averaged over their cyclotron motion and, considering a plane wave decomposition of the electrostatic potential  $\phi(\mathbf{r}, t) = \hat{\phi} \exp[i(\mathbf{k} \cdot \mathbf{r} - \omega t)]$ , reduces to a multiplication by a Bessel function [164]

$$\langle \phi(\mathbf{r}, t) \rangle_{\mathbf{R}} = \hat{\phi} e^{i(\mathbf{k} \cdot \mathbf{R} - \omega t)} \frac{1}{2\pi} \oint e^{(ik_{\perp} \rho \cos \theta)} d\theta = J_0(k_{\perp} \rho) \hat{\phi} e^{i(\mathbf{k} \cdot \mathbf{R} - \omega t)}. \quad (5.7)$$

Here,  $\mathbf{R}$  is the position of the guiding center,  $k_{\perp}$  is the perpendicular wave number of the turbulence,  $\rho$  is the suprathermal ion Larmor radius,  $\theta$  is the angle swept by the by the Larmor motion around the guiding center and  $J_0(x) = \frac{1}{2\pi} \int_0^{2\pi} \exp(ix \cos \theta) d\theta$  is the zeroth order Bessel function of the first kind. In the limit  $k_{\perp} \rho \rightarrow 0$ , gyroaveraging is ineffective and, if drift-averaging is also small, the suprathermal ions are transported by the turbulent structures and the transport is expected to be superdiffusive. Figure 5.6 shows an example of the trajectories of suprathermal ions experiencing a superdiffusive transport (in black) and a subdiffusive transport due to gyroaveraging (in red). It is found that the transition from superdiffusive to subdiffusive happens when  $k_{\Delta} \rho \simeq 2$ , which is indicated by the solid back lines in Fig. 5.5. However, this transition is not sharp and the condition  $k_{\Delta} \rho \simeq 2$  is rather arbitrary. We note that the Larmor radius depends on the perpendicular velocity of the ions,  $\rho = v_{\perp} / \Omega$ , and

$$v_{\perp} \simeq v_{0,\perp} + v_{\mathbf{E} \times \mathbf{B}} + v_{\nabla B}, \quad (5.8)$$

where  $v_{0,\perp} \simeq \sqrt{2E/m\lambda}$  is the initial perpendicular velocity ( $\lambda = v_{\perp} / v_{\parallel}$ ),  $v_{\mathbf{E} \times \mathbf{B}} \simeq k_{\Delta} \tilde{\phi} / B$  and  $v_{\nabla B} \simeq 2E / (qBR)$ . Using these expressions, the condition  $k_{\Delta} \rho = C$  can be written as a function of  $\xi$  and  $\mathcal{E}$

$$\xi \simeq \frac{1}{k_{\Delta}^2 \rho_s^2 \mu} \left( C - k_{\Delta} \rho_s \lambda \sqrt{2\mathcal{E}\mu} - 2 \frac{\rho_s^2 k_{\Delta}}{R} \mu \mathcal{E} \right), \quad (5.9)$$

which is used to draw the black line in Fig. 5.5. Here,  $\mu = m / m_i$ , where  $m$  is the suprathermal ion mass and  $m_i$  is the mass of the plasma ions, and  $\rho_s = c_s / \Omega_{ci}$ .

### Drift-averaging

Drift-averaging in the SMT configuration arises due to the vertical drift of the suprathermal ions and the vertical periodicity of the turbulence in the ideal interchange regime. Provided that the vertical motion of the ions is sufficiently fast, an effective drift-average of the electric field fluctuations reduces the radial dispersion, making it subdiffusive. Due to the vertical periodicity of the turbulence, when suprathermal ions have large vertical velocities, the  $\mathbf{E} \times \mathbf{B}$  drift results in radial displacements of the guiding centers that are followed by radial displacements in the opposite direction with the same amplitude, averaging the total radial displacements toward zero. This mechanism leads to an anti-correlated motion that is known to be a source for subdiffusion (see Section 4.2) when particles are trapped in eddies or, for example, in numerical simulations of tracers in sheared zonal flows in electrostatic ion-temperature-gradient turbulence [165].

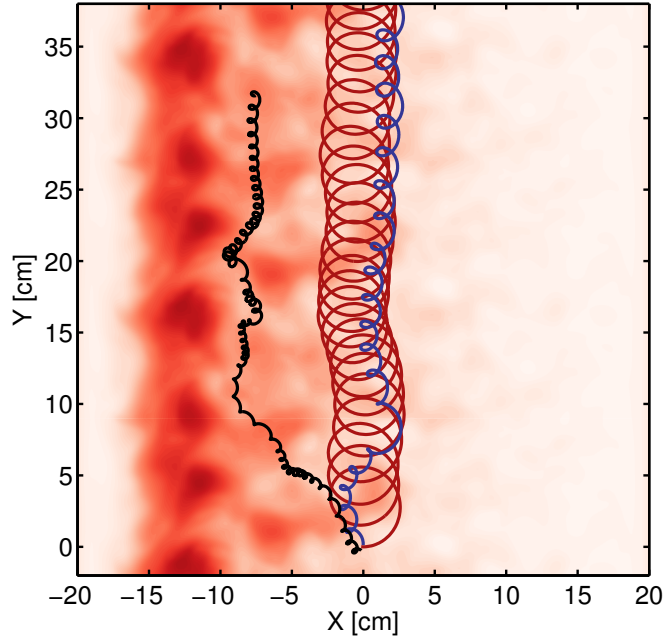


**Figure 5.6** | Example of simulated suprathermal ion trajectories superimposed on a snapshot of the turbulent electrostatic potential used in the simulations. The mechanism of gyroaveraging is represented by the red trajectory with a Larmor radius size comparable to the size of the turbulent structures. The blue trajectory represents an ion that is experiencing drift averaging due to its large vertical drift. The transport experienced by the red and blue ions is subdiffusive. The black trajectory represents an ion with a small Larmor radius and a small vertical drift whose trajectory is strongly affected by  $\mathbf{E} \times \mathbf{B}$  drifts, leading to a superdiffusive transport.

Figure 5.6 shows an example of the trajectory of a suprathermal ion experiencing a subdiffusive transport due to drift-averaging (in blue). The ratio of the time taken by an ion to move across a turbulence wavelength in the radial direction to the time it takes to vertically move across it quantifies the importance of drift-averaging [67]. The time required to move radially across the structure is

$$\tau_R \simeq \frac{L_R}{v_{\mathbf{E} \times \mathbf{B}, R}}, \quad (5.10)$$

where  $L_R$  is the radial scale of the vortex, which has been estimated for the ideal-interchange mode as  $L_R \simeq \sqrt{L_p/k_\Delta}$ , where  $L_p \simeq 5$  cm is the pressure gradient length scale [86]. Similarly, the time taken to move vertically across the structure is

$$\tau_z \simeq \frac{L_z}{v_{\nabla B} + v_{\mathbf{E} \times \mathbf{B}, Z}}, \quad (5.11)$$

with  $L_z \simeq 1/k_\Delta$ . The value  $\tau_R/\tau_z = 5$  corresponds approximately to the transition from superdiffusive to subdiffusive transport indicated by the dashed red line in Fig. 5.5.

The last phase of the transport takes place when the suprathermal ions start sampling regions

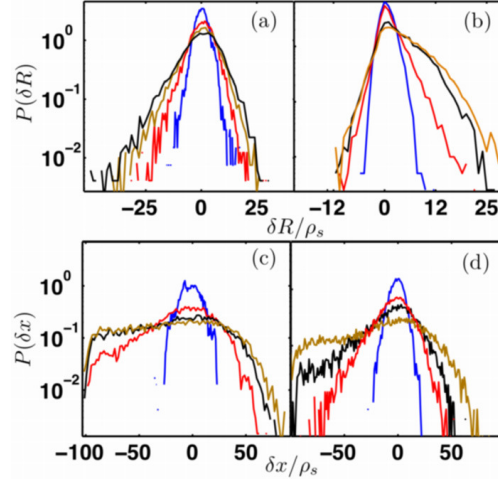


**Figure 5.7** | Probability density (PDF) of suprathermal ion displacements in the direction of the density gradient for the SMT: (a)  $\mathcal{E} = 50$  and (b)  $\mathcal{E} = 250$  injection, and slab: (c)  $\mathcal{E} = 50$  and (d)  $\mathcal{E} = 250$  injection (from [67]). The color of the PDF changes from blue-red-black-brown, in evenly spaced time increments for  $0 \leq \Omega t \leq 1000$ .

with different values of  $\xi$  and  $\mathcal{E}$ , both depending on the value of  $\bar{T}_e(r)$ . When the suprathermal ion beam becomes large compared to the scale over which the electron temperature varies (see Fig. 5.2(b)), the ions experience different transport regimes depending on the local values of  $\xi(r)$  and  $\mathcal{E}(r)$  (as described by Fig. 5.5) and the resulting total transport is close to diffusive ( $\gamma_R \simeq 1$ ). This is reflected in the asymmetry of the PDF of the particle position as a function of time shown in Fig. 5.7.

### 5.2.2 Lévy walk description of the suprathermal ion transport in TORPEX

The Lévy walk model presented in Section 4.2.1 has been applied to the numerical simulations of the suprathermal ion transport in TORPEX [145]. The exponents  $\mu$  and  $\nu$  of the jump PDF  $\psi(\Delta r, \Delta t) \propto \Delta r^{-\mu} \delta(\Delta t - \alpha \Delta r^{1/\nu})$  are computed from the PDF of the step sizes and the plot of the correlation between step sizes,  $\Delta r$ , and step durations,  $\Delta t$ , for a superdiffusive, a subdiffusive and a diffusive case of transport (Figs. 5.8). The values of the transport exponents corresponding to each case are then computed from the values of  $\mu$  and  $\nu$  and show a good agreement with the values computed from the temporal evolution of the variance. A Lévy walk generator is used to recreate the trajectories of the random walkers and to verify the accuracy of the procedure. This confirmed that the fundamental elements of the suprathermal ion transport process are contained in the two microscopic parameters of the Lévy walk,  $\mu$  and  $\nu$ .

However, the assumption of a symmetric distribution of step sizes does not capture the asymmetric nature of the suprathermal ion transport in TORPEX, which is due to the inhomogeneity of the background plasma profiles. Moreover, Figs. 5.8(c),(d) and (e) show that the coupling between the step sizes and the step durations is not well described by a power law,  $\Delta r = \nu \Delta t^\nu$ . For a given  $\Delta t$ , the range of step sizes spans to more than a order of magnitude. In this Thesis,

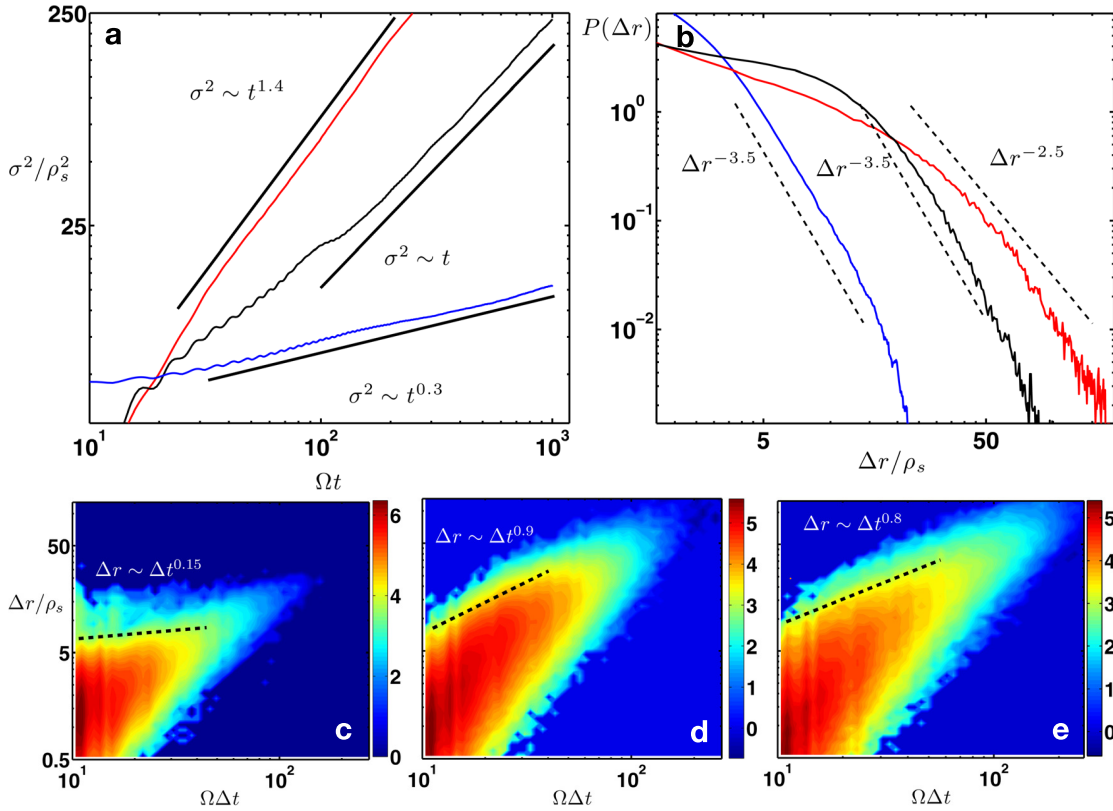


**Figure 5.8** | Lévy walk analysis of the suprathreshold ion numerical simulations on TORPEX [145]. **a**: Radial variance of the ion positions as a function of time for three different injection energies:  $E/T_e = 5$  (red) superdiffusive,  $E/T_e = 25$  (blue) diffusive and  $E/T_e = 250$  (black) subdiffusive. **b**: PDF of the step sizes for the three injection energies showing the values of the exponent  $\mu$ . **c,d,e**: Correlation between step sizes and step durations in log-log scale for  $E/T_e = 250$  (c),  $E/T_e = 25$  (d) and  $E/T_e = 250$  (e) with the best-fitting power law showing the values of  $\nu$ .

we have developed a new theoretical model that allows for an asymmetric transport and that does not assume a coupling of the step sizes and step durations, while allowing for temporal correlations (see Chapter 6).

### 5.2.3 Considerations for the comparison with experiment

For this Thesis, the numerical simulations previously developed were used to compare with experimental results. For this purpose, a realistic model of the injection parameters is crucial. The point-like model previously used is replaced by a more realistic model using a 2D Gaussian distribution for the initial positions. This mimics the finite size of the source aperture in TORPEX. In the experiment, the source is installed horizontally on the toroidal rail and therefore the injection cone forms a small angle with the helical magnetic field lines. Moreover, the orientation of the source relatively to the magnetic field lines can slightly change during the displacement of the source on the toroidal rail. The injection parallel to the magnetic field lines used previously in the simulations is replaced by an injection with a small angle (0.1 rad)

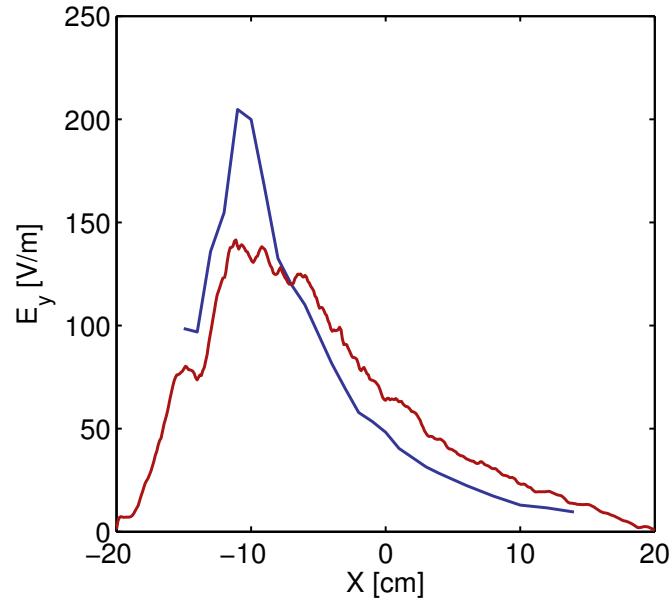


**Figure 5.9** | Radial profile of the fluctuations (standard deviation) of the vertical electrical field measured in TORPEX with the FRIPLE probe (blue) and from the GBS simulations (red).

to take this into account. The source parameters are also varied within the experimental uncertainties and the sensitivity of the results to these parameters is found to be small. The source parameters used to model the source in the simulations are reported in Chapter 7.

Using a non-point-like source with a non-parallel injection revealed the need of increasing the number of tracers in order to achieve a statistical convergence of the variance of particle displacements. This is of crucial importance since the time evolution of the latter is used to compute the value of the transport exponent  $\gamma_R$ . A convergence study has led to the choice of 4000 bins each containing 40 particles resulting in a total number of 160 000 particles. The relative error of the variance, averaged over its entire temporal evolution, compared to a case ran with 6000 bins containing each 100 particles, is smaller than 0.01%. The necessity of using more tracers in the simulations (16 times more than previously) considerably increased the running time of the simulations, which has motivated the parallelization of the code, performed in the context of a student project by Emil Rotilio.

The amplitude of the electrostatic fluctuations of GBS are adjusted to match the amplitude of the fluctuations in the experiment. Since the turbulent transport is caused by the  $\mathbf{E} \times \mathbf{B}$  drifts due to the fluctuating electric field, it is important to match the amplitude of the electric field. Furthermore, since we focus on the radial transport, we compared the vertical component of the electric field. Figure 5.9 shows the radial profile of the vertical electric field fluctuations measured with FRIPLE, at the midplane, and computed from the values of the floating potential from tips separated vertically by 1.6 cm [85]. The same quantity computed from the GBS simulation is also shown. At the injection position ( $X = 0$ ), the value of the vertical electric field in the experiment is  $E_{y,\text{TORPEX}} \approx 48 \text{ V/m}$  while the value in the

simulations is  $E_{y,\text{GBS}} \simeq 64 \text{ V/m}$ . The amplitude of the fluctuations is therefore multiplied by a factor  $\Xi = 0.75$  in the simulations as described in Section 5.2.

### 5.2.4 Fitting the transport exponent

When fitting the temporal evolution of the variance of displacements to compute the value of the transport exponent (Eq. (5.6)), one is confronted with the fact that the value of the variance is oscillating at the Larmor frequency of the suprathermal ions and therefore does not exactly follow a power law (Fig. 5.10(a)). Several options allow circumventing this issue. One can compute the variance from the trajectories of the guiding centers. However, the existence of the guiding centers relies on assuming the conservation of the magnetic moment,  $\mu$ , which is not always true for suprathermal ions in TORPEX [67]. Therefore this method implies a loss of generality. A smoothing of the variance as a function of time can be performed, but this does not rely on any physical ground.

Instead, we choose to fit the transport exponent using only the maxima of the variance, corresponding to the point of the ion gyromotion where they are the most separated. The reason for this choice is motivated in the following. Figure 5.10(a) shows the variance of displacements as a function of time for 70 eV ions injected in the magnetic field of TORPEX in the absence of electrostatic field. The maxima of the variance are indicated by red circles and the minima by red crosses. Figures 5.10(b) and (c) show the skewness and kurtosis of the distribution of displacements. The time index corresponding to the maxima and minima of the variance are also indicated by circles and crosses, respectively. We see that the maxima (circles) correspond to the points where the distribution of displacements is the least affected by orbit effects. Skewness and kurtosis measure the deviation of the distribution from perfect Gaussians. In particular, the skewness measures the asymmetry of the distribution (equal to zero for a Gaussian distribution), while the kurtosis measures the peakedness of the distribution (equal to 3 for a Gaussian). Figure 5.10 shows that a deviation from Gaussianity appears even in the absence of turbulence. The effect of the orbits could be misinterpreted as a turbulent interaction if we were to consider, for example, only the minima. Figure 5.10(b) also shows that, even by considering only the maxima, the skewness slightly increases over long times. This is due to the inhomogeneity of the magnetic field, upon which the Larmor frequency depends. At long times, the suprathermal ions desynchronize and the distribution of positions slightly deviate from a Gaussian. This is confirmed by simulations in a constant magnetic field, which do not display this effect. An investigation of this effect was carried out during a student Master's Thesis [166] and revealed that, for the ion energies under consideration here, it is negligible for injection angle  $\lesssim 0.17 \text{ rad}$ . This discussion points out the importance of taking into account higher moments of the distribution of displacements, or, if possible, the complete distribution (see Chapter 6).

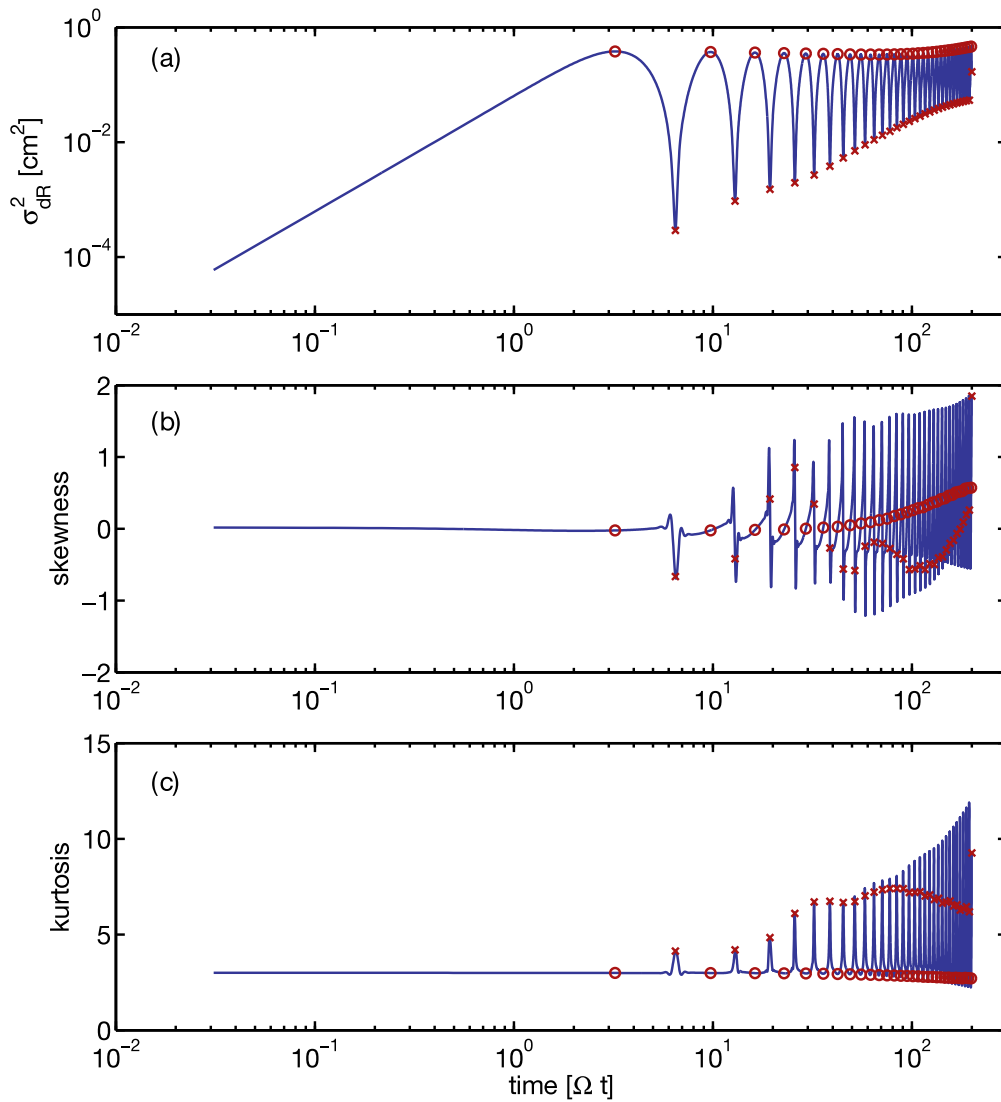


**Figure 5.10** | (a) variance of displacement as a function of time for 70 eV ions injected in the magnetic field of TORPEX in the absence of electrostatic field. The maximas of the variance are indicated by red circles and the minimas by red crosses. (b) and (c) shows the skewness and kurtosis of the ion displacements. The time index corresponding to the maximas and minimas of the variance are also indicated by circles and crosses, respectively.



# 6 Fractional Lévy motion analysis

This Chapter presents the application of the fractional Lévy motion (fLm) model to the numerical simulations of the suprathermal ions in TORPEX. We generalize the fLm model presented in Chapter 4 to allow for an asymmetric propagator. We show that asymmetric fLm can be described by a transport equation using space-fractional differential operator with non-zero skewness [167]. The time evolution of the radial particle position distribution is shown to be described by solutions of the fractional diffusion equation corresponding to asymmetric fLm in subdiffusive and superdiffusive cases.

## 6.1 Asymmetric fractional Lévy motion

Asymmetric fractional Lévy motion (afLm) is based on the fLm (see Section 4.2.2), with the difference that it does not restrict the Lévy noise to be symmetrically distributed (see Appendix A). Similarly to the fLm, which generalizes the Langevin description of Brownian motion [114], it is characterized by long-range positive or negative time correlation and Lévy distributed spatial increments.

The Langevin stochastic equation defining the afLm process is  $x(t)$  is [167]

$$x(t) = \frac{1}{\Gamma(H - 1/\alpha + 1)} \int_0^t (t - t')^{H-1/\alpha} \xi_{\alpha,\sigma}^\theta(t') dt', \quad (6.1)$$

where  $\xi_{\alpha,\sigma}^\theta(t)$  is an uncorrelated noise distributed according to a Lévy strictly stable distribution, with index of stability  $0 < \alpha \leq 2$ , scale parameter  $\sigma$  and asymmetry parameter  $\theta$ .  $\Gamma(\cdot)$  is the Gamma function. The definition and the main properties of the Lévy  $\alpha$ -stable distributions are recalled in Appendix A. When  $\theta = 0$ ,  $\xi_{\alpha,\sigma}^\theta(t)$  is symmetrically distributed and the afLm reduces to fLm.

From the definition and properties of strictly stable Lévy distributions (see Appendix A and [126]), it follows that, beside its asymmetry, afLm shares the same properties of fLm. We briefly recall them here.

## Chapter 6. Fractional Lévy motion analysis

AfLm is  $H$ -self-similar with stationary increments, meaning that the process is invariant under rescaling

$$x(\lambda t) = \lambda^H x(t) \text{ for all } \lambda > 0, \quad (6.2)$$

and exhibits a non-diffusive scaling of its moments

$$\langle |x(t)|^s \rangle \propto t^{sH}, \quad (6.3)$$

where  $0 < s < \alpha$ , to ensure convergence of the moments. The values of  $H$  are restricted to [126]

$$\begin{cases} 0 < H \leq 1/\alpha & \text{if } \alpha < 1, \\ 0 < H \leq 1 & \text{if } \alpha \geq 1. \end{cases} \quad (6.4)$$

Figure 4.5 summarizes the properties of the fLm and afLm as a function of the space transport exponent  $\alpha$  and time transport exponent  $\beta = \alpha H$ , and shows that they encompass the ordinary Brownian motion (oBm), the fractional Brownian motion (fBm) and the Lévy flight.

Following the derivation of Calvo *et al.* [156], and allowing for non-symmetric noise, we find that the propagator is given by a strictly stable distribution depending on  $x/t^H$

$$G_{\alpha,\beta}^\theta(x, t|x_0, 0) = \frac{C(\alpha, \beta)}{t^{\beta/\alpha}} L_{\alpha,\sigma}^\theta \left[ C(\alpha, \beta) \frac{x - x_0}{t^{\beta/\alpha}} \right]. \quad (6.5)$$

To find the diffusion equation associated with this propagator, we first take its Fourier transform in space

$$\hat{G}_{\alpha,\beta}^\theta(k, t) = \exp \left[ -\frac{\sigma^\alpha t^\beta}{\beta |\Gamma(\frac{\beta-1}{\alpha} + 1)|^\alpha} |k|^\alpha e^{i \text{sign}(k) \frac{\theta\pi}{2}} \right]. \quad (6.6)$$

Taking the time derivative of the previous expression,

$$\frac{\partial}{\partial t} \hat{G}_{\alpha,\beta}^\theta(k, t) = -\frac{\sigma^\alpha t^{\beta-1}}{|\Gamma(\frac{\beta-1}{\alpha} + 1)|^\alpha} |k|^\alpha e^{i \text{sign}(k) \frac{\theta\pi}{2}} \hat{G}_{\alpha,\beta}^\theta(k, t), \quad (6.7)$$

we recognize the Riesz-Feller space-fractional derivative of order  $\alpha$  and skewness  $\theta$ , defined as  $\mathcal{F}[D_\theta^\alpha f(x)] = -\psi_\alpha^\theta(k) \hat{f}(k)$ , where  $-\psi_\alpha^\theta(k) = -|k|^\alpha e^{i \text{sign}(k) \frac{\theta\pi}{2}}$  is the symbol of the pseudo-differential operator [129, 168]. The transport equation is found by Fourier inverting Eq. (6.7),

$$\frac{\partial}{\partial t} G_{\alpha,\beta}^\theta(x, t) = K_{\alpha,\beta} t^{\beta-1} D_\theta^\alpha G_{\alpha,\beta}^\theta(x, t), \quad (6.8)$$

where the effective diffusion coefficient  $K_{\alpha,\beta} = \sigma^\alpha / |\Gamma(\frac{\beta-1}{\alpha} + 1)|^\alpha$  has units  $\text{m}^\alpha / \text{s}^\beta$ . When  $\theta = 0$ , the equation is equivalent to Eq. (4.58) and for  $\beta = 1$  one finds the equation describing Lévy-Feller diffusion [168]. It is necessary to use an asymmetric propagator to capture

## 6.2. Numerical simulations of suprathermal ions transport in TORPEX

	$\delta_1$ [rad]	$\delta_2$ [rad]	$E$ [eV]	$X$ [cm]	$e\tilde{\phi}/T_e$
subdiffusive	$-0.10 \pm 0.08$	$-0.10 \pm 0.08$	$70 \pm 5\%$	$-0.4 \pm 0.12$	0.56
superdiffusive	$0.03 \pm 0.08$	$0.00 \pm 0.08$	$10 \pm 5\%$	$-0.4 \pm 0.12$	0.56

**Table 6.1** | Initial parameters of the simulated ions trajectories. The standard deviation of the Gaussian spreadings is also indicated.  $\delta_1$  is the angle between the source orientation and the horizontal plane and  $\delta_2$  is the angle between the source orientation and the toroidal direction. Injection energy  $E$ , injection position  $X$  ( $X = 0$  represents the center of the poloidal cross-section) and fluctuation amplitude,  $e\tilde{\phi}/T_e$ , at the injection position are also indicated

the asymmetry of the transport found in magnetically confined plasmas, including in basic toroidal plasma experiments, where the inhomogeneity of the magnetic field and of the fluctuations between high and low field sides can lead to an asymmetric dynamics [67].

Similarly to fIm, the restriction on the range of permissible values for  $H$  (Eq. (6.4)) translates for  $\beta$  as

$$\begin{cases} 0 < \beta \leq 1 & \text{if } \alpha < 1 \\ 0 < \beta \leq \alpha & \text{if } \alpha \geq 1, \end{cases} \quad (6.9)$$

and when  $\beta < 1$  or  $\beta > 1$  the process is negatively or positively time correlated,  $\beta = 1$  corresponding to an uncorrelated process.

## 6.2 Numerical simulations of suprathermal ions transport in TORPEX

To find the values of the spatial and temporal transport exponents,  $\alpha$  and  $\beta$ , describing the transport of suprathermal ions in TORPEX, we perform numerical simulations that model the suprathermal ion experimental setup installed in TORPEX as described in Section 5.2.1. Here, we are interested in the interaction phase. This phase can last several dozens of gyroperiods, until the ions sample regions with sufficiently different turbulence characteristics. The average resulting transport is close to diffusive ( $\gamma_R \simeq 1$ ). We focus on two cases, with different initial conditions (reported in Table 6.1): a superdiffusive case with an injection parallel to the magnetic field lines and an energy of 10 eV (corresponding to a ratio  $E/T_e \simeq 9$ ) and a subdiffusive one with an energy of 70 eV ( $E/T_e \simeq 64$ ) and a small angle between the injection direction and the magnetic field.

The variance of the ion radial position, computed as

$$\sigma_R^2(t) = \langle (\delta R(t) - \langle \delta R \rangle)^2 \rangle, \quad (6.10)$$

where  $\delta R(t) = R(t) - R(0)$ , is shown in Fig. 6.1 as a function of time. The choice of the time

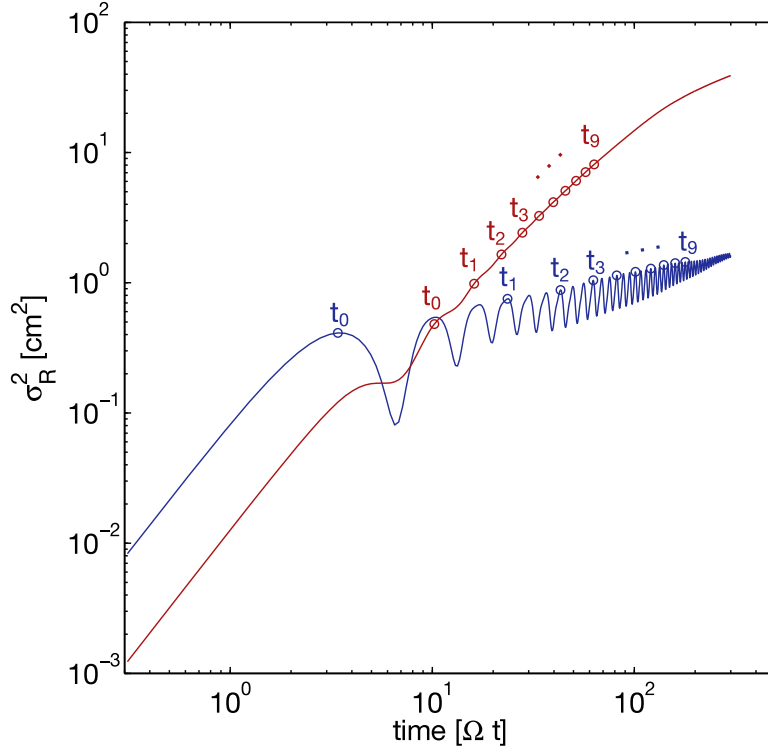


**Figure 6.1** | Variance of the suprathermal ion radial positions as a function of time. Ions with an energy of 70 eV (blue) experience a subdiffusive transport whereas ions with an energy of 10 eV (red) experience a superdiffusive transport. The circles represent the 10 selected time points for the fit. They are chosen at maxima of the gyromotion in the interaction phase. The time axis is normalized to the suprathermal ion gyroperiod  $1/\Omega$ .

points to compute the radial distribution has to be done carefully. Indeed, as can be seen in Fig. 6.1, the evolution of the variance is modulated by the gyromotion of the ions. As explained in Section 5.2.4, we choose time points corresponding to maxima of the gyromotion (shown in Fig. 6.1), where the trajectories are the least affected by orbit effects. The time intervals considered for the transport analysis cover the interaction phase and consist of 9 gyroperiods for the case of ions having an energy of 10 eV and 27 gyroperiods for ions of 70 eV.

The definition of the self-similarity exponent  $H$  (Eq. (6.2)) implies the following scaling of the variance of radial positions

$$\sigma_R^2(t) \propto t^{2H} \propto t^{\gamma_R}. \quad (6.11)$$

We note that, although the variance of stable distributions is infinite when  $\alpha < 2$ , the variance of our particle distribution is always finite due to the finite number of particles and the finite size of the spatial domain. Equation (6.11) provides the relation between the different transport exponents,  $\gamma_R = 2\beta/\alpha$ , thus providing an additional method to compute  $\gamma_R$ , from  $\alpha$  and  $\beta$ , different from that used in Section 5.2.4, which is based on the scaling of  $\sigma_R^2$  with time. However, care has to be taken in the evaluation of  $\gamma_R$  from the evolution of  $\sigma_R^2(t)$  if one wants

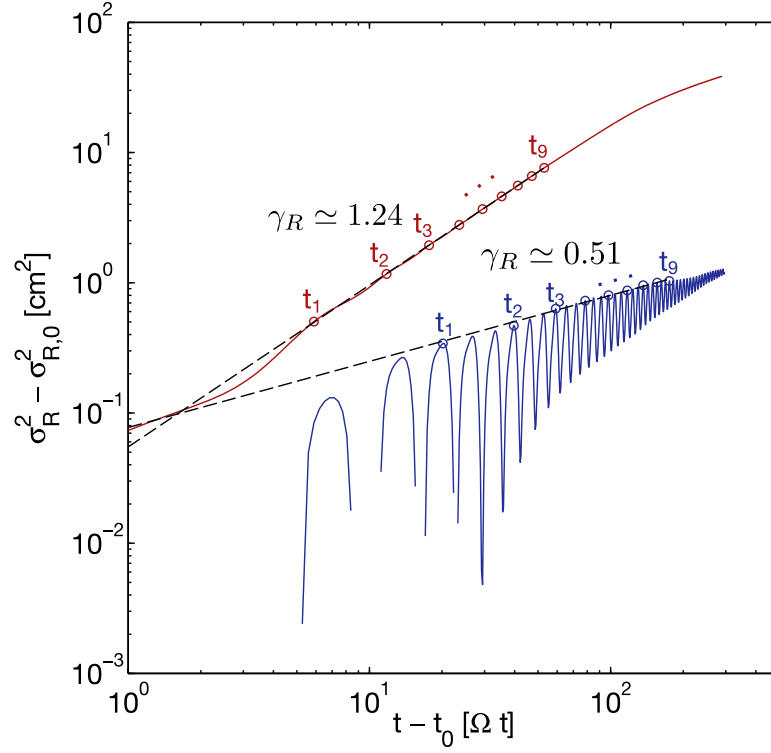


**Figure 6.2** | Same as Fig. 6.1 but with the axis shifted so that the beginning of the interaction phase corresponds to the origin of the plot. Fits of the slope (indicated in black dashed lines) provide the values of  $\gamma_R$  for the two cases.

to compare it with  $2\beta/\alpha$ . Since the value of  $\gamma_R$  changes between the ballistic phase and the interaction phase, new initial conditions have to be considered at the beginning of the latter. The definition of  $H$  in Eq. (6.2) implies that  $x(t=0) = 0$ , which is not true if we consider the initial condition at the end of the ballistic phase. In this case, the process satisfies

$$x(\lambda t) = \lambda^H x(t) + c, \quad (6.12)$$

for all  $\lambda > 0$ . Here  $c$  is a constant and the process belongs to the family of *broad-sense self-similar processes* ([169, definition 13.5] and [170, p. 272]).

The correct scaling of the variance with time is thus given by

$$\sigma_R^2(t) - \sigma_R^2(t_0) \propto (t - t_0)^{2H}, \quad (6.13)$$

with  $\gamma_R = 2H$ .

Indeed, if we assume  $\langle x^2(t) \rangle - \langle x^2(t_0) \rangle \propto (t - t_0)^K$ , using Eq. (6.12), we have

$$\begin{aligned}
 & \langle (\lambda^H x(t) + c)^2 \rangle - \langle (\lambda^H x(t_0) + c)^2 \rangle \propto \lambda^K (t - t_0)^K \\
 \Rightarrow & \langle \lambda^{2H} x^2(t) + 2c\lambda^H x(t) + c^2 \rangle - \langle \lambda^{2H} x^2(t_0) + 2c\lambda^H x(t_0) + c^2 \rangle \propto \lambda^K (t - t_0)^K \\
 \Rightarrow & \lambda^{2H} (\langle x^2(t) \rangle - \langle x^2(t_0) \rangle) + 2c\lambda^H (\langle x(t) \rangle - \langle x(t_0) \rangle) \propto \lambda^K (t - t_0)^K \\
 \Rightarrow & \lambda^{2H} (\langle x^2(t) \rangle - \langle x^2(t_0) \rangle) \propto \lambda^K (t - t_0)^K.
 \end{aligned} \tag{6.14}$$

The last relation implies  $K = 2H$  since it must be true for all  $\lambda > 0$  and  $\langle x(t) \rangle = \langle x(t_0) \rangle$ , as the process has a constant mean.

Figure 6.2 shows the time evolution of the variance of radial positions, with the axis correctly shifted so that the slope of the plot is equal to  $\gamma_R$ . A least-squares fit gives for the subdiffusive case,  $\gamma_R \approx 0.5$  and for the superdiffusive case  $\gamma_R \approx 1.24$ . The values found by shifting the time and the variance with the initial conditions are slightly different from those found without the shifts ( $\gamma_R \approx 0.3$  and  $1.5$ , for the sub- and superdiffusive case, respectively). The previous approach [47, 67] (without shifts) gives a global value of  $\gamma_R$  and the new one gives a local value in the interaction phase.

### 6.3 Least-squares fit of the radial distribution

In this section we describe the procedure and the results of the fit of the radial profiles with the evolution given by the propagator of the fLm. Histograms of the radial position PDF are computed at selected times,  $t_i, i = 0, \dots, 9$ , (indicated by circles in Figs. 6.1 and 6.2). The profiles are centered around  $r = 0$ , removing the mean drift velocity, thus focusing on the radial spreading of the profiles. The first profile is used as initial condition  $n_0(x, t = 0)$  and its convolution with the propagator (Eq. (6.5)) provides the profile at all times  $t_i$ ,

$$n(x, t_i) = G_{\alpha, \beta}^{\theta}(x, t_i | x_0, 0) * n_0(x). \tag{6.15}$$

The four parameters  $(\alpha, \beta, K, \theta)$  characterizing the transport are fitted, in the least-squares sense, such that the convolution of the propagator with the initial condition simultaneously best-fits the profiles at each times  $t_i, i = 1, \dots, 9$ .

Figures 6.3 and 6.4 show the resulting profiles for ions with an energy of 10 eV and 70 eV, respectively. The parameters corresponding to the best fit are displayed in Table 6.2.

#### 6.3.1 Superdiffusive case

The fit of the superdiffusive case is in very good agreement with the profiles of the simulations as well as the value of  $\gamma_R$  and the value of  $2\beta/\alpha$ . The value of  $\beta > 1$  indicates the presence of positive time correlations in the process, revealing the persistent motion of the ions. The value  $\alpha < 2$  indicates that the process is non-Gaussian and characterized by a heavy-

### 6.3. Least-squares fit of the radial distribution

	$\alpha$	$\beta$	$K [\text{cm}^\alpha/\text{s}^\beta]$	$\theta$
subdiffusive	$2.00 \pm 0.01$	$0.58 \pm 0.02$	$0.100 \pm 0.001$	-
superdiffusive	$1.81 \pm 0.02$	$1.13 \pm 0.01$	$0.300 \pm 0.003$	$-0.193 \pm 0.002$
		$2\beta/\alpha$	$\gamma_R$	
subdiffusive		$0.58 \pm 0.02$	$0.51 \pm 0.04$	
superdiffusive		$1.24 \pm 0.02$	$1.243 \pm 0.003$	

**Table 6.2** | Parameters of the propagator (Eq. (6.5)) and fractional diffusion equation (Eq. (6.8)) giving the best fit of the radial profiles.  $\alpha$  and  $\beta$  are the spatial and temporal transport exponents, respectively,  $K$  is the effective diffusion coefficient and  $\theta$  is the asymmetry parameter. The value of the transport exponent  $\gamma_R$  computed from the radial position variance evolution (Fig. 6.2) is reported along with the value of the transport exponent computed as  $2\beta/\alpha$  and show a very good agreement. 95% confidence intervals of the fits are reported.

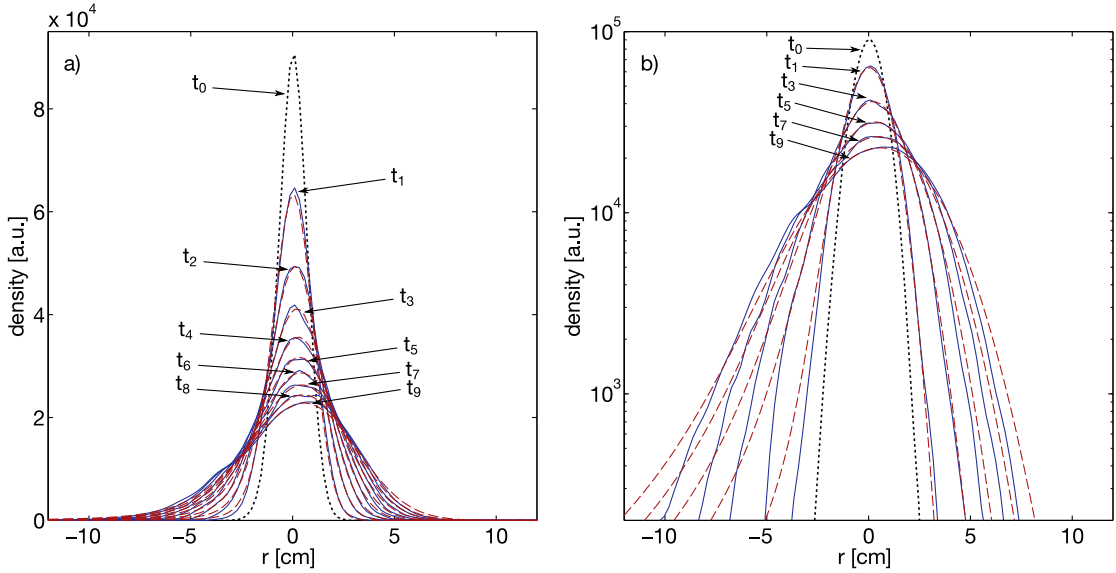


**Figure 6.3** | a) Radial profiles of the suprathreshold ion density for the superdiffusive case ( $E = 10$  eV). The initial condition is in black dotted line and the profiles at times  $t_i$ ,  $i = 1, \dots, 9$  are in blue. The best fit of the evolution given by the propagator of fLm is shown in dashed red lines, and show an excellent agreement. b) Same as a), but on logarithmic vs linear scale, for times  $t_i$ ,  $i = 1, 3, 5, 7, 9$ , showing that the fits have heavy-tails on their left side. The profiles follow the heavy-tails up to a certain radial extent. A cut-off is present due to the limitation of the radial velocity of the suprathreshold ions.

tailed propagator. The value of the skewness  $\theta$  reaches its maximum value ( $2 - \alpha$ ), meaning that the propagator is a stable distribution totally skewed to the left [126]. This reflects the asymmetry of the plasma fluctuations in TORPEX, where the turbulence is dominated by an ideal-interchange mode on the high field side and intermittent blobs propagating radially outward on the low field side [77, 97, 98, 100, 101]. Consequently, the profiles of the electron temperature and of the plasma potential fluctuations are strongly inhomogeneous. The values of  $E/T_e$  and  $e\tilde{\phi}/T_e$  change when the ions sample different regions of the plasma, leading

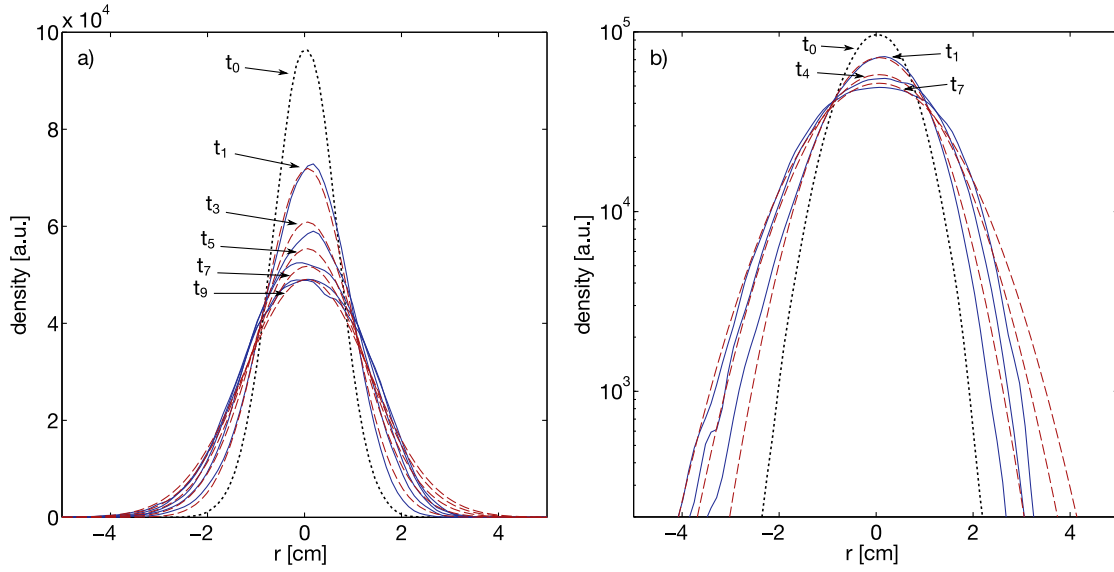


**Figure 6.4** | a) Radial profiles of the suprathermal ion density for the subdiffusive case ( $E = 70$  eV). The initial condition is in black dotted line and the profiles at times  $t_i, i = 1, 3, 5, 7, 9$  are in blue. The best fit of the evolution given by the propagator of fLm is shown in dashed red lines, and show a good agreement. b) Same as a), but on logarithmic vs linear scale, for times  $t_i, i = 1, 4, 7$ , showing the absence of heavy-tails for this subdiffusive case.

to an asymmetric transport (see Fig. 5.2). A cut-off of the heavy tails is visible in Fig. 6.3(b). Indeed, in the fLm model, space and time are decoupled (Section 4.2), allowing arbitrary fast radial steps of the suprathermal ions. On the other hand, in the simulations, the radial velocity, determined by the fluctuating  $\mathbf{E} \times \mathbf{B}$  drifts, is naturally limited, resulting in a cut-off of the propagator's tails similarly to the *Lévy-walk* model [128, 145, 171]. We note that the model of exponentially truncated Lévy processes [172, 173], which is described by a propagator having heavy-tails tempered by an exponentially decaying function could be used to refine the afLm [174]. The exponential truncation takes into account the non-ideal properties of the system (finite size, inhomogeneity). In the superdiffusive case, the truncation introduces a transition to a subdiffusive regime at long times, something that we have also observed experimentally (see Figs. 7.3 and 7.5). This model has also the advantage of possessing finite moments at all orders.

### 6.3.2 Subdiffusive case

For the subdiffusive case (Fig. 6.4), the fit reproduces the global evolution of the profiles. However, the agreement between the fits and the profiles is less good than for the superdiffusive case. In this case, we obtain  $\alpha = 2$ , indicating a Gaussian process, and  $\beta < 1$ , indicating a negatively correlated process. This is consistent with the picture of gyro- and drift-averaging causing an anti-persistent motion of the suprathermal ions leading to subdiffusion. As the propagator is Gaussian, it is forced to be symmetric. The asymmetry parameter  $\theta$  is irrelevant, although the profiles are slightly skewed. This causes a mismatch between the profiles and

the fits (Fig. 6.4) and represents a limitation of our model.

## 6.4 Conclusions

In this Chapter, we have derived the fractional diffusion equation and the propagator corresponding to asymmetric fractional Lévy motion [167]. This model embodies Lévy statistics of the displacements and time-correlations. Using numerical simulations, we showed that the temporal evolution of the radial position distribution of suprathermal ions in TORPEX can be well represented by solutions of the asymmetric fLm fractional diffusion equations in two cases: a superdiffusive case and a subdiffusive case matching experimental measurements [40]. This method provides the value of the spatial and temporal transport exponents ( $\alpha$  and  $\beta$ ), which are related to the transport exponent by  $\gamma_R = 2\beta/\alpha$ , and the asymmetry parameter  $\theta$ . The knowledge of these two exponents provides insights into the microscopic processes underlying the transport of suprathermal ions in TORPEX, previously not quantifiable. These findings complement and extend previous numerical studies of suprathermal ion transport in TORPEX [47, 67, 145], confirming that superdiffusion is caused by large intermittent and persistent  $\mathbf{E} \times \mathbf{B}$  drifts, while gyro- and drift-averaging effectively suppress these large drifts resulting in a Gaussian anti-persistent motion, which leads to subdiffusion.

The Lévy, heavy-tailed, statistics of the superdiffusive motion reflects the presence of large fluctuations in the particle motion characterizing intermittent bursts in the suprathermal ion transport. An investigation of the time-resolved measurements of the suprathermal ion transport in TORPEX and a characterisation of its intermittence is presented in Chapter 8. Intermittency of the transport can be a concern for burning plasmas because of its effects on the core reactivity, and, to a larger extent, on the heat load that suprathermal ions may produce on localized areas of the reactor first wall.



# 7 Comparison between experiment and simulations

The comparison between experimental time-averaged measurements of the suprathermal ion beam dynamics and numerical simulations is presented in this Chapter. To identify the transport regime, the radial transport exponent,  $\gamma_R$ , has to be computed from the temporal evolution of the variance of radial displacements of the suprathermal ions (Eq. (4.15)). However, the experimental data is time-averaged and the radial spreading of the ions is only accessible as a function of the toroidal distance. Owing to a small spreading in the initial injection parameters, the suprathermal ions all have a slightly different toroidal velocity and there is not a unique relation between their time of flight and their toroidal position. For this reason, numerical simulations are necessary to compute the transport exponent. In the following, we focus on two cases of transport of suprathermal ions in TORPEX, which are differentiated by their energy. In the first case, the suprathermal ions have an energy  $E \simeq 70$  eV and in the second they have an energy  $E \simeq 30$  eV. We compare the evolution of the radial width of the suprathermal ion beam with the results of numerical simulations to which a synthetic diagnostic is applied. The transport exponent is computed from the numerical simulations for the two cases. During the interaction phase, we find that the 30 eV ions experience a superdiffusive transport while the 70 eV experience a subdiffusive transport.

## 7.1 Experimental and numerical parameters

The experimental injection parameters in the experiment are reported in Table 7.1. The measurements have been performed over a period of more than two years using several suprathermal ion emitters. For this reason, the injection parameters slightly vary from one experimental campaign to the other. The values reported in Table 7.1 show the range spanned by the parameters during the different measurements. Plasma conditions in TORPEX are very reproducible. The plasma parameters characterizing the discharges used for this study are detailed in Section 2.1.3, Table 2.1, and Fig. 5.2.

Table 7.2 shows the initial parameters used for the injection of suprathermal ions in the simulated turbulent electric potential used for the comparison with the experiments. To take

## Chapter 7. Comparison between experiment and simulations

	$E$ [eV]	$X$ [cm]	$Y$ [cm]	$T_e$ [eV]	$e\tilde{V}_{pl}/T_e$
1	[68,74]				
2	[28,32]	[-2, -0.4]	[-15, 1.3]	[1.4 ± 0.4, 1.2 ± 0.3]	[0.58, 0.98]

**Table 7.1** | Injection parameters used in the experiments. We indicate the range over which the parameters have varied during the different experiments that we have conducted for this study.  $E$  is the ion initial energy,  $X$  is horizontal position of the source,  $Y$  its vertical position,  $T_e$  is the electron temperature at the injection position and  $e\tilde{V}_{pl}/T_e$  denotes the amplitude of the fluctuations. The vertical position of the source was changed for some experiments to maximize the distance traveled by the ions before they reach the upper wall (see Fig. 2.12).

	$E$ [eV]	$\delta_1$ [rad]	$\delta_2$ [rad]	$X$ [cm]	$Y$ [cm]	$\Xi$	$e\tilde{\phi}/T_e$
1	75 ± 5%	-0.10 ± 0.08	-0.10 ± 0.08	-0.4 ± 0.12	1.1 ± 0.12	0.75	0.58
2	65 ± 5%	-0.1 ± 0.1	-0.1 ± 0.1	-2 ± 0.12	1.1 ± 0.12	0.85	0.66
3	30 ± 5%	-0.10 ± 0.08	-0.10 ± 0.08	-2 ± 0.12	1.1 ± 0.12	0.75	0.57
4	25 ± 5%	-0.10 ± 0.08	-0.1 ± 0.08	-2 ± 0.12	1.1 ± 0.12	0.75	0.57

**Table 7.2** | Initial parameters of suprathermal ions in the simulations. The standard deviation of the Gaussian spreading is also indicated. Injection energy  $E$ , injection positions  $X$  and  $Y$  and fluctuation amplitude,  $e\tilde{\phi}/T_e$ , at the injection position are indicated.  $\Xi$  is the factor by which the plasma potential fluctuations are multiplied as explained in Section 5.2.3,  $\delta_1$  is the angle between the source orientation and the horizontal plane and  $\delta_2$  is the angle between the source orientation and the toroidal direction.

into account the experimental uncertainty of the initial values and their variation from one measurement to the other, two simulations are performed for each experimental case with initial parameters spanning the variation of the experimental initial parameters. Note that the initial vertical position is not important since the turbulence is periodic in the vertical direction. The turbulent electric potential is modeled with the GBS code and the details of the simulations are given in Section 5.1, Fig. 5.2, and Table C.1.

## 7.2 Synthetic diagnostic

Comparisons between the suprathermal ion current profiles measured in TORPEX and the simulations are made using a synthetic diagnostic. This produces the time-averaged poloidal suprathermal ion current profiles using the simulated tracer trajectories. To reconstruct the suprathermal ion current at a fixed toroidal position, the poloidal plane is tiled in squares of a size comparable to the experimental resolution of the measurements. To take into account the fact that, in the experiment, the resolution in the poloidal plane is varied as a function of the profile shapes (see Fig. 3.2), we use two different sizes of tiles in the synthetic diagnostic:  $4 \times 4 \text{ mm}^2$  and  $8 \times 8 \text{ mm}^2$ , representing the minimum and maximum resolutions typically used in the experiment. To compare the time-averaged ion current measured from the continuously

emitting source with the results of the simulations in which the tracers are all launched simultaneously, the current is integrated in each tile by letting all the tracers cross the poloidal plane. The profile is then interpolated using the exact same method used for the experimental profiles (Section 3.1). The mean vertical position and the radial variance are also computed in the same manner as for the experimental profiles (Section 3.2).

### 7.3 Comparison of the experiments with the synthetic diagnostic

Figures 7.1 and 7.2 show examples of poloidal time-averaged suprathermal ion current density profiles, in the presence of a plasma, measured at different toroidal locations for  $E = 30$  eV and  $E = 70$  eV from the experiments (left) and from numerical simulations (right). On top of the unperturbed motion, consisting of the gyromotion and the vertical drift (see Section 3.4), a broadening due to the interaction with the plasma turbulence is revealed. The broadening is larger for 30 eV than for 70 eV and is apparent in both the simulations and the experiments. Although the simulated profiles show some discrepancies with the measured ones, the main features, such as the overall shape, position and radial broadening, are correctly reproduced by the simulations.

The comparison between the measured and simulated evolution of the beam width as a function of the toroidal distance is shown in Figs. 7.3 and 7.4 for the two energies. The radial beam width is computed as the radial standard deviation of the suprathermal ion current profiles (see Section 3.2). The toroidal distance between the source and the detectors is computed with 1 cm precision. The statistical error arising from the averaging of the radial standard deviation over the entire profile is also taken into account in the error bars, as detailed in Section 3.3. The continuous bands are drawn from the synthetic diagnostic of numerical simulations. The bottom and top lines defining the bands are computed from the numerical simulations 1 and 2, from Table 7.2, for the 70 eV case and 3 and 4 for the 30 eV case. For the simulations 1 and 3,  $4 \times 4 \text{ mm}^2$  tiles are used in the synthetic diagnostic and  $8 \times 8 \text{ mm}^2$  tiles are used for the simulations 2 and 4.

The beam width oscillates due to the gyromotion of the ions. A slight discrepancy between measurements and simulations in the phase and amplitude of these oscillations is visible. This comes from the fact that they depend on the injection angle and energy, which can slightly vary from one measurement to the other. Close to the source, the profiles have comparable widths for the two energies (also shown in Figs. 7.1 and 7.2). As the distance from the source is increased, the radial width of the 30 eV ion beam is observed to grow much faster than that of the 70 eV ions. This indicates that the interaction with the plasma turbulence results in a larger spreading for ions with lower energy and that the transport that they experience is different. A good agreement between the experiments and the simulations is apparent.

The beam width evolution over the first 60 cm is shown in Figure 7.4. The oscillations of the beam width due to the gyromotion of the ions are visible both in the experiment and in the simulations. They are larger for 70 eV ions since their Larmor radii are larger than those of

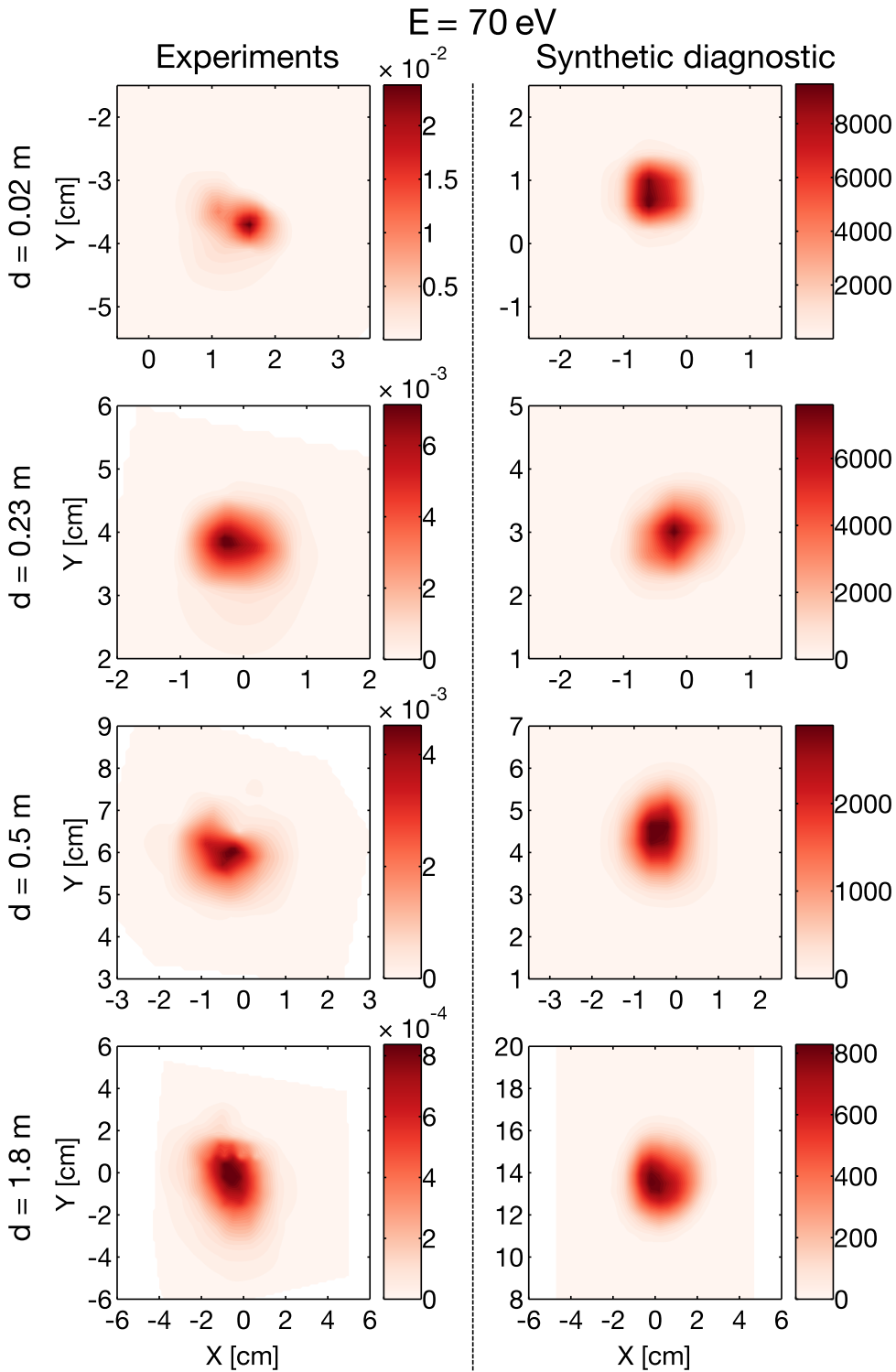


**Figure 7.1 | Poloidal suprathermal ion current density profiles at different toroidal distances** (from top to bottom,  $d = 0.02 \text{ m}$ ,  $0.23 \text{ m}$ ,  $0.5 \text{ m}$  and  $1.8 \text{ m}$ ) for ions having an energy of  $E = 70 \text{ eV}$ . Experimental measurements are displayed on the left in  $\text{A/m}^2$  and the results from numerical simulations (number 1 in Table 7.2) on the right (arbitrary units).

### 7.3. Comparison of the experiments with the synthetic diagnostic

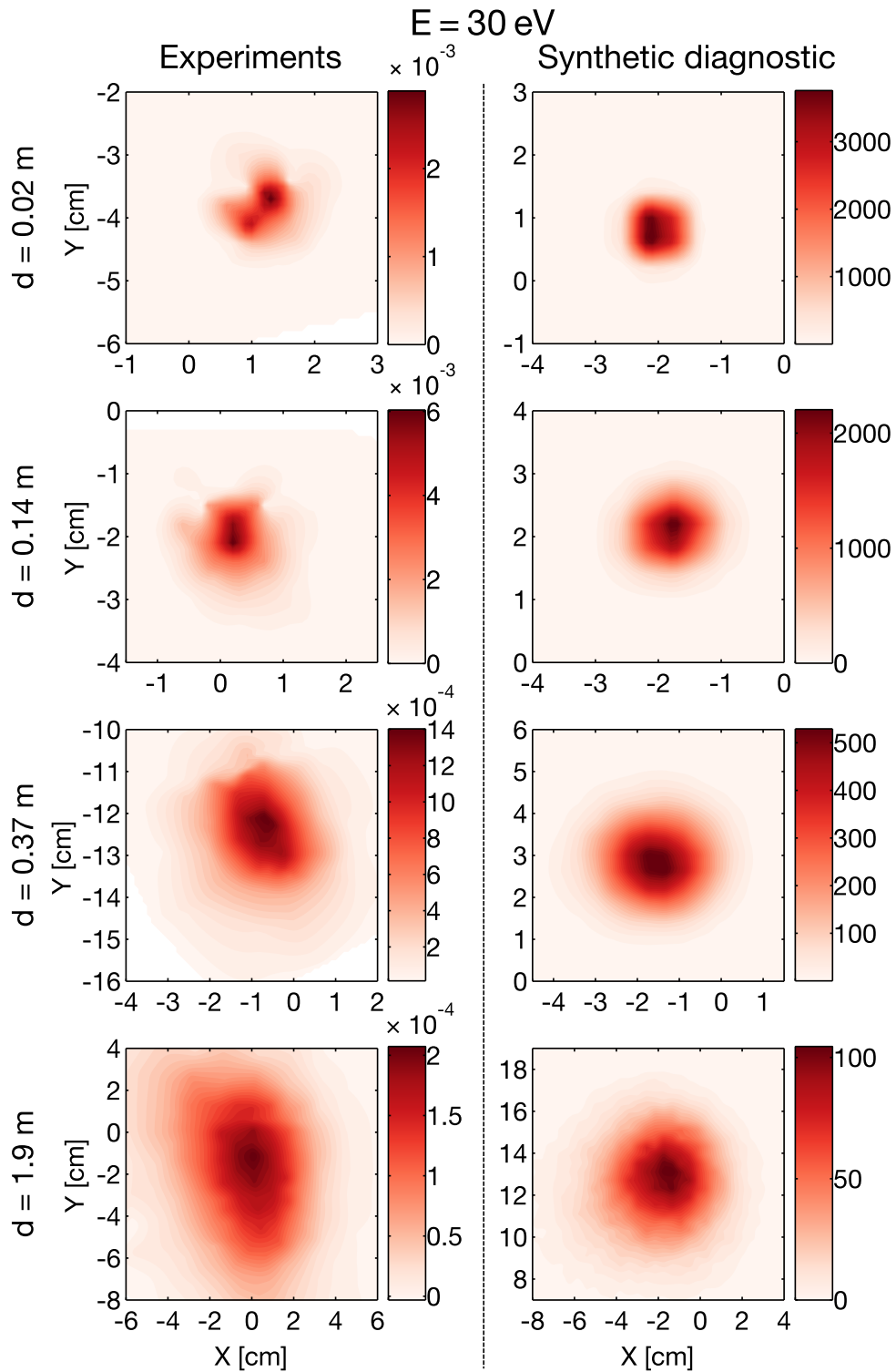


**Figure 7.2** | Poloidal suprathreshold ion current density profiles at different toroidal distances (from top to bottom,  $d = 0.02 \text{ m}$ ,  $0.14 \text{ m}$ ,  $0.37 \text{ m}$  and  $1.9 \text{ m}$ ) for ions having an energy of  $E = 30 \text{ eV}$ . Experimental measurements are displayed on the left in  $\text{A/m}^2$  and the results from numerical simulations (number 3 in Table 7.2) on the right (arbitrary units).

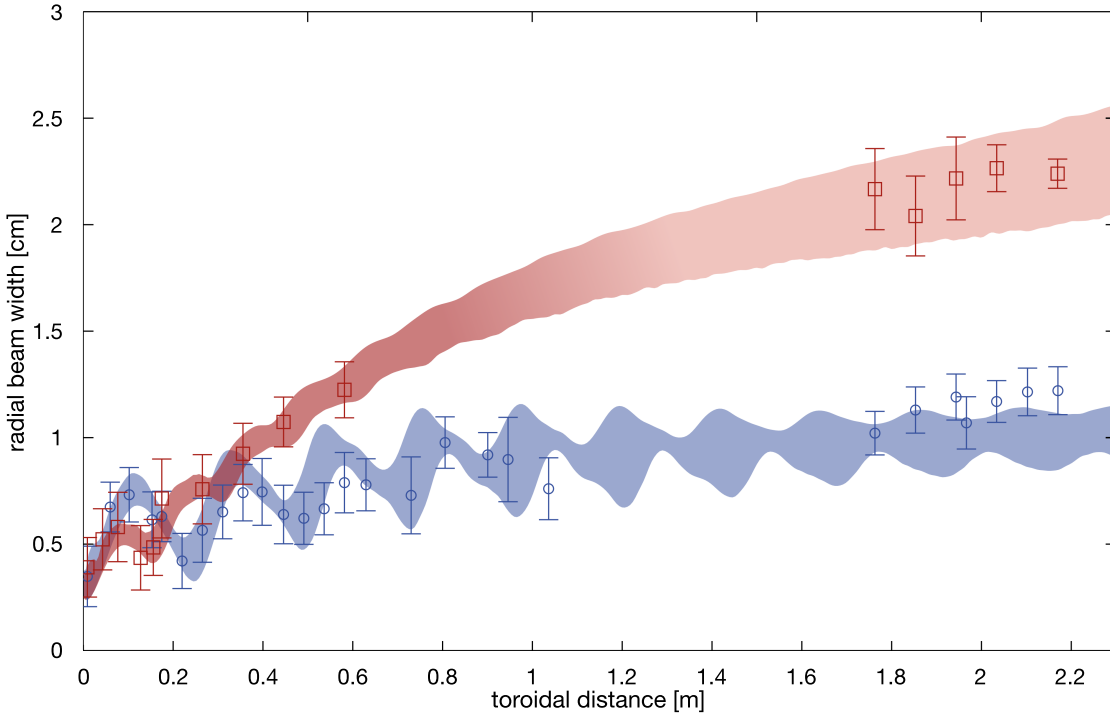


**Figure 7.3 | Radial width of suprathermal ion current profiles as a function of toroidal distance traveled.** Red squares and blue circles represent experimental measurements for ions emitted at 30 eV and 70 eV respectively. Continuous bands are drawn from a synthetic diagnostic of numerical simulations for 30 eV (red) and 70 eV (blue) ions. The width of the bands is obtained by varying the simulations input parameters within experimental uncertainties. On top of this oscillation, the beam spreads due to the interaction of the ions with the turbulence. The different trends of the spreading indicate different transport regimes. The ballistic phase, lasting approximately one gyroperiod (first three measurements), is in good agreement with the simulations for both energies (see Fig. 7.4). Then, the 30 eV ion beam spreads strongly until a toroidal distance of  $\approx 1$  m. The accumulated spreading of the 70 eV ion beam is less than the 30 eV beam. Error bars are computed by modeling the measurement with a finite size detector inlet (4 mm radius) and 2 mm absolute positioning accuracy (see Section 3.3).

30 eV ions. The first three measurements are made in the ballistic phase of the transport (see Section 5.2.1) and show good agreement with the numerical simulations.

## 7.4 Identification of the transport regimes

To compute the radial transport exponent,  $\gamma_R$ , the evolution of the variance of the ion radial displacements as a function of time,  $\sigma_R^2(t)$ , is computed from the numerical simulations reproducing the experimental conditions (Fig. 7.5). The ion transport is ballistic ( $\sigma_R^2(t) \propto t^2$ ) during a first phase lasting approximately one gyroperiod. In this short initial phase, the ions have not yet interacted with the plasma and are not yet magnetized [47, 163]. The ions enter a second spreading phase as they start to interact with the plasma turbulence. In this phase, different transport regimes are observed depending on the energy of the ions and the character

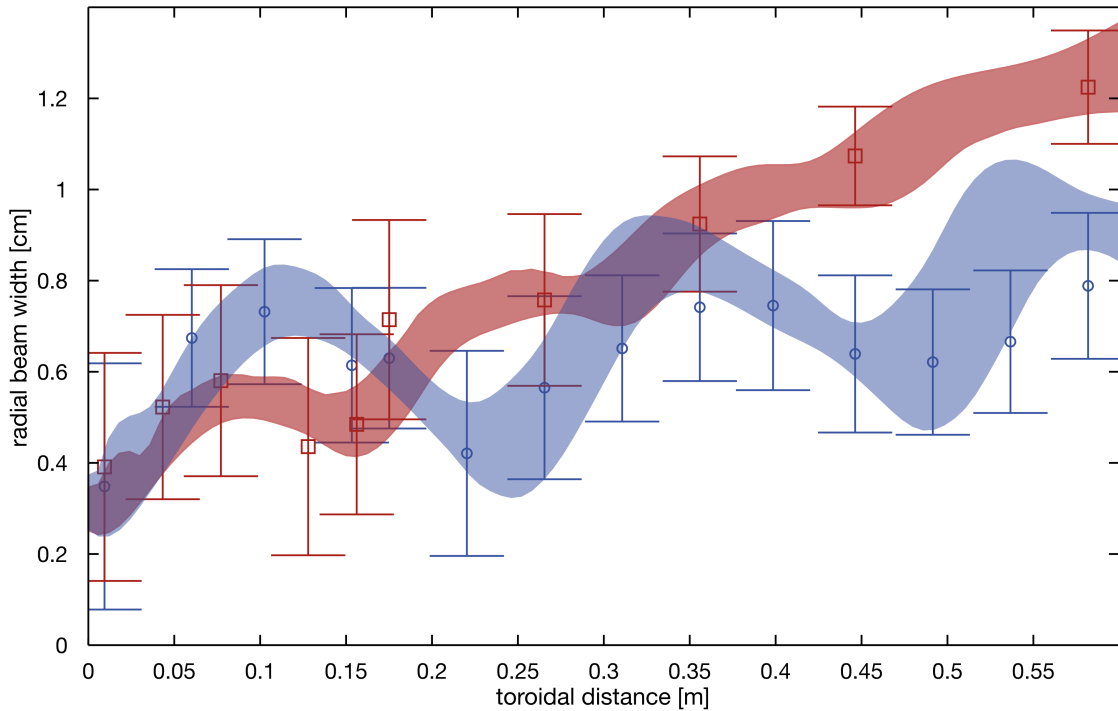


**Figure 7.4** | Same than Fig. 7.3 but showing only the first 60 cm of the toroidal distance traveled by the ions. The first three measurements are made in the ballistic phase of the transport and show good agreement with the numerical simulations.

of the turbulence (see Section 5.2.1). Fitting the temporal evolution of  $\sigma_R^2$  (Fig. 7.5) to power laws provides the values of the transport exponents in the different phases. To compute the transport exponents in Fig. 7.5, local maxima of  $\sigma_R^2(t)$  during the gyromotion are fitted with the equation  $\sigma_R^2(t) - \sigma_R^2(t_0) \propto (t - t_0)^{\gamma_R}$ , where  $t_0$  is chosen as the first maximum of each phase (see Section 6.2). Maxima are chosen since they correspond to the points of the gyromotion that are least affected by orbits effects (see Section 5.2.4). This procedure is applied to each simulation in Table 7.2 used to draw the bands in Fig. 7.3, and the average is computed for each phase.

In the interaction phase, an exponent  $\gamma_R = 0.51 \pm 0.01$  is found for ions of 70 eV ( $E/T_e \simeq 54$ ) and  $\gamma_R = 1.20 \pm 0.04$  for ions of 30 eV ( $E/T_e \simeq 23$ ), indicating that the transport varies from subdiffusive to superdiffusive as the energy of the ions is decreased. These results show, for the first time, the existence of two different transport regimes, in the same background turbulence, for suprathermal ions in TORPEX that are only differentiated by their energy. For ions of 30 eV, after the superdiffusive phase, a phase where the transport is close to diffusive ( $\gamma_R = 0.92 \pm 0.04$ ) is visible in Fig. 7.3 after approximately 1 m and in Fig. 7.5 after six gyroperiods. This phase appears when the size of the beam becomes sufficiently large that ions sample regions of the plasma with different fluctuation amplitudes, originating an average transport close to diffusive (see Section 5.2.1).

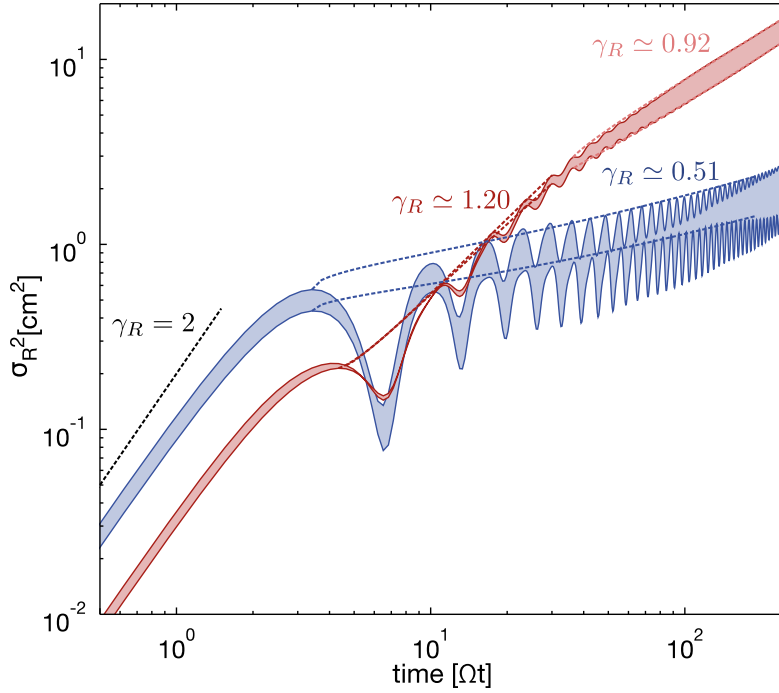


**Figure 7.5 | Variance of the ion radial positions as a function of time.** Results obtained from the numerical simulations reproducing the experimental data in Fig. 7.3, for ions at 70 eV (blue) (number 1 and 2 in Table 7.2) and 30 eV (red) (number 3 and 4 in Table 7.2). Fits of the different phases, shown in dashed lines, provide the values of the transport exponent  $\gamma_R$ . A slope corresponding to  $\gamma_R = 2$  is shown next to the initial ballistic phase. For ions of 30 eV, the transport is then superdiffusive with a transport exponent  $\gamma_R \simeq 1.20$  during approximately 4 gyromotions and finally close to a diffusive process with  $\gamma_R \simeq 0.92$ . For ions of 70 eV, the transport is subdiffusive with  $\gamma_R \simeq 0.51$ . Time is normalized to the ions gyroperiod.

Applying the asymmetric fractional Lévy motion (afLm) analysis (Chapter 6) to the simulations used here, we find that, in the interaction phase, for 30 eV the transport is non-Gaussian ( $\alpha = 1.88 \pm 0.04$ ), persistent ( $\beta = 1.18 \pm 0.02$ ) and asymmetric ( $\theta = 0.1 \pm 0.2$ ). For 70 eV ions, the transport is almost Gaussian ( $\alpha = 1.97 \pm 0.03$ ) and anti-persistent ( $\beta = 0.55 \pm 0.4$ ). The values of the transport exponent computed from  $\alpha$  and  $\beta$  are very close to the values computed from the fits of the variance: for the 30 eV case,  $2\beta/\alpha = 1.26 \pm 0.03$ , and for the 70 eV case,  $2\beta/\alpha = 0.56 \pm 0.05$ .

## 7.5 Discussion

We have shown that experimental measurements of suprathermal ion transport in a turbulent magnetized plasma are in agreement with validated numerical simulations for two ion energies. Therefore, the transport of these ions is demonstrated to be consistent with the non-diffusive transport theory that successfully describes the simulations (Section 5.2.1). The measured and simulated transport is first ballistic for approximately one gyroperiod, after

$E$ [eV]	$\gamma_R$	$\rho_L$ [cm]	$2\rho_L/L_z$	$v_z/v_R$	$\tau_R/\tau_Z$
70	$0.51 \pm 0.01$	$0.8 \pm 0.2$	0.6	$5.5 \pm 0.8$	7
30	$1.21 \pm 0.04$	$0.5 \pm 0.1$	0.3	$1.5 \pm 0.5$	2

**Table 7.3** | Energy, radial transport exponent in the interaction phase, Larmor radii, ratio of the vertical to the radial velocity, ratio of the Larmor orbit diameter to the vertical extend of the blobs and ratio of the time required to cross a blob radially to the time required to cross it vertically. All the values are computed from the simulations as the average over all particles and over time. The average from simulations 1 and 2 in Table 7.2 is computed for the 70 eV case and the average from simulations 3 and 4 is computed for the 30 eV case. The uncertainties are given by the standard deviation of value distribution for all particles. The Larmor radius is computed from the perpendicular velocity. The vertical velocity is given by the average of the guiding center vertical velocities. The radial velocity is given by the standard deviation of the guiding center radial velocities, since the averaged radial velocity is almost equal to zero.

which the spreading of the beam strongly depends on the injection energy. Numerical simulations allow determining the radial transport exponents  $\gamma_R$  and reveal the basic physical mechanisms leading to super- or subdiffusive behavior. Suprathermal ions with the lower energy follow Lévy-type (non-Gaussian) superdiffusive transport trajectories as they are transported by the turbulent structures. In the same turbulent plasma, suprathermal ions with larger energies average the turbulent electric field more significantly as larger Larmor radii and faster vertical drift lead together to anti-correlated, non-Markovian, subdiffusive transport. This work thus gives a proof of principle that the transport of suprathermal ions in turbulent plasmas can exhibit various non-diffusive regimes.

The relative importance of gyroaveraging and drift-averaging is estimated from the numerical simulations. Table 7.3 shows the Larmor radii, the ratio of the vertical to the radial velocity of the ions and the parameters indicating the importance of gyroaveraging,  $2\rho_L/L_z$ , and drift-averaging,  $\tau_R/\tau_Z = L_R v_z / (L_z v_R)$  (Section 5.2.1). The radial extent of the blobs is taken as the radial width of the interchange mode [86]  $L_R \simeq \sqrt{L_p/k_\Delta} \simeq 3.8$  cm and their vertical extent as [67]  $L_z \simeq 1/k_\Delta \simeq 2.9$  cm. The conditions identified in the numerical investigation (Section 5.2.1) [47, 67], for the gyroaveraging and drift-averaging to become effective are

$$2\rho_L/L_z = 2k_\Delta\rho_L \gtrsim 4 \quad \text{and} \quad \tau_R/\tau_Z \gtrsim 5. \quad (7.1)$$

In Table 7.3, the values of both ratios is higher for the 70 eV case than for 30 eV case indicating the role of these mechanisms in the reduction of the transport. The drift-averaging condition (Eq. (7.1)) is satisfied for the 70 eV case. On the other hand, the gyroaveraging condition (Eq. (7.1)) is satisfied in neither case. While the estimate of the vertical size of blobs given by  $L_z$  is in agreement with the value observed in the experiment using conditional sampling [95], it does not take into account the complex structures that constitute a blob. Seeded blob simulations show that, depending on their size, blobs are subject to secondary instabilities [175, 176], such as Kelvin-Helmholtz or Rayleigh-Taylor instabilities, that develop in complex

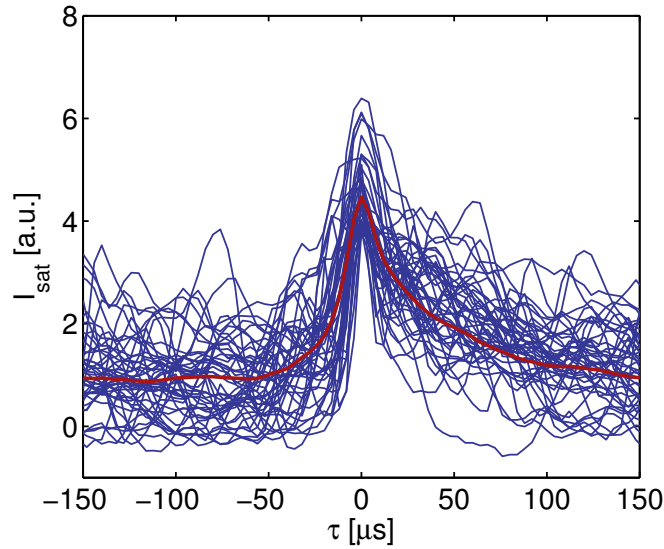


**Figure 7.6** | Ion saturation current time traces of blobs detected on a tip of HEXTIP with the technique of conditional average sampling (see Chapter 8). The traces in blue are the results of single blobs crossing the tip and the trace in red is the result of the conditional average sampling method. The blobs fine structures are visible on the individual  $I_{\text{sat}}$  time traces but they are averaged out by the conditional average sampling technique.

shapes with smaller scales than the blob size. These fine structures are not resolved by the experimental conditionally averaged measurements. For example, Fig. 7.6 shows the  $I_{\text{sat}}$  time traces of blobs detected on a tip of HEXTIP with the technique of conditional average sampling (see Chapter 8). The traces in blue are the results of single blobs crossing the tip and the trace in red is the result of the conditional average sampling method. The blobs fine structures are visible on the individual  $I_{\text{sat}}$  time traces but they are averaged out by the conditional average sampling technique. Moreover, different blob sizes are present in TORPEX [100], and the smallest ones are probably not detected, due to the insufficient resolution of the measurements. As the ion Larmor radii increase, the suprathermal ions gradually gyroaverage fine structures and small blobs. Nevertheless, a thorough investigation of the blob size and structure in TORPEX is still needed to fully characterize the effect of gyroaveraging.

## 8 Time-resolved measurements

In fusion experiments and astrophysical plasmas, measurements are limited to a few positions by high-temperature and diagnostics accessibility. In these cases, it is not possible to characterize the transport by the temporal evolution of the variance of displacements and information about the transport has to be inferred from the time trace statistics [83, 138, 177]. In this Chapter, we present first time-resolved measurements of the cross-field transport of suprathermal ions in a turbulent magnetized plasma [41].

In Chapter 7, by using three-dimensional time-averaged measurements of the width of a suprathermal ion beam in combination with numerical simulations (an example is shown in Fig. 8.1), we have shown that the transport of suprathermal ions varies from superdiffusive to subdiffusive as their energy is increased [37, 40, 47, 67, 69, 145, 167]. Here, we consider the same two cases than in Chapter 7, with suprathermal ion energies of 30 eV and 70 eV, for which the transport was identified to be superdiffusive and subdiffusive, respectively [40, 69]. We show that the time traces of the suprathermal ion current show a clear difference in the intermittency level. Using the technique of conditional average sampling (CAS) [70, 71], we identify the effect of turbulent structures on the suprathermal ion beam confirming the efficiency of gyroaveraging, depending on the ion energy, to decrease transport.

### 8.1 Experimental set-up for the time-resolved measurements

Figure 8.1 shows the setup used for this study. Similarly to the time-averaged measurements (Chapter 7), the suprathermal ion source is positioned in the region dominated by blobs, at  $X = 1.5$  cm and  $Y = -4.3$  cm, and injects suprathermal ions in the toroidal direction. At the injection position the time-averaged electron temperature measured by a triple probe [85] is  $T_e \approx 1.3$  eV. Measurements at different poloidal locations are taken using a gridded energy analyzer (GEA) [40] placed at a distance  $d = 41.2$  cm along the toroidal axis. At this distance, suprathermal ions have completed approximately two gyro-orbits and are in the interaction phase (Section 7.3) [47, 69]. The GEA is used to selectively measure the current produced by ions having an energy larger than 10 eV, repelling electrons (Section 2.2.2). The array of

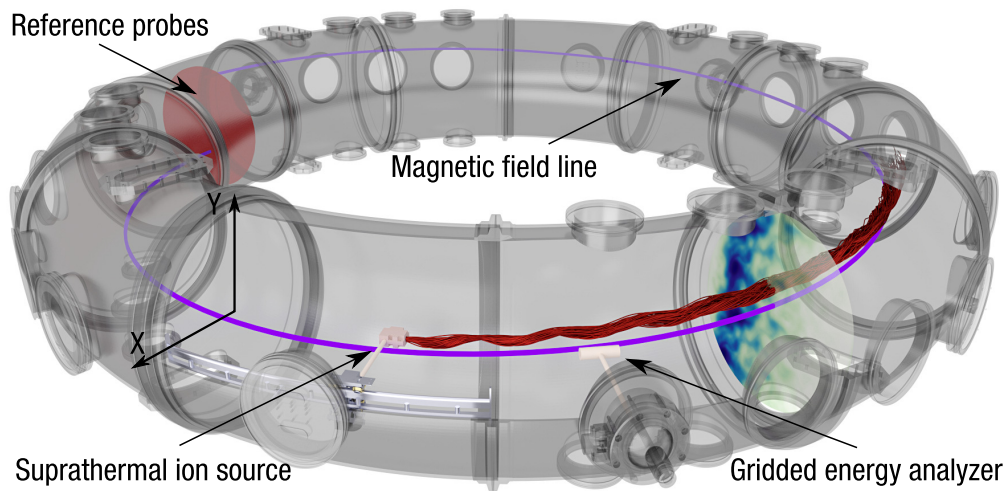


**Figure 8.1** | Experimental setup showing the TORPEX device. The suprathermal ion source and the gridded energy analyzer are shown. The poloidal plane in red indicates the position of the reference probes used for the CAS. A helical magnetic field line is shown in violet. The field lines crossing the suprathermal ion beam between the source and the detector cross the reference probe plane twice. Examples of computed suprathermal ion trajectories are shown in red along with a snapshot of the electric potential fluctuations as simulated by the GBS code [69, 87].

LPs, HEXTIP, shown in red in Fig. 8.1, is used to detect blobs for the CAS technique. In these experiments, synchronous detection is not used and the time traces of the GEA are directly digitized at 250 kHz during discharges lasting  $\approx 1.5$  s. This allows measuring the time-resolved suprathermal ion current but, as a complete poloidal profile of the  $I_{\text{sat}}$  fluctuations is recorded with HEXTIP for each measurements, a longer time is required to measure a complete poloidal profile than with the synchronous detection technique due to the time required by data acquisition.

## 8.2 Suprathermal ion current times traces

Figure 8.2 shows two examples of suprathermal ion current time traces from the GEA for ion energies of 30 eV and 70 eV. The bias voltage on the emitter is turned on and off at  $\sim 30$  Hz, allowing to differentiate the fluctuations of the background noise from those of the suprathermal ion current. During the on phase, the time trace for 30 eV ions shows a higher intermittency (Fig. 8.2(a)) than the 70 eV case (Fig. 8.2(b)). This difference is reflected in the PDFs for the current fluctuations of the two cases (Fig. 8.2 insets). The PDF for the 30 eV case is positively skewed suggesting the fact that the suprathermal ions reach the detector in bursts, while the PDF for the 70 eV ions does not show large fluctuations.

### 8.3. Time-averaged, skewness and kurtosis profiles of the suprathermal ion current

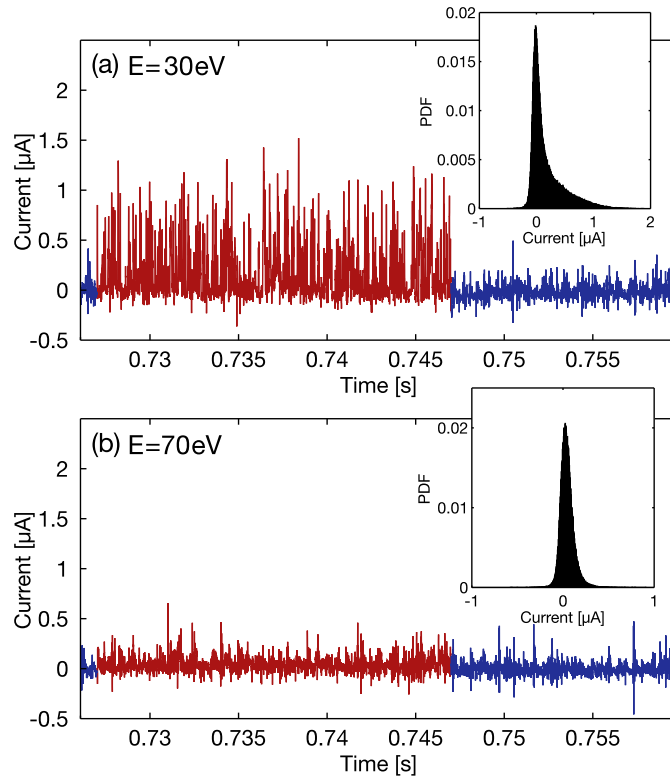


**Figure 8.2** | Suprathermal ion current time traces measured with the GEA positioned at the locations indicated by the black crosses in Fig. 8.3. The suprathermal ion source is turned on (red) and off (blue) periodically. The time trace of 30 eV ions (a) shows a high intermittency level contrary to the 70 eV ions time trace (b). Insets show the PDFs of the suprathermal current fluctuations. The PDF for the 30 eV case is strongly positively skewed, reflecting the intermittency of the signal, whereas the PDF for the 70 eV case is not.

### 8.3 Time-averaged, skewness and kurtosis profiles of the suprathermal ion current

We characterize the intermittency of the time traces by computing the skewness and kurtosis (also called flatness) [82, 178] of their PDFs. The skewness is the normalized third order moment of the PDF and is a measure of the asymmetry of the PDF. In our case, a positive skewness indicates the presence of positive bursts in the signal. The kurtosis is the normalized fourth order moment of the PDF and is a measure of the heaviness of the PDF tails. The periods during which the source is not emitting are used to compute the position-dependent background values of the mean (offset), skewness and kurtosis. These are removed from the values computed during the on phases.

Figures 8.3(a) and (b) display two-dimensional profiles of the time-averaged suprathermal ions current density for the two energies. Although the time-averaged profiles for the two energies are relatively similar, when the profiles of the skewness and kurtosis of the time-traces are reconstructed (Figs. 8.3(c),(d),(e) and (f)), a clear difference appears. While the skewness

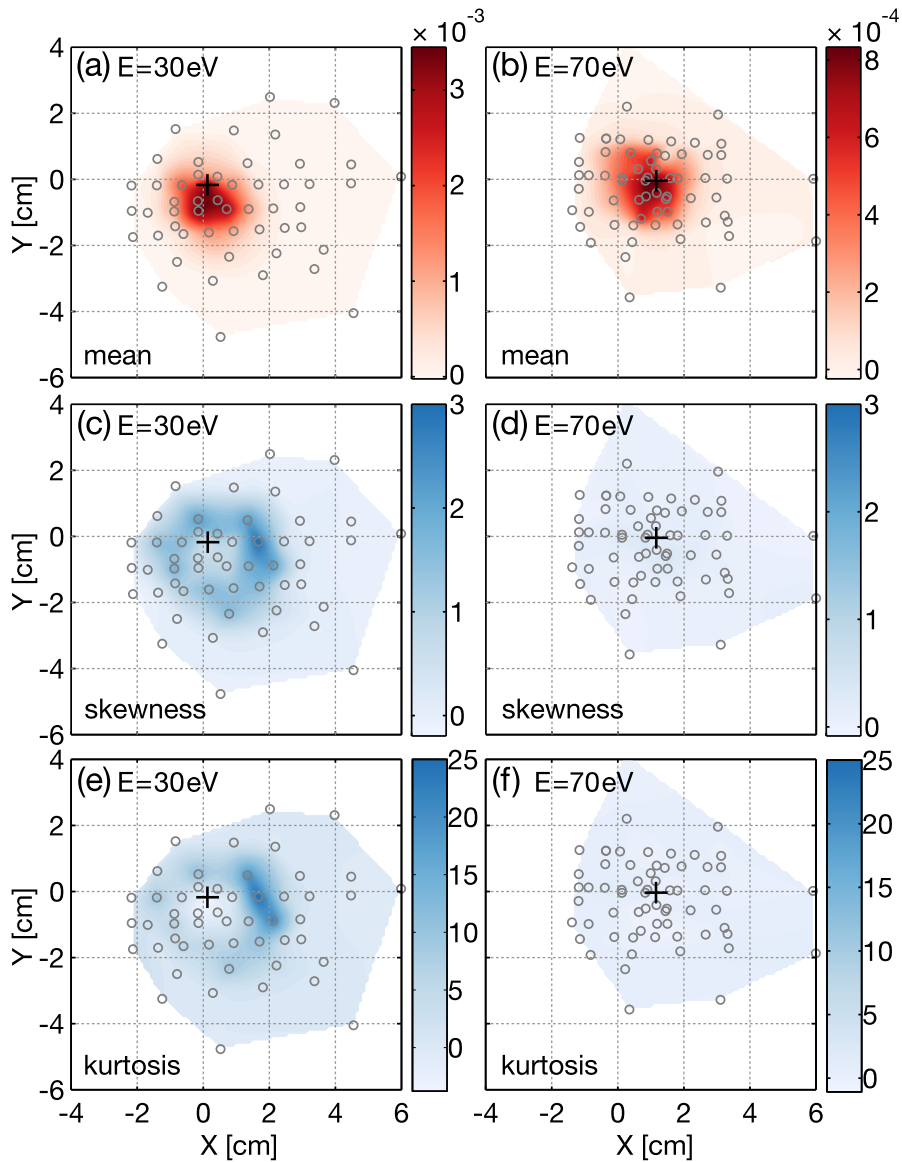


**Figure 8.3** | Poloidal profiles of the time-averaged suprathermal ion current density, in  $A/m^2$ , for ions at 30 eV (a) and 70 eV (b). The profile of the skewness, (c) and (d), and kurtosis, (e) and (f), of the time-traces are also shown. The profiles of the skewness and kurtosis of the 30 eV ions ((c) and (e)) reveal a crown of high skewness and high kurtosis around the peak of time-averaged profile. This indicates that the broadening of the 30 eV suprathermal ion beam is due to intermittent bursts perturbing the gyro-motion of the ions. This pattern is not visible on the skewness and kurtosis profiles for 70 eV ions ((d) and (f)). Gray circles show the positions of measurements. The black crosses represent the position of the detector corresponding to the time traces shown in Fig. 8.2.

and kurtosis profiles for the 70 eV ion beam are flat, the profiles for the 30 eV ions reveal a region of high skewness and high kurtosis around the peak of maximum time-averaged current. This implies that, in the peripheral regions of the profile, where the time traces have a low time-averaged current compared to the center of the profile, the intermittency is more important. In the following, we show that this intermittency is caused by the interaction of the

suprathermal ions with blobs.

### 8.4 Conditionally averaged suprathermal ion current profiles

To identify the effect of blobs on the suprathermal ion beam we use the CAS over many blob events. To detect blobs, we use the Langmuir probe array HEX TIP [92] (Section 2.1.2) situated at a toroidal angle of  $240^\circ$  away from the detector (see Fig. 8.1). Blobs are defined as bursts in the ion saturation current characterized by  $n\sigma < \tilde{I}_{\text{sat}} < m\sigma$ , where  $\tilde{I}_{\text{sat}} = I_{\text{sat}} - \bar{I}_{\text{sat}}$  is the ion saturation current fluctuations,  $\sigma$  is the standard deviation of the ion saturation current signal and,  $n$  and  $m$  are factors allowing to select the amplitude of events in a certain range. The suprathermal ion current is averaged in a time window centered around each blob event. This procedure is applied to the phase with and without suprathermal ions. The difference between the two CAS shows the dynamic of the suprathermal ion beam when a blob is detected on a given probe tip of HEX TIP.

Figure 8.4 shows the time evolution of the conditionally-averaged suprathermal ion current profile for the 30 eV ions (see the supplementary material of [41] for a movie showing the same data). The reference probe is positioned at  $X = 0$  cm and  $Y = 12.1$  cm and all events exceeding a level corresponding to  $n = 3$  are selected. Due to the helical magnetic configuration, blobs detected on this tip are aligned to a magnetic field line that is located at  $X = 0$  cm,  $Y = -0.5$  cm at the toroidal location of the detector, which is close to the maximum of the time-averaged profiles (Figs. 8.3(a) and (b)). Figure 8.4 shows the CAS analysis from  $-64 \mu\text{s}$  before to  $64 \mu\text{s}$  after the detection of the blob. This time interval corresponds approximately to the autocorrelation time of floating potential fluctuations in the blob region ( $\tau_{\text{corr}, V_{\text{fl}}} \approx 42 \mu\text{s}$ ) and of  $I_{\text{sat}}$  fluctuations ( $\tau_{\text{corr}, I_{\text{sat}}} \approx 52 \mu\text{s}$ ). First, the beam is displaced to the top-left with respect to its time-averaged profile (gray contours) (Figs. 8.4(a), (b) and (c)). Then, when the blob crosses the probe (Figs. 8.4(d), (e) and (f)), the displacement changes from left to right. At later times (Figs. 8.4(g), (h) and (i)), the beam is displaced to the bottom right of its averaged position. The time scale of the beam displacement is comparable to the duration of the intermittent bursts shown in Fig. 8.2(a). This is demonstrated by the value of the autocorrelation time ( $\tau_{\text{corr}} \approx 22 \mu\text{s}$ ) of the most intermittent suprathermal ions time traces (with a skewness above 2) which is comparable to the  $I_{\text{sat}}$  autocorrelation time. Figure 8.5 show that as the same CAS blob crosses the 70 eV ion beam, the displacement of the beam is extremely small compared to the one of the 30 eV beam.

As the time of flight between the source and the detector is smaller for 70 eV ions ( $t_{f,70\text{eV}} \approx 9 \mu\text{s}$ ) than for 30 eV ions ( $t_{f,30\text{eV}} \approx 13 \mu\text{s}$ ), a smaller perpendicular displacement is expected for 70 eV ions. The maximum displacement of the center of mass of the 30 eV ion beam is  $d_{\perp,30\text{eV}} \approx 0.8$  cm and  $d_{\perp,70\text{eV}} \approx 0.3$  cm for the 70 eV ion beam. Considering the simplified picture of the effect of a blob as inducing a perpendicular displacement at a constant velocity of the guiding center of the ions, the perpendicular displacement is given by  $d_{\perp} = v_{\perp} t_f$ , where  $v_{\perp} = \tilde{E}/B$  and  $\tilde{E}$  is the electric field of the blob. Since the electric field is the same in both

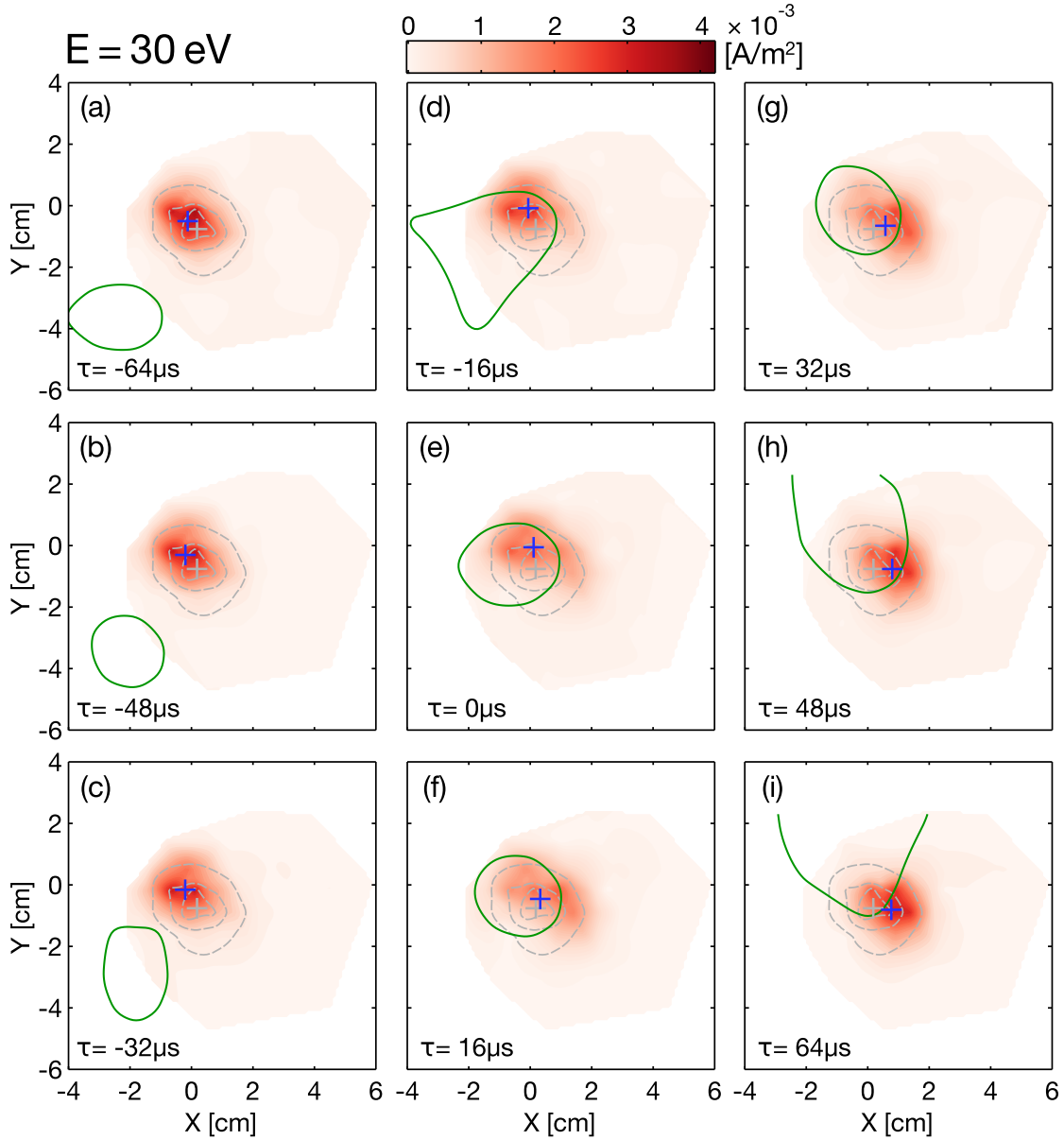


**Figure 8.4** | Conditionally averaged dynamics of the suprathermal ion current density [ $\text{A}/\text{m}^2$ ] for the 30 eV case at nine different times. Dashed gray contours represent time-averaged profiles (Fig. 8.3) and the green contour represents the blob averaged  $I_{\text{sat}}$  profile. The center of mass positions of the beam and of the time-averaged profiles are indicated by blue and gray crosses, respectively.

cases, we should have  $\frac{d_{\perp,30\text{eV}}}{d_{\perp,70\text{eV}}} = \frac{t_{f,30\text{eV}}}{t_{f,70\text{eV}}}$ . Instead, we find  $\frac{d_{\perp,30\text{eV}}}{d_{\perp,70\text{eV}}} \approx 2.7 > 1.4 \approx \frac{t_{f,30\text{eV}}}{t_{f,70\text{eV}}}$ . This indicates a weaker interaction between suprathermal ions and blobs in the 70 eV case than in the 30 eV case, consistent with the absence of intermittency in the current time traces in Fig. 8.2(b) and Fig. 8.3(d) and with an increased effect of gyroaveraging for ions having larger Larmor radii [47]. The value of the electric field estimated from the displacement of the 30 eV ion beam is  $\tilde{E} \approx 45 \text{ V}/\text{m}$ , which is comparable to previously measured values [77, 95].

## 8.5. Analysis of the suprathreshold ion beam displacement

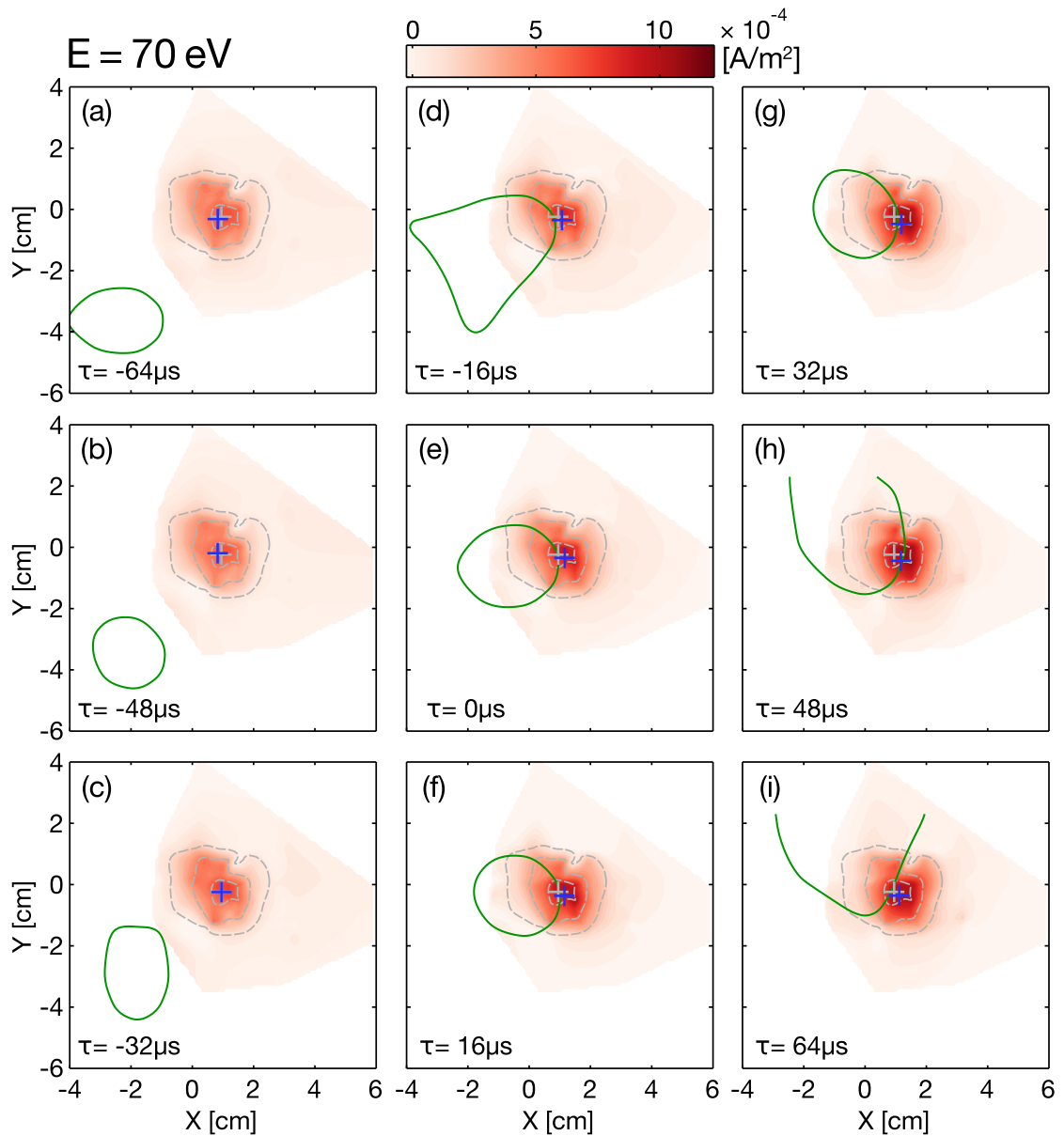


**Figure 8.5** | Conditionally averaged dynamics of the suprathreshold ion current density [ $\text{A}/\text{m}^2$ ] for the 70 eV case at nine different times. Dashed gray contours represent time-averaged profiles (Fig. 8.3) and the green contour represents the blob averaged  $I_{\text{sat}}$  profile. The center of mass positions of the beam and of the time-averaged profiles are indicated by blue and gray crosses, respectively.

Figure 8.6 shows the same analysis, for both energies, but with a blob passing far away from the ion beam (the reference probe position is  $X = 10.5$  cm,  $Y = 0$  cm). In this case the beam is not perturbed.

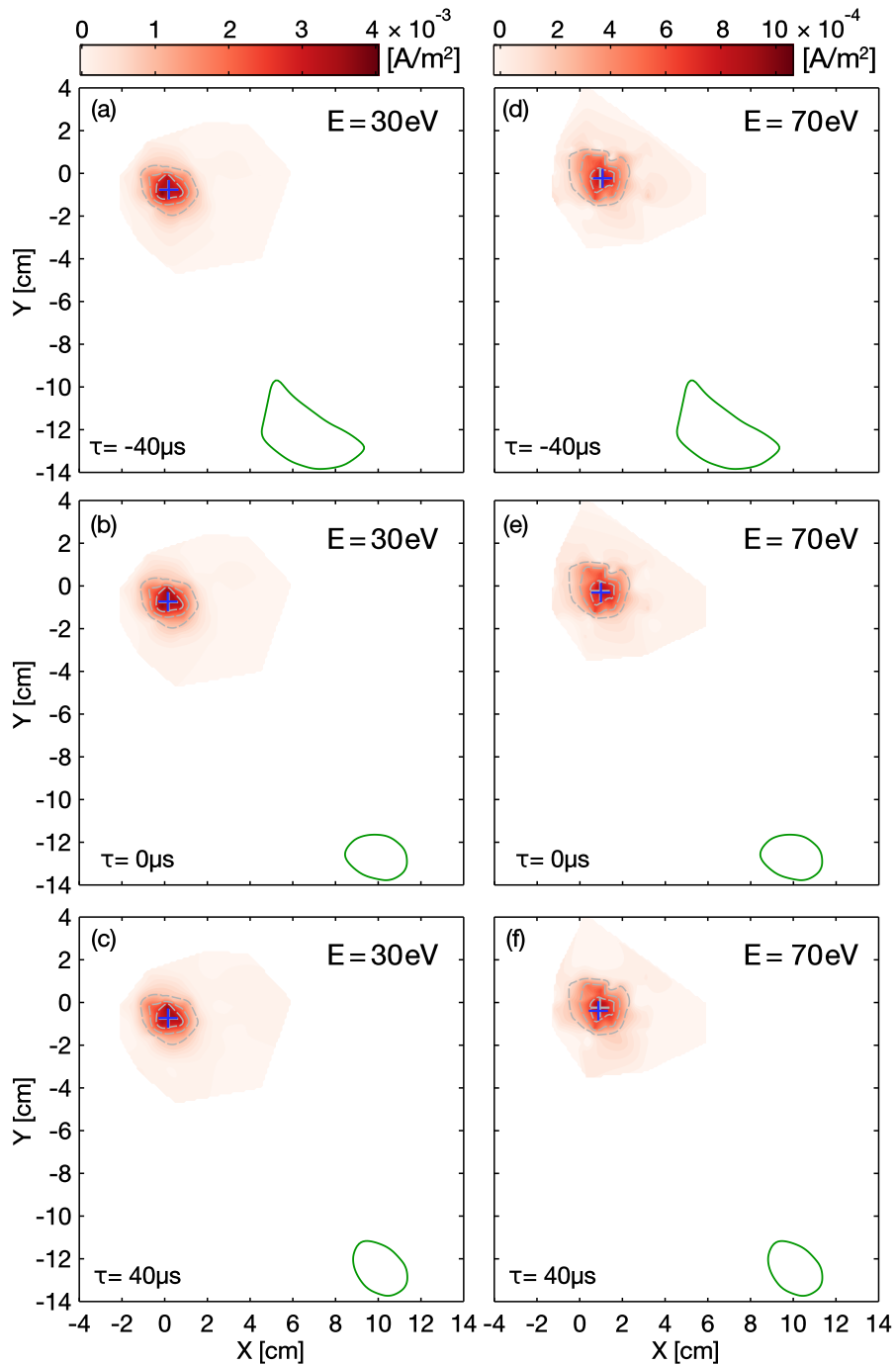
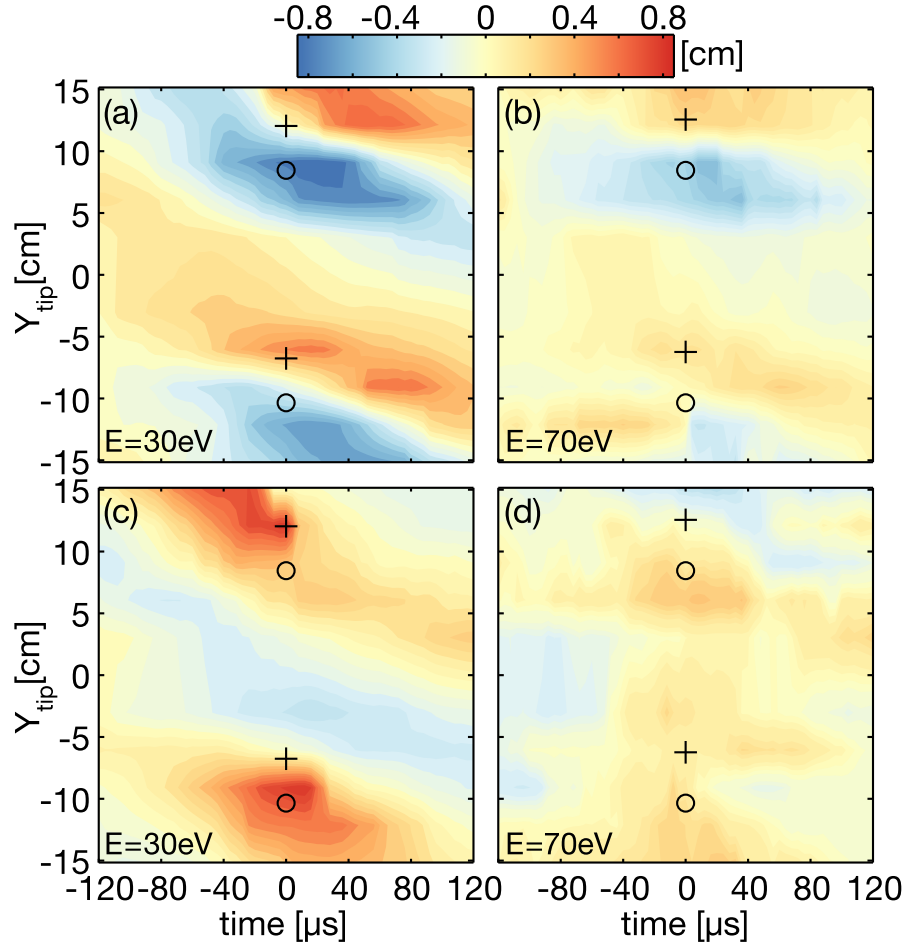


**Figure 8.6** | Conditionally averaged dynamics of the suprathermal ion current density  $[\text{A/m}^2]$  for the 30 eV (left) and 70 eV (right) cases but with a blob passing far away from the beam. The reference probe position is  $X = 10.5 \text{ cm}$ ,  $Y = 0 \text{ cm}$ . In this case the beams are not perturbed. Note the  $X, Y$  scale difference with respect to Figs. 8.4 and 8.5.

### 8.5 Analysis of the suprathermal ion beam displacement

To investigate the mechanisms perturbing the trajectories of suprathermal ions, we study the effect of blobs at different positions in the poloidal plane. Using probe tips at different

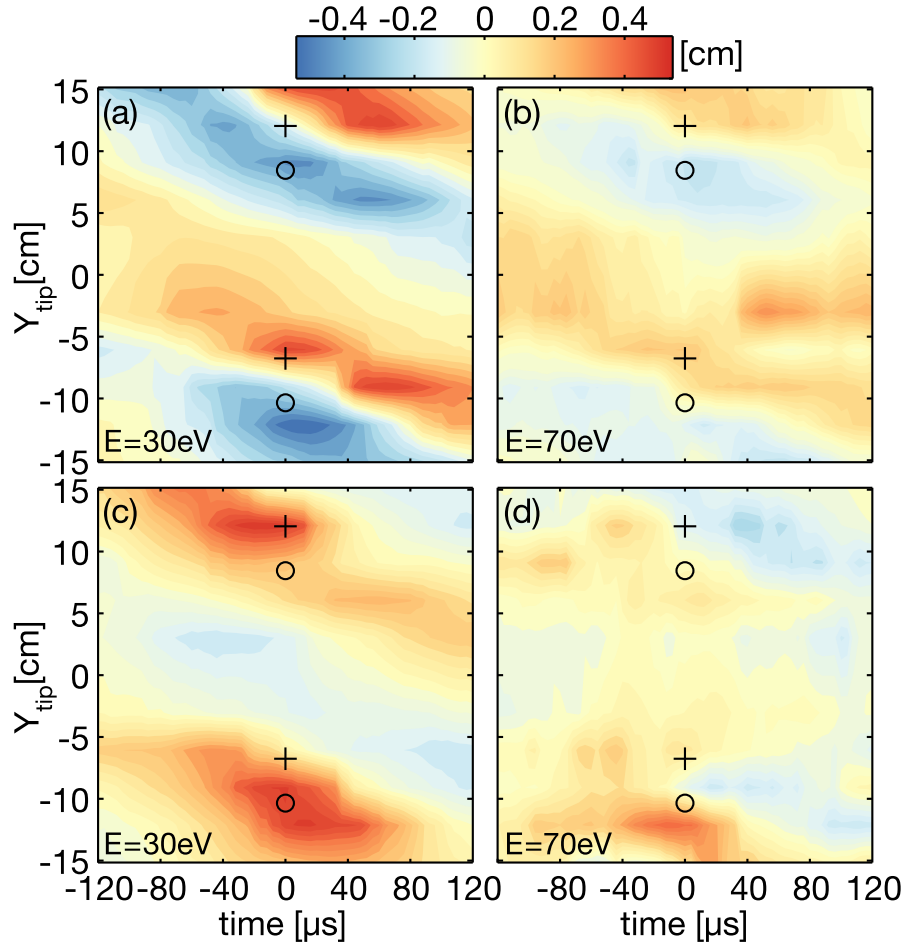
## 8.5. Analysis of the suprathermal ion beam displacement



**Figure 8.7** | Horizontal (top row) and vertical (bottom row) displacement of the suprathermal ion beam due to large blobs ( $\tilde{I}_{\text{sat}} > 4\sigma$ ) for 30 eV and 70 eV suprathermal ions. On all panels, the x-axis represents the time relative to the detection of the blob on the reference probe and the y-axis represents the vertical position of the reference probe. The crosses and the circles indicate the positions of the beam center, when it reaches the detector, and of the source, respectively, projected along the helical magnetic field lines on the poloidal plane of the reference probes (see Fig. 8.1). The measurement error is  $\pm 1$  mm. The vertical periodicity of the magnetic field is reflected in the pattern with a field line return distance of  $\Delta \approx 18.8$  cm.

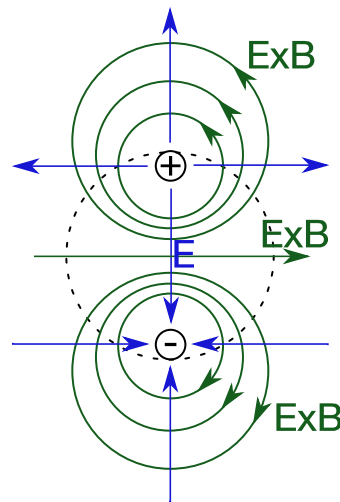
vertical positions between the radial position  $0 \text{ cm} \leq X \leq 1.7 \text{ cm}$  as reference probes for the CAS, we compute the horizontal and vertical displacement of the beam center of mass as a function of time. We separate the blobs in two classes, depending on the amplitude of their  $I_{\text{sat}}$  fluctuations: small blobs with  $2\sigma < \tilde{I}_{\text{sat}} < 4\sigma$  and large blobs with  $\tilde{I}_{\text{sat}} > 4\sigma$ .

Figure 8.7 shows the horizontal and vertical displacement for 30 eV and 70 eV ions due to large blobs. The circles represent the position of the suprathermal ion source projected along the helical magnetic field lines on the poloidal plane of the reference probes. The crosses represent the position of the beam center, when it reaches the detector, projected onto the same plane. Thus, the vertical distance between the circles and the crosses show the vertical distance



**Figure 8.8** | Horizontal (top row) and vertical (bottom row) displacement of the suprathermal ion beam due to small blobs ( $2\sigma < \tilde{I}_{sat} < 4\sigma$ ) for 30 eV and 70 eV suprathermal ions.

traveled by the ions between their emission and their detection due to the vertical drift. The error on the displacement is estimated by simulating the measurements on prescribed profiles and is  $\pm 1$  mm. Figure 8.8 shows the horizontal and vertical displacement for 30 eV and 70 eV ions due to small blobs. We observe that 30 eV ions are systematically more significantly displaced by the blobs than 70 eV ions. Figures 8.7 and 8.8 reveal also that, depending on its position relevant to that of the blob, the beam can be displaced inwards or outwards. We note that, the beams are not displaced when a blob transits far away (for probes located at  $Y \approx 0$  cm). We observe that blobs passing above the beam tend to move it outwards and that blobs passing below it tend to move it inwards. The plasma potential associated with blobs in TORPEX has been identified with a bipolar structure that results from the  $\nabla B$  and curvature-induced charge separation inside them [100]. The electric field and  $\mathbf{E} \times \mathbf{B}$  velocity field associated with a blob are schematically represented in Fig. 8.9. The observed suprathermal ion beam displacement is consistent with the bipolar potential structure, taking into account that in the present plasma conditions the blob motion can have a strong vertical component. Figure 8.8 shows that lower amplitude blobs induce the same pattern of displacements with amplitudes smaller



**Figure 8.9** | simplified schematic of a blob showing the electric field and  $\mathbf{E} \times \mathbf{B}$  velocity field associated with the plasma potential dipole.

by about a factor two.

## 8.6 Conclusions

In summary, thanks to unprecedented time-resolved measurements, we show that suprathermal ions in TORPEX plasmas experiencing superdiffusive transport are associated with bursty displacement events resulting in highly intermittent time traces. Suprathermal ions experiencing subdiffusive transport do not display such intermittency. The intermittency of the time traces is quantified by the skewness and kurtosis of their fluctuations. For superdiffusive ions, the skewness and kurtosis poloidal profiles reveal a crown around the peak of maximum current, where the fluctuations are the most intermittent. Using CAS measurements, we prove that the intermittency in the superdiffusive ions is due to their higher sensitivity to intermittent blobs, which move the ions through their electrical field both inwards and outwards depending on their relative location. Larger blobs have a greater effect than smaller blobs.

Our work links observations usually inaccessible in fusion devices and astrophysical plasmas, namely energy-resolved three-dimensional time-averaged measurements (Chapter 7), with Eulerian time-resolved measurements, which are often the only accessible measurements in such experiments. The presence of large fluctuations in the time traces of superdiffusive ions corroborates our previous theoretical study, where we showed that Lévy, heavy-tailed, statistics govern this regime [145, 167] (Chapter 6).



## 9 Conclusions

In magnetic fusion and space plasmas, the transport of suprathermal ions is determined mainly by turbulence [47, 179] with Coulomb collisions playing only a minor role. In magnetic fusion reactors, fusion-generated alpha particles regulate the burning plasma regime, in which reactors will necessarily operate, providing the dominant fraction of the plasma heating [12]. Losses or internal redistribution of suprathermal ions need to be controlled as they can affect the burn dynamics, degrade the fusion energy production and damage the reactor structure. In space, superdiffusive transport is thought to play a role in the long-standing problem of cosmic ray acceleration [51, 52, 57] and in the transport of solar energetic particles that can be harmful to spacecraft functioning [42, 56, 58].

The transport of suprathermal ions in turbulence is a complex process that depends on the interplay between the ion orbits and the turbulent structures. Investigating this phenomenon requires detailed knowledge of the characteristics of the suprathermal ions trajectories and of the turbulence. TORPEX, with its easy access for diagnostics and its well characterized turbulent regimes, is an ideal testbed to carry out a systematic study of the suprathermal ion transport. Curvature and gradient of the magnetic field, due to the toroidal configuration of TORPEX, generate drifts of the suprathermal ions and a turbulence that is dominated by intermittent field-elongated structures, features that are also characteristics of tokamak plasmas. Detailed numerical simulations of the interaction of suprathermal ions with validated simulations of turbulence are also necessary to precisely characterize the suprathermal ion transport and to unveil the mechanisms responsible for it.

During this Thesis, the design of the suprathermal ion source initially developed in TORPEX was modified. The new design improves the insulation of the electric parts, which increases the source performance, and facilitates its assembly. An analog lock-in detector that allows one to remove the capacitive noise due to the source voltage modulation was realized. A motorized cart allowing to remotely move the source along the toroidal direction and a second GEA detector were built. These ameliorations and additions to the suprathermal ion experimental setup permitted us to considerably accelerate the numerous and long-lasting measurements of the suprathermal ion current profiles.

## Chapter 9. Conclusions

---

To characterize the transport of suprathermal ions, poloidal profiles of their current density were measured with the two GEA detectors at a number of toroidal locations along the suprathermal ion beam allowing its 3D reconstruction. These measurements reveal the vertical drift experienced by the suprathermal ions and the oscillations of the beam width due to their gyromotion. Experiments were conducted with two different suprathermal ion injection energies, 70 eV and 30 eV. A broadening of the suprathermal ion beam due to its interaction with the turbulence was observed. The turbulent broadening is considerably more important for the ions injected with the smaller energies, indicating that the transport regime experienced by the ions depends on their energy.

Numerical simulations reproducing the experiments were conducted. Modeling of the background plasma turbulence with the fluid code GBS was performed to carefully match experimental measurements of the plasma potential profiles. Numerical simulations of the suprathermal ion transport in the simulated turbulent fields were performed with initial parameters mimicking the experimental parameters. A comparison of the experimental and numerical results was conducted by applying a synthetic diagnostic to the code output. The comparison of the experimental radial beam width with the one from the synthetic diagnostic shows a good agreement. The numerical simulations, in agreement with the experimental measurements, allow us to precisely characterize the transport experienced by the suprathermal ions by computing the values of the radial transport exponent,  $\gamma_R$ , from the temporal evolution of the variance of displacements. The transport is at first ballistic ( $\gamma_R = 2$ ) during approximately one gyroperiod. The ions enter then the interaction phase where the transport is found to be superdiffusive ( $\gamma_R \simeq 1.2$ ) for 30 eV ions and subdiffusive ( $\gamma_R \simeq 0.5$ ) for 70 eV ions. For 30 eV ions, a third phase, featuring a transport close to diffusive ( $\gamma_R \simeq 0.9$ ) is found. It was found that the mechanisms of gyroaveraging and drift-averaging were more important for 70 eV than for 30 eV, effectively reducing the transport.

A theoretical model based on a stochastic equation describing the trajectories of the particles was developed. This model, the asymmetric fractional Lévy motion (afLm), generalizes the classic Brownian motion to include long-range temporal correlations and heavy-tailed PDF of step sizes that can be asymmetrically distributed. The corresponding macroscopic equation for the temporal evolution of the radial particle density was derived. This equation uses a fractional differential operator with non-zero skewness and a time dependent diffusivity. The solutions of this equation fit very well the PDF of particle density from the numerical simulations in subdiffusive and superdiffusive cases. This model provides the values of the spatial transport exponent  $\alpha$ , indicating the departure from Gaussianity, the temporal transport exponent  $\beta$ , revealing the presence of positive or negative temporal correlations, and the asymmetry parameter  $\theta$ . These parameters gives an insight into the microscopic processes at play that was not accessible before. The superdiffusive transport is found to be characterized by heavy-tailed (Lévy) asymmetric PDFs and the subdiffusive transport is characterized by anti-persistent, negatively correlated trajectories.

To identify the effect of blobs on the suprathermal ions, time-resolved measurements of the

---

suprathermal ion current were performed in the interaction phase, for 70 eV and 30 eV ions. A sharp difference was revealed in the intermittency of the time traces, characterized by their skewness and kurtosis. A crown of high intermittent signals is observed in the surrounding of the 30 eV indicating that, in this case, the ions reach the detector in bursts. This is not observed for 70 eV ions. The technique of conditional average sampling allowed us to identify the role of blobs. 30 eV ions are found to be more sensitive to the turbulent  $\mathbf{E} \times \mathbf{B}$  fields associated with the blobs. The intermittency observed in these Eulerian measurements for the 30 eV ions is consistent with the Lagrangian descriptions depicted in the afLm, where Lévy PDFs are found in the superdiffusive case.

While our findings cannot be directly extrapolated to fusion and astrophysical plasmas, they advance the basic understanding of the turbulent transport of suprathermal ions and serve as a proof-of-principle that suprathermal ion transport is generally non-diffusive and that it depends on the energy of the ions.

Presently, most predictions of turbulent transport of energetic particles are based on a diffusion model, in which ad-hoc “anomalous” diffusion coefficients are inserted, implying a transport that is Gaussian and Markovian. This assumption can lead to false extrapolations and misleading estimates of the importance of fundamental processes: in our case the orbit averaging and effect of turbulent structures. Our observations of non-diffusive transport in this simple magnetized torus support the importance of considering alternative descriptions to canonical diffusion equations, such as fractional diffusion equations [122, 167]. Future fusion reactors will rely on good confinement of energetic ions, the motion of which may be non-diffusive in some cases. Moreover, in burning plasmas, strong intermittency in the transport of suprathermal ions can be a concern, because of possible effects on the core reactivity, and, more importantly on the heat load that the suprathermal ions may produce on the reactor first wall even in situations of negligible average loss rates.

Studying suprathermal ions in field-elongated turbulent structures may also help explain the transport of energetic particles in magnetic flux tubes of the solar wind. For example, “dropouts” in the intensity of solar energetic particle fluxes were measured by spacecrafts [180] and are still not well understood [42, 181–183].

The understanding of suprathermal ion transport in TORPEX could be further consolidated by a number of future experiments. The turbulence characteristics could be varied by changing the injection position, for example by injecting the ions in the mode region. Varying the number  $N$  of magnetic field line turns would also change the value of the ideal-interchange mode vertical wave-number that may affect the vertical size of the blobs. Using different gas to create the plasma would also have an effect on the size and velocity of the blobs [100]. The transport of suprathermal ions could also be studied in the resistive-interchange mode or with the closed field line configurations. In the closed field line configuration, X-points can be created and studying the transport across these could be of interest for fusion and astrophysical plasmas where acceleration of particles is also observed during magnetic reconnection events.

## Chapter 9. Conclusions

---

In this configuration, the interaction with Alfvén waves excited by the in-vessel toroidal conductor could also be studied [74]. Numerical simulations solving the trajectories of the suprathermal ions in 3D turbulence are already available and would need to be adapted to the TORPEX geometry. Injecting ions with different masses, which would change their Larmor radii and cyclotron frequencies, is also possible by using different emitters doped with other alkali than lithium. The phenomenon of fast ion acceleration could also be studied in 3D turbulence with detectors allowing to precisely measure the ion energy. The tools developed for the study of suprathermal ion transport in the context of this Thesis, such as the numerical simulations and the analysis technique could be applied to the study of fast electron transport using, for example, an electron gun.

The theoretical model of the asymmetric fractional Lévy motion (afLm) could be refined with the inclusion of tempered fractional derivatives [173] that could take into account the observed cut-off of heavy tails and the transition from the interaction phase to the asymmetric phase.

Conditionally averaged measurements could be performed with the addition of the FRIPLE probe, resolving the blob plasma potential structure, and the fast-framing camera, that could resolve the blob with a greater resolution than the Langmuir probes, revealing the blob finer structures. Time-resolved measurements could be taken simultaneously by several GEAs to investigate the correlations existing between the blobs and the different ion trajectories or between the ions themselves. The ballistic and the asymmetric phases could also be investigated with time-resolved measurements. An interesting possibility would be to use the technique of laser-induced fluorescence in combination with optical tagging to create and detect test particles among the suprathermal ions.

Moreover, the characterization of the Eulerian time-trace intermittency started here could be extended with techniques that can identify non-classical scalings, such as multifractal analysis [83, 177], structure function scaling [184] or diffusion entropy analysis [138]. The nature of the link between the Lagrangian characterization of the turbulent transport, provided for example by the self-similarity (Hurst) exponent,  $H$ , which we computed here, and the Eulerian characterization of the transport still represents an outstanding open question.

# A Stable distributions

We recall here the main properties of  $\alpha$ -stable random variables and distributions (also called Lévy  $\alpha$ -stable distributions), although we refer the reader to reference [126] for a detailed monograph. The generalized central limit theorem states that stable distributions are the limiting distributions of normalized sums of independent, identically distributed random variables. The Gaussian distribution is a particular case that corresponds to the case where the random variables have a finite variance. Stable distributions are especially interesting because, with the exception of the Gaussian distribution, they allow heavy-tails and non-zero skewness. Their probability densities exist and are continuous, but their expressions in closed form exist only for a few particular cases (Gaussian, Cauchy and Lévy distributions) and they are usually described by their characteristic function, i.e. their Fourier transform.

A random variable  $X$  is said to be stable if for any  $A, B > 0$  there is  $C > 0$  and  $D \in \mathbb{R}$  such that [126]

$$AX + BX = CX + D. \quad (\text{A.1})$$

Moreover, for any stable random variable there is a number  $\alpha \in (0, 2]$  such that

$$C^\alpha = A^\alpha + B^\alpha. \quad (\text{A.2})$$

The Gaussian distribution corresponds to the case  $\alpha = 2$ .

Different parameterizations of their characteristic function are possible. We adopt here the following parameterization for the stable distribution  $L_{\alpha, \sigma, \mu}^\theta$  (close to parameterization C in [185]):

$$\mathcal{F}[L_{\alpha, \sigma, \mu}^\theta(x)](k) = \exp\left\{-\sigma^\alpha |k|^\alpha e^{i \operatorname{sign}(k) \frac{\theta \pi}{2}} + i k \mu\right\}. \quad (\text{A.3})$$

Here  $\alpha \in (0, 2]$  is the *index of stability* or *characteristic exponent*,  $\sigma > 0$  is the *scale parameter*,  $\theta$  is the *asymmetry parameter* ( $|\theta| \leq \min(\alpha, 2 - \alpha)$ ) and  $\mu \in \mathbb{R}$  the *shift parameter*. For example, the Gaussian distribution is found for  $\alpha = 2$  and has mean equal to  $\mu$  and standard deviation

## Appendix A. Stable distributions

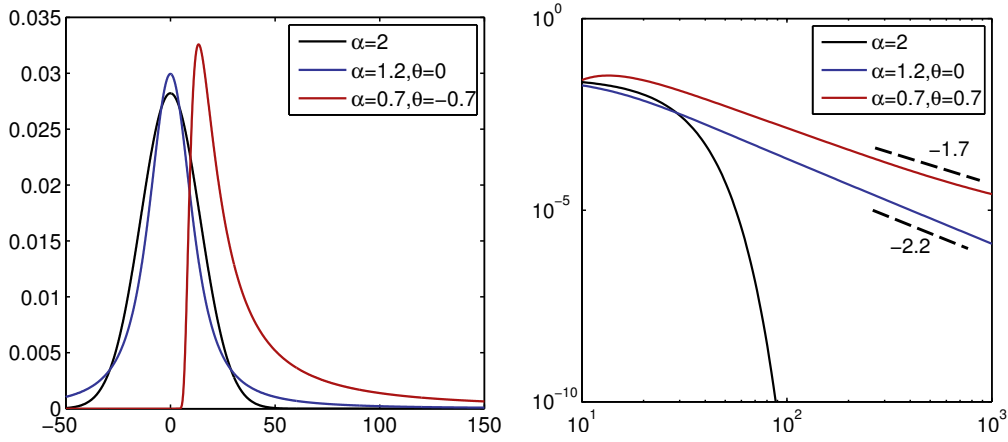


**Figure A.1** | Example of stable distributions on a lin-lin (left) and log-log scale (right). All the distributions have shift parameter  $\mu = 0$  and scale parameter  $\sigma = 10$ . A Gaussian distribution is shown in black ( $\alpha = 2$ ), a distribution with  $\alpha = 1.2$  in blue and a one sided distribution (totally skewed to the right) in red. The log-log scale shows the heavy tails of the distributions with  $\alpha < 2$ , with exponent  $-(\alpha + 1)$ .

equal to  $\sqrt{2}\sigma$  (the asymmetry parameter  $\theta$  is equal to zero when  $\alpha = 2$ ). When  $\mu = 0$ , the class of distributions reduces to the strictly stable distribution  $L_{\alpha,\sigma}^{\theta}$  and when  $\mu = \theta = 0$ , the class of distributions reduces to the symmetric  $\alpha$ -stable distributions,  $L_{\alpha,\sigma}$ .

When  $\alpha < 2$ , stable distributions have the interesting property of having one tail, if their skewness is maximum, or both tails that behave asymptotically as power laws (heavy-tail) [126],

$$L_{\alpha,\sigma,\mu}^{\theta}(x) \sim \frac{1}{|x|^{\alpha+1}}, \text{ when } |x| \rightarrow \infty. \quad (\text{A.4})$$

As a result, they always have infinite variance when  $\alpha < 2$ , which reflects their capability of modeling processes with large fluctuations. For  $\alpha < 1$  they also have infinite first moments.

Stable distributions that have  $\alpha < 1$  and are totally skewed to the right or to the left ( $\theta = \pm\alpha$ ) are *one sided*. They are only defined for  $x > 0$  if  $\theta = -\alpha$  and for  $x < 0$  if  $\theta = \alpha$ .

For  $\mu = 0$  and  $\theta = -\alpha$ , their Laplace transform is given by [126]

$$\mathcal{L}[L_{\alpha,\sigma}(x)](s) = \exp\left\{-\frac{\sigma^{\alpha}}{\cos\frac{\pi\alpha}{2}}s^{\alpha}\right\}. \quad (\text{A.5})$$

Although no expression in closed form exists for the general stable distributions (they are expressed with transcendental functions known as Mittag-Leffler functions [129]), numerical algorithms allow to compute their probability distribution function with great accuracy and very efficiently (see [186] for example).

## B Fractional differential operators

The idea of generalizing the differential operation to fractional order is as old as differential calculus. Leibniz, Euler, Liouville, Riemann and Fourier are among the many great mathematicians who developed fractional differential calculus. It is only more recently, in the second half of the 20th century, that it began to be applied in physics and engineering, to problems such as the modeling of viscoelasticity in materials [187] or dynamical processes in fractals [188].

Among the different definitions, one of the most famous is the *Riemann-Liouville differential operators* that can be defined explicitly by means of the integral operators [141, 189]. The left and right Riemann-Liouville fraction derivative of order  $\alpha$  are

$${}_a D_x^\alpha f(x) \equiv \frac{1}{\Gamma(m-\alpha)} \frac{d^m}{dx^m} \left[ \int_a^x \frac{f(x')}{(x-x')^{\alpha-m+1}} dx' \right] \quad (\text{B.1})$$

and

$${}_b D_x^\alpha f(x) \equiv \frac{-1}{\Gamma(m-\alpha)} \frac{d^m}{d(-x)^m} \left[ \int_x^b \frac{f(x')}{(x-x')^{\alpha-m+1}} dx' \right], \quad (\text{B.2})$$

where  $\Gamma(t) = \int_0^\infty x^{t-1} e^{-x} dx$  is the gamma function,  $m$  is the integer satisfying  $m-1 < \alpha < m$  and  $a$  and  $b$  are the start and end point of the operators. We immediately see from these definitions that an important difference of the fractional version of the derivative of a function at a point  $x$  is that it is *not a local* property. As a matter of fact they can depend on the value of the function very far from  $x$ . In the cases in which the start point  $a$  or the end point  $b$  extend all the way to infinity, the following notation is generally used

$$\frac{d^\alpha f}{dx^\alpha} \equiv {}_{-\infty} D_x^\alpha f(x) \quad \text{and} \quad \frac{d^\alpha f}{d(-x)^\alpha} \equiv {}^{+\infty} D_x^\alpha f(x). \quad (\text{B.3})$$

The Fourier transform of these operators sheds light on their signification and their usage as they appear as a natural generalization of the Fourier transform of the derivative operator

$$\mathcal{F} \left[ \frac{d^\alpha f}{dx^\alpha} \right] = (-ik)^\alpha \hat{f}(k) \quad \text{and} \quad \mathcal{F} \left[ \frac{d^\alpha f}{d(-x)^\alpha} \right] = (ik)^\alpha \hat{f}(k). \quad (\text{B.4})$$

## Appendix B. Fractional differential operators

---

A symmetrization of these operators leads to the *Riesz fractional derivative operator* [141, 156]

$$\frac{d^\alpha f}{d|x|^\alpha} \equiv -\frac{-1}{2 \cos(\pi\alpha/2)} \left( \frac{d^\alpha f}{dx^\alpha} + \frac{d^\alpha f}{d(-x)^\alpha} \right) \quad (\text{B.5})$$

with the following Fourier transform

$$\mathcal{F} \left[ \frac{d^\alpha f}{d|x|^\alpha} \right] = |k|^\alpha \hat{f}(k). \quad (\text{B.6})$$

A different definition than the Riemann-Liouville is the *Caputo fractional derivative operator* of order  $\beta$  [129, 187]

$${}_t^* D_t^\beta f(t) \equiv \frac{1}{\Gamma(m-\beta)} \left[ \int_0^t \frac{f^{(m)}(t')}{(t-t')^{\beta-m+1}} dt' \right] \quad \text{with} \quad m-1 < \beta < m. \quad (\text{B.7})$$

This definition of the fractional derivative is usually associated with derivatives in time because of the practical form of its Laplace transform

$$\mathcal{L} \left[ {}_t^* D_t^\beta f(t) \right] = s^\beta \hat{f}(s) - \sum_{k=0}^{m-1} s^{\beta-k-1} \frac{d^k f}{dt^k}(0) \quad (\text{B.8})$$

which depends only on the initial values of  $f(t)$  and its integer derivatives. The Laplace transform of the Riemann-Liouville derivative depends instead on the initial values of the fractional derivatives of lower order than  $\beta$ , which makes it not practical for real applications [187].

## C GBS simulations

The plasmas studied here are dominated by an ideal-interchange mode characterized by a wave-number parallel to the magnetic field lines  $k_{\parallel} \simeq 0$  (see Section 2.1.3). The GBS simulation used in this Thesis are thus run with the 2D version of the code, evolving the following equations for the line-integrated density,  $n(x, y, t)$ , electrostatic potential,  $\phi(x, y, t)$ , and electron temperature  $T_e(x, y, t)$  [67, 87]

$$\frac{\partial n}{\partial t} = R_0[\phi, n] + 2 \left( n \frac{\partial T_e}{\partial y} + T_e \frac{\partial n}{\partial y} - n \frac{\partial \phi}{\partial y} \right) + D_n \nabla^2 n - \sigma n \sqrt{T_e} \exp \left( \Lambda - \frac{e\phi}{T_e} \right) + S_n, \quad (\text{C.1})$$

$$\frac{\partial \nabla^2 \phi}{\partial t} = R_0[\phi, \nabla^2 \phi] + 2 \left( \frac{T_e}{n} \frac{\partial n}{\partial y} + \frac{\partial T_e}{\partial y} \right) + D_\omega \nabla^4 \phi + \sigma \sqrt{T_e} \left[ 1 - \exp \left( \Lambda - \frac{\phi}{T_e} \right) \right], \quad (\text{C.2})$$

$$\begin{aligned} \frac{\partial T_e}{\partial t} = R_0[\phi, T_e] + \frac{4}{3} \left( \frac{7}{2} T_e \frac{\partial T_e}{\partial y} + \frac{T_e^2}{n} \frac{\partial n}{\partial y} - T_e \frac{\partial \phi}{\partial y} \right) + D_T \nabla^2 T_e \\ - \frac{2}{3} \sigma \sqrt{T_e^3} \left[ 1.71 \exp \left( \Lambda - \frac{\phi}{T_e} \right) - 0.71 \right] + S_T, \end{aligned} \quad (\text{C.3})$$

where  $x$  is in the radial direction and  $y$  in the vertical direction and  $[\phi, f] = \partial_x \phi \partial_y f - \partial_y \phi \partial_x f$  is the Poisson bracket representing the convection of the quantity  $f$  by the  $\mathbf{E} \times \mathbf{B}$  drift.

Simulation parameters reported in Table C.1 are chosen to match the experimental profiles (Section 5.1.1). The density and temperature sources are modeled to mimic the EC and UH resonances in TORPEX with the following form [89]

$$S_\alpha(x) = S_{EC,\alpha} \exp \left[ -(x - x_{EC,\alpha})^2 / \lambda_{EC,\alpha}^2 \right] + S_{UH,\alpha} \exp \left[ -(x - x_{UH,\alpha})^2 / \lambda_{UH,\alpha}^2 \right], \quad (\text{C.4})$$

where  $\alpha = n$  or  $T$ . Density, temperature and plasma potential are normalized to reference values  $n_0$ ,  $T_{e0} = 2.1 \text{ eV}$  and  $\phi_0 = T_{e0}/e$ . Distances are normalized to  $\rho_s = 2 \text{ mm}$  and time to  $R_0/c_{s0}$  where  $c_{s0} = \sqrt{T_{e0}/m_i}$  [87]. Dirichlet boundary conditions are used for  $n$ ,  $T_e$  and

## Appendix C. GBS simulations

**Table C.1** | GBS simulation parameters.

Quantity	Symbol	Value	Information
nx		750	Number of radial grid points
ny		256	Number of vertical grid points
xmin		0	Minimum of radial coordinates
xmax		$200\rho_s$	Maximum of radial coordinates
ymin		0	Minimum of vertical coordinates
ymax		$90\rho_s$	Maximum of vertical coordinates
diff_theta	$D_n$	1	Diffusion coefficient for density
diff_tempe	$D_T$	1	Diffusion coefficient for temperature
diff_omega	$D_\omega$	1	Diffusion coefficient for vorticity
frict_theta	$\eta_n$	0	Friction coefficient for density
frict_tempe	$\eta_T$	0	Friction coefficient for temperature
frict_omega	$\eta_\omega$	0	Friction coefficient for vorticity
rorho_s	$R/\rho_s$	500	
sigma	$\sigma$	0.216	Parallel absorption
lambda	$\Lambda$	3	Sheath potential
SEC_theta	$S_{EC,n}$	0.9	Peak intensity of EC source for density
SUH_theta	$S_{UH,n}$	1.35	Peak intensity of UH source for density
SEC_tempe	$S_{EC,T}$	0.9	Peak intensity of EC source for temperature
SUH_tempe	$S_{UH,T}$	1.35	Peak intensity of UH source for temperature
wEC_theta	$\lambda_{EC,n}$	$2.5\rho_s$	Width of EC source for density
wUH_theta	$\lambda_{UH,n}$	$5.0\rho_s$	Width of UH source for density
wEC_tempe	$\lambda_{EC,T}$	$2.5\rho_s$	Width of EC source for temperature
wUH_tempe	$\lambda_{UH,T}$	$5.0\rho_s$	Width of UH source for temperature
x0EC_theta	$x_{EC,n}$	$30\rho_s$	Position of EC source for temperature
x0UH_theta	$x_{UH,n}$	$40\rho_s$	Position of UH source for density
x0EC_tempe	$x_{EC,T}$	$30\rho_s$	Position of EC source for temperature
x0UH_tempe	$x_{UH,T}$	$40\rho_s$	Position of UH source for density

$\omega = \nabla_\perp \phi$ . In the 2D case, the parameter  $\sigma$  represents the importance of the parallel losses and is usually set to  $R_0/L_c$ . This parameter depends on the ratio of the density in the middle of a field line to the density at the pre-sheath [161]. To match the experimental measurements of the gradient of the profiles, the value of  $\sigma$  was increased compared to the usual value [67]. Three-dimensional simulations, where this parameter is not free but is set by the parallel dynamics, show similar gradients than the ones we have in the 2D simulations, confirming this choice for  $\sigma$ .

## D Suprathermal ion collision frequencies

The collision frequency for transverse diffusion due to collisions with the thermal ions is [190]

$$\nu_i = 1.8 \times 10^{-7} \mu^{-1/2} E(\text{eV})^{-3/2} n_i (\text{cm}^{-3}) \lambda_{ii'} \simeq 16 \text{ Hz}, \quad (\text{D.1})$$

where  $\lambda_{ii'} = \ln \Lambda_{ii'} = \ln\left(\frac{b_{max}}{b_{min}}\right) \simeq 13$  is the Coulomb logarithm for collisions between suprathermal ions and thermal ions with  $b_{max} = \lambda_{D,i} = \sqrt{\frac{\epsilon_0 T_i}{n_i e}}$  and  $b_{min} = \frac{q^2}{4\pi\epsilon_0 E}$ . The mean free path for collisions with the thermal ions is

$$\lambda_{\text{mfp},i} = \frac{v}{\nu_i} \simeq 750 \text{ km}, \quad (\text{D.2})$$

which is much longer than the distance traveled by the ions in TORPEX ( $\simeq 2 \text{ m}$ ).

This is also the case for collisions with the neutral particles. The frequency of collisions and the mean free path between collisions with neutrals are given by

$$\nu_n = \nu n_n \sigma_n = \sqrt{\frac{2E}{m}} n_n \pi (r_{Li} + a_0)^2 \simeq 6.2 \text{ kHz} \quad \text{and} \quad \lambda_{\text{mfp},n} = \frac{v}{\nu_n} \simeq 8 \text{ m}, \quad (\text{D.3})$$

where  $r_{Li} = 152 \text{ pm}$  is the radius of lithium nucleus and  $a_0$  is Bohr radius.



# Acronyms

2D	two-dimensional.
3D	three-dimensional.
afLm	asymmetric fractional Lévy motion.
CAS	conditional average sampling.
CLT	central limit theorem.
CTRW	continuous time random walk.
EC	electron cyclotron.
fBm	fractional Brownian motion.
fGn	fractional Gaussian noise.
fLm	fractional Lévy motion.
FRIPLE	five-tip triple probe.
GBS	global Braginskii solver.
GEA	gridded energy analyzer.
GLE	generalized Langevin equation.
HEXTIP	hexagonal turbulence imaging probe.
HFS	high field side.
ICRH	ion cyclotron resonance heating.
LAPD	Large Plasma Device.
LFS	low field side.
lhs	left hand side.
LP	Lamgmuir probe.
NBI	neutral beam injection.
oBm	ordinary Brownian motion.
PDF	probability distribution function.
rhs	right hand side.
SMT	simple magnetized torus.
SOL	scrape-off layer.
TORPEX	TORoidal Plasma EXperiment.
UH	upper hybrid.



## Repeatedly used symbols

$R_0$	TORPEX major radius.
$a$	TORPEX minor radius.
$R$	Radial distance from the center of the torus.
$X$	Horizontal coordinate in the poloidal plane, $X = 0$ on the torus toroidal axis.
$Y$	Vertical coordinate in the poloidal plane, $Y = 0$ on the horizontal symmetry plane of the torus.
$\Delta$	Field line return vertical distance.
$N$	Number of toroidal field turns.
$\gamma_R$	Radial transport exponent.
$\alpha$	Spatial transport exponent of the fractional Lévy motion.
$\beta$	Temporal transport exponent of the fractional Lévy motion.
$H$	Self-similarity exponent, also called Hurst exponent.
$E$	Suprathermal ion energy.
$I_{\text{sat}}$	Ion saturation current.
$\lambda_D$	Debye length.
$L_n$	Density gradient scale length.
$n_e$	Electron density.
$\phi$	Plasma potential in the numerical simulations.
$\rho_L$	Suprathermal ion Larmor radius.
$T_e$	Electron temperature.
$T_i$	Ion temperature.
$V_{\text{fl}}$	Plasma floating potential.
$V_{\text{pl}}$	Plasma electric potential.



# Bibliography

- [1] Chen, F. F. *Introduction to plasma physics* (Plenum, New York, NY, 1974).
- [2] Keidar, M. *et al.* Cold atmospheric plasma in cancer therapy. *Phys. Plasmas* **20**, – (2013).
- [3] Freidberg, J. *Plasma Physics and Fusion Energy* (Cambridge University Press, 2007).
- [4] Moses, E. & the NIC Collaborators. The national ignition campaign: status and progress. *Nucl. Fusion* **53**, 104020 (2013).
- [5] Bocchi, M. *et al.* Numerical simulations of z-pinch experiments to create supersonic differentially rotating plasma flows. *The Astrophysical Journal* **767**, 84 (2013).
- [6] Keilhacker, M. Diffusion of trapped reversed magnetic field in a theta pinch in the presence of a probe. *Nucl. Fusion* **4**, 287 (1964).
- [7] Be'ery, I., Seemann, O., Goldstein, G., Fisher, A. & Ron, A. Flute growth rate of plasma jet in mirror machine. *Plasma Phys. & Controlled Fusion* **56**, 025006 (2014).
- [8] Peiry, J., Altmann, M. & Tonetti, G. Measurement of the poloidal configuration in the Lausanne belt pinch. In *Proc. 8th European Conference on Contr. Fusion and Plasma Physics*, vol. I (1977). *Proc. 8th European Conference on Contr. Fusion and Plasma Physics*, Prague, Vol. I, 75 (1977).
- [9] Besseghir, K. *Free-Boundary Simulations of ITER Advanced Scenarios*. Ph.D. thesis, SB, Lausanne (2013).
- [10] Bosch, H.-S. *et al.* Technical challenges in the construction of the steady-state stellarator Wendelstein 7-X. *Nucl. Fusion* **53**, 126001 (2013).
- [11] Aymar, R., Barabaschi, P. & Shimomura, Y. The ITER design. *Plasma Phys. & Controlled Fusion* **44**, 519–565 (2002).
- [12] Fasoli, A. *et al.* Chapter 5: Physics of energetic ions. *Nucl. Fusion* **47**, S264–S284 (2007).
- [13] Kazakov, Y., Kiptily, V., Sharapov, S., Eester, D. V. & Contributors, J. E. Study of icrh scenarios for thermal ion heating in jet d–t plasmas. *Nucl. Fusion* **52**, 094012 (2012).

## Bibliography

---

- [14] Zweibel, E. G. The microphysics and macrophysics of cosmic rays. *Phys. Plasmas* **20**, 055501 (2013).
- [15] Ackermann, M. *et al.* Detection of the characteristic pion-decay signature in supernova remnants. *Science (New York, N.Y.)* **339**, 807–11 (2013).
- [16] Nikolić, S. *et al.* An integral view of fast shocks around supernova 1006. *Science (New York, N.Y.)* **340**, 45–8 (2013).
- [17] Chen, L. & Zonca, F. Theory of Alfvén waves and energetic particle physics in burning plasmas. *Nucl. Fusion* **47**, S727–S734 (2007).
- [18] Heidbrink, W. W. Basic physics of Alfvén instabilities driven by energetic particles in toroidally confined plasmas. *Phys. Plasmas* **15**, 055501 (2008).
- [19] Graves, J. *et al.* Control of magnetohydrodynamic stability by phase space engineering of energetic ions in tokamak plasmas. *Nat. Commun.* **3**, 624 (2012).
- [20] Zonca, F. *et al.* Energetic particles and multi-scale dynamics in fusion plasmas. *Plasma Phys. & Controlled Fusion* **57**, 014024 (2015).
- [21] Dendy, R. *Plasma Physics: An Introductory Course* (Cambridge University Press, 1995).
- [22] Diamond, P., Itoh, S. & Itoh, K. *Modern Plasma Physics: Volume 1, Physical Kinetics of Turbulent Plasmas* (Cambridge University Press, 2010).
- [23] Naitou, H., Kamimura, T. & Dawson, J. M. Kinetic Effects on the Convective Plasma Diffusion and the Heat Transport. *J. Phys. Soc. Japan* **46**, 258–265 (1979).
- [24] Heidbrink, W. W. & Sadler, G. J. The behaviour of fast ions in tokamak experiments. *Nucl. Fusion* **34**, 535 (1994).
- [25] Manfredi, G. & Dendy, R. Test-Particle Transport in Strong Electrostatic Drift Turbulence with Finite Larmor Radius Effects. *Phys. Rev. Lett.* **76**, 4360–4363 (1996).
- [26] Günter, S. *et al.* Interaction of energetic particles with large and small scale instabilities. *Nucl. Fusion* **47**, 920–928 (2007).
- [27] Zhang, W., Lin, Z. & Chen, L. Transport of Energetic Particles by Microturbulence in Magnetized Plasmas. *Phys. Rev. Lett.* **101**, 095001 (2008).
- [28] Albergante, M., Graves, J. P., Fasoli, A. & Lapillonne, X. Microturbulence driven transport of energetic ions in the ITER steady-state scenario. *Nucl. Fusion* **50**, 084013 (2010).
- [29] Albergante, M., Fasoli, a., Graves, J., Brunner, S. & Cooper, W. Assessment of turbulent beam ion redistribution in tokamaks through velocity space-dependent gyrokinetic analyses. *Nucl. Fusion* **52**, 094016 (2012).

- 
- [30] Hauff, T. & Jenko, F. Mechanisms and scalings of energetic ion transport via tokamak microturbulence. *Phys. Plasmas* **15**, 112307 (2008).
- [31] Heidbrink, W. *et al.* Evidence for Fast-Ion Transport by Microturbulence. *Phys. Rev. Lett.* **103**, 1–4 (2009).
- [32] Turnyanskiy, M. *et al.* Measurement and control of the fast ion redistribution on MAST. *Nucl. Fusion* **53**, 053016 (2013).
- [33] Pace, D. C. *et al.* Energetic ion transport by microturbulence is insignificant in tokamaks. *Phys. Plasmas* **20**, 056108 (2013).
- [34] Del-Castillo-Negrete, D., Mantica, P., Naulin, V. & Rasmussen, J. Fractional diffusion models of non-local perturbative transport: numerical results and application to JET experiments. *Nucl. Fusion* **48**, 075009 (2008).
- [35] Zhou, S. *et al.* Turbulent transport of fast ions in the Large Plasma Device. *Phys. Plasmas* **17**, 092103 (2010).
- [36] Zhou, S. *et al.* Dependence of fast-ion transport on the nature of the turbulence in the Large Plasma Device. *Phys. Plasmas* **18**, 082104 (2011).
- [37] Bovet, A., Furno, I., Fasoli, A., Gustafson, K. & Ricci, P. Investigation of fast ion transport in torpex. *Nucl. Fusion* **52**, 094017 (2012).
- [38] Brown, R. & Booth, S. Private Communication, Oversteps, O=0 (2010).
- [39] Heidbrink, W. W. *et al.* Measurements of interactions between waves and energetic ions in basic plasma experiments. *Plasma Phys. & Controlled Fusion* **54**, 124007 (2012).
- [40] Bovet, A., Furno, I., Fasoli, A., Gustafson, K. & Ricci, P. Three-dimensional measurements of non-diffusive fast ion transport in TORPEX. *Plasma Phys. & Controlled Fusion* **55**, 124021 (2013).
- [41] Bovet, A., Fasoli, A. & Furno, I. Time-Resolved Measurements of Suprathermal Ion Transport Induced by Intermittent Plasma Blob Filaments. *Phys. Rev. Lett.* **113**, 225001 (2014).
- [42] Zimbardo, G. Anomalous particle diffusion and Lévy random walk of magnetic field lines in three-dimensional solar wind turbulence. *Plasma Phys. & Controlled Fusion* **47**, B755–B767 (2005).
- [43] Del-Castillo-Negrete, D., Carreras, B. & Lynch, V. Nondiffusive Transport in Plasma Turbulence: A Fractional Diffusion Approach. *Phys. Rev. Lett.* **94**, 065003 (2005).
- [44] Hauff, T., Jenko, F. & Eule, S. Intermediate non-Gaussian transport in plasma core turbulence. *Phys. Plasmas* **14**, 102316 (2007).

## Bibliography

---

- [45] Gustafson, K., Del-Castillo-Negrete, D. & Dorland, W. Finite Larmor radius effects on nondiffusive tracer transport in a zonal flow. *Phys. Plasmas* **15**, 102309 (2008).
- [46] Mier, J., Sánchez, R., García, L., Carreras, B. & Newman, D. Characterization of Nondiffusive Transport in Plasma Turbulence via a Novel Lagrangian Method. *Phys. Rev. Lett.* **101**, 165001 (2008).
- [47] Gustafson, K., Ricci, P., Furno, I. & Fasoli, A. Nondiffusive suprathreshold ion transport in simple magnetized toroidal plasmas. *Phys. Rev. Lett.* **108**, 035006 (2012).
- [48] Fermi, E. On the Origin of the Cosmic Radiation. *Physical Review* **75**, 1169–1174 (1949).
- [49] Perri, S. & Zimbardo, G. Ion Superdiffusion At the Solar Wind Termination Shock. *The Astrophysical Journal* **693**, L118–L121 (2009).
- [50] Perri, S. & Zimbardo, G. Ion and electron superdiffusive transport in the interplanetary space. *Adv. Space Res.* **44**, 465–470 (2009).
- [51] Perri, S. & Zimbardo, G. Superdiffusive Shock Acceleration. *Astrophys. J.* **750**, 87 (2012).
- [52] Stage, M. D., Allen, G. E., Houck, J. C. & Davis, J. E. Cosmic-ray diffusion near the Bohm limit in the Cassiopeia A supernova remnant. *Nature Phys.* **2**, 614–619 (2006).
- [53] Perri, S. & Zimbardo, G. Evidence of Superdiffusive Transport of Electrons Accelerated at Interplanetary Shocks. *The Astrophysical Journal* **671**, L177–L180 (2007).
- [54] Pommois, P., Zimbardo, G. & Veltri, P. Anomalous, non-Gaussian transport of charged particles in anisotropic magnetic turbulence. *Phys. Plasmas* **14**, 012311 (2007).
- [55] Trotta, E. M. & Zimbardo, G. Quasi-ballistic and superdiffusive transport for impulsive solar particle events. *Astronomy & Astrophysics* **530**, A130 (2011).
- [56] Perrone, D. *et al.* Nonclassical Transport and Particle-Field Coupling: from Laboratory Plasmas to the Solar Wind. *Space Sci. Rev.* **178**, 233–270 (2013).
- [57] Uchaikin, V. V. Fractional phenomenology of cosmic ray anomalous diffusion. *Physics-Uspekhi* **56**, 1074–1119 (2013).
- [58] Shi, Q. Q. *et al.* Solar wind entry into the high-latitude terrestrial magnetosphere during geomagnetically quiet times. *Nat. Commun.* **4**, 1466 (2013).
- [59] Brockmann, D., Hufnagel, L. & Geisel, T. The scaling laws of human travel. *Nature* **439**, 462–5 (2006).
- [60] Song, C., Koren, T., Wang, P. & Barabási, A.-L. Modelling the scaling properties of human mobility. *Nature Phys.* **6**, 818–823 (2010).
- [61] Caspi, A., Granek, R. & Elbaum, M. Enhanced diffusion in active intracellular transport. *Phys. Rev. Lett.* **85**, 5655–8 (2000).

- [62] Lawrence, J., Cadavid, A., Ruzmaikin, A. & Berger, T. Spatiotemporal Scaling of Solar Surface Flows. *Phys. Rev. Lett.* **86**, 5894–5897 (2001).
- [63] Scher, H. & Montroll, E. Anomalous transit-time dispersion in amorphous solids. *Phys. Rev. B* **12**, 2455–2477 (1975).
- [64] Kirchner, J., Feng, X. & Neal, C. Fractal stream chemistry and its implications for contaminant transport in catchments. *Nature* **403**, 524–7 (2000).
- [65] Ayala-Orozco, B. *et al.* Lévy walk patterns in the foraging movements of spider monkeys (*Ateles geoffroyi*). *Behavioral Ecology and Sociobiology* **55**, 223–230 (2004).
- [66] Eliazar, I. & Klafter, J. Anomalous is ubiquitous. *Annals of Physics* **326**, 2517–2531 (2011).
- [67] Gustafson, K., Ricci, P., Bovet, A., Furno, I. & Fasoli, A. Suprathermal ion transport in simple magnetized torus configurations. *Phys. Plasmas* **19**, 062306 (2012).
- [68] Plyushchev, G. *Interaction of supra-thermal ions with turbulence in a magnetized toroidal plasma*. Ph.D. thesis, Lausanne (2009).
- [69] Bovet, A., Fasoli, A., Gustafson, K., Ricci, P. & Furno, I. Non-diffusive transport regimes for suprathermal ions in turbulent plasmas. *submitted to Phys. Rev. Lett.* (2015).
- [70] Johnsen, H., Pécseli, H. L. & Trulsen, J. Conditional eddies in plasma turbulence. *Phys. Fluids* **30**, 2239–2254 (1987).
- [71] Furno, I. *et al.* Mechanism for blob generation in the torpex toroidal plasma. *Phys. Plasmas* **15**, 055903 (2008).
- [72] Fasoli, A. *et al.* Basic investigations of electrostatic turbulence and its interaction with plasma and suprathermal ions in a simple magnetized toroidal plasma. *Nucl. Fusion* **53**, 063013 (2013).
- [73] Müller, S. *Turbulence in basic toroidal plasmas*. Ph.D. thesis, SB, Lausanne (2007).
- [74] Avino, E., Fasoli, A. & Furno, I. The new TORPEX in-vessel toroidal conductor for the generation of a poloidal magnetic field. *Rev. Sci. Inst.* **85** (2014).
- [75] Podestà, M. *et al.* Plasma production by low-field side injection of electron cyclotron waves in a simple magnetized torus. *Plasma Phys. & Controlled Fusion* **47**, 1989–2002 (2005).
- [76] Podestà, M. *Plasma production and transport in a simple magnetised toroidal plasma*. Ph.D. thesis, SB, Lausanne (2007).
- [77] Furno, I. *et al.* Direct Two-Dimensional Measurements of the Field-Aligned Current Associated with Plasma Blobs. *Phys. Rev. Lett.* **106**, 245001 (2011).

## Bibliography

---

- [78] Iraj, D., Furno, I., Fasoli, A. & Theiler, C. Imaging of turbulent structures and tomographic reconstruction of TORPEX plasma emissivity. *Phys. Plasmas* **17**, 122304 (2010).
- [79] Iraj, D., Furno, I. & Fasoli, A. Fast Imaging of Blob Motion in TORPEX Plasmas. *IEEE Transactions on Plasma Science* **39**, 3010–3011 (2011).
- [80] Iraj, D. *Fast Imaging of Turbulent Plasmas in the TORPEX Device*. Ph.D. thesis, SB, Lausanne (2011).
- [81] Hutchinson, I. *Principles of Plasma Diagnostics* (Cambridge University Press, 2005).
- [82] Labit, B. *et al.* Statistical properties of electrostatic turbulence in toroidal magnetized plasmas. *Plasma Phys. & Controlled Fusion* **49**, B281–B290 (2007).
- [83] Rajković, M., Škorić, M., Sølina, K. & Antar, G. Characterization of local turbulence in magnetic confinement devices. *Nucl. Fusion* **48**, 024016 (2008).
- [84] Theiler, C. G. *Basic Investigation of Turbulent Structures and Blobs of Relevance for Magnetic Fusion Plasmas*. Ph.D. thesis, SB, Lausanne (2011).
- [85] Theiler, C., Furno, I., Kuenlin, A., Marmillod, P. & Fasoli, A. Practical solutions for reliable triple probe measurements in magnetized plasmas. *Rev. Sci. Instr.* **82**, 013504 (2011).
- [86] Ricci, P., Rogers, B. N. & Brunner, S. High- and Low-Confinement Modes in Simple Magnetized Toroidal Plasmas. *Phys. Rev. Lett.* **100**, 225002 (2008).
- [87] Ricci, P. & Rogers, B. N. Three-dimensional fluid simulations of a simple magnetized toroidal plasma. *Phys. Plasmas* **16**, 092307 (2009).
- [88] Ricci, P. & Rogers, B. N. Transport scaling in interchange-driven toroidal plasmas. *Phys. Plasmas* **16**, 062303 (2009).
- [89] Ricci, P. & Rogers, B. N. Turbulence Phase Space in Simple Magnetized Toroidal Plasmas. *Phys. Rev. Lett.* **104**, 1–4 (2010).
- [90] Ricci, P. *et al.* Langmuir probe-based observables for plasma-turbulence code validation and application to the torpex basic plasma physics experiment. *Phys. Plasmas* **16**, 055703 (2009).
- [91] Ricci, P. *et al.* Methodology for turbulence code validation: Quantification of simulation-experiment agreement and application to the TORPEX experiment. *Phys. Plasmas* **18**, 032109 (2011).
- [92] Müller, S. H. *et al.* Basic turbulence studies on TORPEX and challenges in the theory-experiment comparison. *Phys. Plasmas* **12**, 090906 (2005).
- [93] Park, J. *et al.* Field-aligned current associated with low-latitude plasma blobs as observed by the CHAMP satellite. *Annales Geophysicae* **28**, 697–703 (2010).

- 
- [94] Kirk, A. *et al.* Evolution of filament structures during edge-localized modes in the mst tokamak. *Phys. Rev. Lett.* **96**, 185001 (2006).
- [95] Theiler, C. *et al.* Blob motion and control in simple magnetized plasmas. *Phys. Plasmas* **18**, 55901 (2011).
- [96] Furno, I. *et al.* Experimental Observation of the Blob-Generation Mechanism from Interchange Waves in a Plasma. *Phys. Rev. Lett.* **100**, 055004 (2008).
- [97] Theiler, C. *et al.* The role of the density gradient on intermittent cross-field transport events in a simple magnetized toroidal plasma. *Phys. Plasmas* **15**, 42303 (2008).
- [98] Podestà, M. *et al.* Cross-field transport by instabilities and blobs in a magnetized toroidal plasma. *Phys. Rev. Lett.* **101**, 045001 (2008).
- [99] Diallo, A. *et al.* Dynamics of Plasma Blobs in a Shear Flow. *Phys. Rev. Lett.* **101**, 10–13 (2008).
- [100] Theiler, C. *et al.* Cross-Field Motion of Plasma Blobs in an Open Magnetic Field Line Configuration. *Phys. Rev. Lett.* **103**, 65001 (2009).
- [101] Müller, S. H. *et al.* Studies of blob formation, propagation and transport mechanisms in basic experimental plasmas (torpex and csdx). *Plasma Phys. & Controlled Fusion* **51**, 055020 (2009).
- [102] Plyushchev, G. *et al.* Fast ion source and detector for investigating the interaction of turbulence with suprathermal ions in a low temperature toroidal plasma. *Rev. Sci. Inst.* **77**, 10F503 (2006).
- [103] Zhang, Y. *et al.* Lithium ion sources for investigations of fast ion transport in magnetized plasmas. *Rev. Sci. Inst.* **78**, 013302 (2007).
- [104] HeatWave Labs Inc., Alkali Ion Source documentation. <http://www.cathode.com/pdf/tb-118.pdf>.
- [105] Murphy, E. L. & Good, R. H. Thermionic emission, field emission, and the transition region. *Phys. Rev.* **102**, 1464–1473 (1956).
- [106] Atracsys LCC, AccuTrack documentation. [http://atracsys.com/pdfs/atracsys\\_tracking\\_systems.pdf](http://atracsys.com/pdfs/atracsys_tracking_systems.pdf).
- [107] Baloniak, T., Reuter, R., Flötgen, C. & von Keudell, A. Calibration of a miniaturized retarding field analyzer for low-temperature plasmas: geometrical transparency and collisional effects. *Journal of Physics D: Applied Physics* **43**, 055203 (2010).
- [108] Knudsen, W. Evaluation and demonstration of the use of retarding potential analyzers for measuring several ionospheric quantities. *Journal of Geophysical Research* **71**, 4669–4678 (1966).

## Bibliography

---

- [109] Böhm, C. & Perrin, J. J. Retarding-field analyzer for measurements of ion energy distributions and secondary electron emission coefficients in low-pressure radio frequency discharges. *Rev. Sci. Instr.* **64**, 31 (1993).
- [110] Temple, P. A. An introduction to phase-sensitive amplifiers: An inexpensive student instrument. *Amer. J. Phys.* **43**, 801–807 (1975).
- [111] Sibson, R. *Interpreting Multivariate Data*, chap. A brief description of natural neighbour interpolation, 21–36 (Chichester, 1981).
- [112] Einstein, A. On the movement of small particles suspended in stationary liquids required by the molecular-kinetic theory of heat. *Annalen der Physik* **17**, 16 (1905).
- [113] von Smoluchowski, M. Zur kinetischen theorie der brownschen molekularbewegung und der suspensionen. *Annalen der Physik* **326**, 756–780 (1906).
- [114] Langevin, P. On the Theory of Brownian Motion. *C. R. Acad. Sci. (Paris)* **146**, 530–533 (1908).
- [115] Hinton, F & Hazeltine, R. Theory of plasma transport in toroidal confinement systems. *Reviews of Modern Physics* **48**, 239–308 (1976).
- [116] Vedenov, A. A. Quasi-linear theory of a plasma. *The Soviet Journal of Atomic Energy* **13**, 591–612 (1963).
- [117] Vernay, T. *et al.* Global Gyrokinetic Simulations of TEM Microturbulence. *Plasma Phys. & Controlled Fusion* **55**, 074016 (2013).
- [118] Villard, L. *et al.* Global Gyrokinetic ITG Turbulence Simulations of ITER. *Plasma Phys. & Controlled Fusion* **55**, 074016 (2013).
- [119] Coda, S. T. T. T. Overview of Recent and Current Research on the TCV Tokamak. *Nucl. Fusion* (2012).
- [120] Sánchez, R., Newman, D. & Carreras, B. Waiting-Time Statistics of Self-Organized-Criticality Systems. *Phys. Rev. Lett.* **88**, 068302 (2002).
- [121] Bakunin, O. G. Diffusion equations and turbulent transport. *Plasma Physics Reports* **29**, 955–970 (2003).
- [122] Sánchez, R., Carreras, B., Newman, D., Lynch, V. & van Milligen, B. Renormalization of tracer turbulence leading to fractional differential equations. *Phys. Rev. E* **74**, 1–11 (2006).
- [123] del Castillo-Negrete, D. Nonlocal transport in the presence of transport barriers. *Bulletin of the American Physical Society* **58** (2013).

- 
- [124] Pedrosa, M. A. *et al.* Empirical similarity of frequency spectra of the edge-plasma fluctuations in toroidal magnetic-confinement systems. *Phys. Rev. Lett.* **82**, 3621–3624 (1999).
- [125] Carreras, B. A. *et al.* Experimental evidence of long-range correlations and self-similarity in plasma fluctuations. *Phys. Plasmas* **6**, 1885 (1999).
- [126] Samorodnitsky, G. & Taqqu, M. S. *Stable Non-Gaussian Random Processes: Stochastic Models with Infinite Variance* (New York, Chapman and Hall, 1994).
- [127] Metzler, R. & Klafter, J. The random walk's guide to anomalous diffusion: a fractional dynamics approach. *Phys. Rep.* **339**, 1–77 (2000).
- [128] Metzler, R. & Klafter, J. The restaurant at the end of the random walk: recent developments in the description of anomalous transport by fractional dynamics. *Journal of Physics A: Mathematical and General* **37**, R161–R208 (2004).
- [129] Mainardi, F., Luchko, Y. & Gianni, P. The fundamental solution of the space-time fractional diffusion equation. *Fractional Calculus and Applied Analysis*, Vol. **4**, 153–192 (2001). 0702419v1.
- [130] Perrin, J. *Les Atomes* (Paris, Félix Alcan, Paris, 1913).
- [131] Philibert, J. One and a half century of diffusion: Fick, Einstein, before and beyond. *Diffusion Fundamentals* **2**, 1–10 (2005).
- [132] Mandelbrot, B. B. *The Fractal Geometry of Nature* (New York, W. H. Freeman and Company, New York, 1983).
- [133] Greco, A. *et al.* Ion transport and Lévy random walk across the magnetopause in the presence of magnetic turbulence. *Journal of Geophysical Research* **108**, 1395 (2003).
- [134] Carreras, B. a., Lynch, V. E. & Zaslavsky, G. M. Anomalous diffusion and exit time distribution of particle tracers in plasma turbulence model. *Phys. Plasmas* **8**, 5096 (2001).
- [135] Mandelbrot, B. B. & Wallis, J. R. Noah, Joseph, and operational hydrology. *Water Resources Research* **4**, 909 (1968).
- [136] Khintchine, A. & Lévy, P. Comptes rendus hebdomadaires des séances de l' Académie des sciences / publiés ... par MM. les secrétaires. *Comptes rendus hebdomadaires des séances de l' Académie des sciences* **202**, 374–376 (1936).
- [137] Bouchaud, J.-P. & Georges, A. Anomalous diffusion in disordered media: Statistical mechanisms, models and physical applications. *Physics Reports* **195**, 127–293 (1990).
- [138] Scafetta, N. & West, B. Solar Flare Intermittency and the Earth's Temperature Anomalies. *Phys. Rev. Lett.* **90**, 248701 (2003).

## Bibliography

---

- [139] Montroll, E. W. & Weiss, G. H. Random Walks on Lattices. II. *Journal of Mathematical Physics* **6**, 167 (1965).
- [140] Klafter, J., Blumen, A. & Shlesinger, M. F. Stochastic pathway to anomalous diffusion. *Phys. Rev. A* **35**, 3081–3085 (1987).
- [141] Sánchez, R., Carreras, B. & van Milligen, B. Fluid limit of nonintegrable continuous-time random walks in terms of fractional differential equations. *Physical Review E* **71**, 011111 (2005).
- [142] Saenko, V. V. New approach to statistical description of fluctuating particle fluxes. *Plasma Physics Reports* **35**, 1–13 (2009).
- [143] Reynolds, A. M. Scale-free animal movement patterns: Lévy walks outperform fractional Brownian motions and fractional Lévy motions in random search scenarios. *Journal of Physics A: Mathematical and Theoretical* **42**, 434006 (2009).
- [144] Sokolov, I. & Metzler, R. Towards deterministic equations for Lévy walks: The fractional material derivative. *Physical Review E* **67**, 010101 (2003).
- [145] Gustafson, K. & Ricci, P. Lévy walk description of suprathermal ion transport. *Phys. Plasmas* **19**, 032304 (2012).
- [146] Kubo, R. The fluctuation-dissipation theorem. *Reports on Progress in Physics* **29**, 255–284 (1966).
- [147] Nyquist, H. Thermal Agitation of Electric Charge in Conductors. *Physical Review* **32**, 110–113 (1928).
- [148] Callen, H. & Welton, T. Irreversibility and Generalized Noise. *Physical Review* **83**, 34–40 (1951).
- [149] Porr, J., Wang, K. & Masoliver, J. Generalized Langevin equations: Anomalous diffusion and probability distributions. *Physical review. E, Statistical physics, plasmas, fluids, and related interdisciplinary topics* **53**, 5872–5881 (1996).
- [150] Mandelbrot, B. B. & Van Ness, J. W. Fractional Brownian Motions, Fractional Noises and Applications. *SIAM Review* **10**, 422–437 (1968).
- [151] Hurst, H. E. Long-term Storage Capacity of Reservoirs. *Transactions of the American Society of Civil Engineers* **116**, 770 (1951).
- [152] Calvo, I. & Sánchez, R. The path integral formulation of fractional Brownian motion for the general Hurst exponent. *Journal of Physics A: Mathematical and Theoretical* **41**, 282002 (2008).
- [153] Jeon, J.-H. & Metzler, R. Fractional Brownian motion and motion governed by the fractional Langevin equation in confined geometries. *Physical Review E* **81**, 021103 (2010).

- [154] Mainardi, F., Mura, A. & Pagnini, G. The M-Wright Function in Time-Fractional Diffusion Processes: A Tutorial Survey. *International Journal of Differential Equations* **2010**, 1–29 (2010).
- [155] Laskin, N., Lambadaris, I., Harmantzis, F. C. & Devetsikiotis, M. Fractional Lévy motion and its application to network traffic modeling. *Computer Networks* **40**, 363–375 (2002).
- [156] Calvo, I., Sánchez, R. & Carreras, B. a. Fractional Lévy motion through path integrals. *J. Phys. A:Math. Theor.* **42**, 055003 (2009).
- [157] Podlubny, I. *Fractional differential equations* (San Diego, Academic Press, 1999).
- [158] Wersal, C., Ricci, P., Halpern, F. D. & Riva, F. A kinetic neutral atom model for tokamak SOL turbulence simulations. <http://infoscience.epfl.ch/record/201710> (2014).
- [159] Braginskii, S. Transport processes in a plasma. *Reviews of Plasma Physics* 205–311 (1965).
- [160] Zeiler, A., Drake, J. & Rogers, B. Nonlinear reduced Braginskii equations with ion thermal dynamics in toroidal plasma. *Phys. Plasmas* **4**, 2134–2138 (1997).
- [161] Loizu, J. *The role of the sheath in magnetized plasma turbulence and flows*. Ph.D. thesis, SB, Lausanne (2013).
- [162] Fasoli, A., Skiff, F., Kleiber, R., Tran, M. M. & Paris, P. P. Dynamical chaos of plasma ions in electrostatic waves. *Phys. Rev. Lett.* **70**, 303–306 (1993).
- [163] Huang, R. *et al.* Direct observation of the full transition from ballistic to diffusive Brownian motion in a liquid. *Nature Phys.* **7**, 576–580 (2011).
- [164] Howes, G. G. *et al.* Astrophysical Gyrokinetics: Basic Equations and Linear Theory. *The Astrophysical Journal* **651**, 590–614 (2006).
- [165] Sánchez, R., Newman, D., Leboeuf, J.-N., Decyk, V. & Carreras, B. Nature of Transport across Sheared Zonal Flows in Electrostatic Ion-Temperature-Gradient Gyrokinetic Plasma Turbulence. *Phys. Rev. Lett.* **101**, 205002 (2008).
- [166] Gamarino, M. Characterization of a fast ion beam transport in the basic plasma physics experiment TORPEX (2013).
- [167] Bovet, A. *et al.* Transport equation describing fractional Lévy motion of suprathermal ions in TORPEX. *Nucl. Fusion* **54**, 104009 (2014).
- [168] Gorenflo, R. & Mainardi, F. Approximation of Lévy-Feller Diffusion by Random Walk. *Journal for Analysis and its Applications* **18**, 231–246 (1999).
- [169] Sato, K. *Lévy Processes and Infinitely Divisible Distributions*. Cambridge Studies in Advanced Mathematics (Cambridge University Press, 1999).

## Bibliography

---

- [170] Xiao, Y. *Fractal Geometry and Applications: Multifractals, probability and statistical mechanics, applications*, chap. Random Fractals and Markov Processes, 261–339 (American Mathematical Soc., 2004).
- [171] Blumen, A., Klafter, J. & Zumofen, G. A stochastic approach to enhanced diffusion: Lévy walks. *EPL (Europhysics Letters)* **223** (1990).
- [172] Cartea, A. & Del-Castillo-Negrete, D. Fluid limit of the continuous-time random walk with general Lévy jump distribution functions. *Physical Review E* **76**, 041105 (2007).
- [173] Del-Castillo-Negrete, D. Truncation effects in superdiffusive front propagation with Lévy flights. *Physical Review E* **79**, 031120 (2009).
- [174] del Castillo-Negrete, D. Private communication (2014).
- [175] D’Ippolito, D. a., Myra, J. R. & Zweben, S. J. Convective transport by intermittent blob-filaments: Comparison of theory and experiment. *Phys. Plasmas* **18**, 060501 (2011).
- [176] Halpern, F. D. *et al.* Three-dimensional simulations of blob dynamics in a simple magnetized torus. *Phys. Plasmas* **21**, 022305 (2014).
- [177] Carreras, B. A. *et al.* Intermittency of plasma edge fluctuation data: Multifractal analysis. *Phys. Plasmas* **7**, 3278 (2000).
- [178] Frisch, U. *Turbulence: the legacy of A. N. Kolmogorov* (Cambridge university press, 1995).
- [179] Hauff, T., Pueschel, M., Dannert, T. & Jenko, F. Electrostatic and magnetic transport of energetic ions in turbulent plasmas. *Phys. Rev. Lett.* **102**, 075004 (2009).
- [180] Mazur, J. E. *et al.* Interplanetary Magnetic Field Line Mixing Deduced from Impulsive Solar Flare Particles. *The Astrophysical Journal* **532**, L79–L82 (2000).
- [181] Giacalone, J., Jokipii, J. R. & Mazur, J. E. Small-scale Gradients and Large-scale Diffusion of Charged Particles in the Heliospheric Magnetic Field. *The Astrophysical Journal* **532**, L75–L78 (2000).
- [182] Zimbardo, G., Pommois, P. & Veltri, P. Magnetic flux tube evolution in solar wind anisotropic magnetic turbulence. *Journal of Geophysical Research* **109**, A02113 (2004).
- [183] Guo, F. & Giacalone, J. Small-scale gradients of charged particles in the heliospheric magnetic field. *The Astrophysical Journal* **780**, 16 (2014).
- [184] Yu, C. X., Gilmore, M., Peebles, W. a. & Rhodes, T. L. Structure function analysis of long-range correlations in plasma turbulence. *Phys. Plasmas* **10**, 2772 (2003).
- [185] Zolotarev, V. M. *One-dimensional stable distributions* (Providence, Rhode Island, American Mathematical Society, 1986).

- [186] Nolan, J. P. Numerical calculation of stable densities and distribution functions. *Communications in Statistics. Stochastic Models* **13**, 759–774 (1997).
- [187] Caputo, M. Linear Models of Dissipation whose Q is almost Frequency Independent–II. *Geophysical Journal International* **13**, 529–539 (1967).
- [188] Haber, R., Prehl, J., Herrmann, H. & Hoffmann, K. H. Diffusion of oriented particles in porous media. *Physics Letters A* **377**, 2840–2845 (2013).
- [189] Gorenflo, R. & Mainardi, F. Fractional Calculus: Integral and Differential Equations of Fractional Order. *arXiv preprint arXiv:0805.3823* 56 (2008). 0805.3823.
- [190] Huba, J. *NRL Plasma Formulary* (Office of Naval Research, 2013).



# Acknowledgements

A Thesis is like a travel in a foreign country in many ways. I was very fortunate to be surrounded by great people that guided me when I was lost and helped me make fascinating discoveries. I wish to thank my supervisors, Ivo Furno and Ambrogio Fasoli, for their invaluable guidance during this travel. I greatly enjoyed and learned from the many discussions with Ivo. His vast knowledge and his constant curiosity was a great source of motivation that made the possibilities seem almost limitless. Ambrogio's profound understanding of the field was a great help. He was always encouraging with precise and pertinent explanations. I also enjoyed very much assisting him in his teaching of the Physique Générale II course during four years. I wish to thank Paolo Ricci for being like my third supervisor, always taking the time to rigorously answer my questions about the theory and the numerical simulations. I am also indebted to Kyle Gustafson for his help at the beginning of my Thesis. He was very kind and patient while he explained me all the details of the numerical model he developed. I also thank the technical team of the CRPP for its essential support, Blaise, Christian, Jérémie, Matthieu, Nelson, Omar, Philippe, Pierre, Steve, Ugo and William. I am grateful to the CRPP secretaries, Edith, Heidi and Roxanne, for their effectiveness in reducing my administrative hassle.

It was a real pleasure to interact daily with the talented and passionate members of the TORPEX team. I am particularly grateful to Christian Theiler, Fabio Avino and Joaquim Loizu. Interesting discussions, mutual assistance and a positive spirit made these years not only intellectually rewarding but also fun.

I am also thankful to my other colleagues and friends, David, Falk, Federico, Jonathan Faustin, Jonathan Rossel, Julien, Josef, Karim, Thibault, Wouter and all the others. The many interesting discussions and laughs that we shared over coffees (or beers) greatly contributed to the exceptional work atmosphere at the CRPP.

I wish to sincerely thank my family for their unstinting care and support. Many thanks to Guillaume Lammers, Sébastien Boutinard Rouelle, Fanny Guex and all my other friends from Lausanne for their unconditional support. Finally, I thank Pierrine Auberson for always putting a smile on my face.

*Lausanne, 30 January 2015*

A. B.



Alexandre Bovet  
Ch. des Fleurettes 32  
1007 Lausanne  
Switzerland

[alexandre.bovet@gmail.com](mailto:alexandre.bovet@gmail.com)  
[people.epfl.ch/alexandre.bovet](http://people.epfl.ch/alexandre.bovet)



Born in Lausanne, Switzerland  
Sept, 28, 1984  
Swiss

## Education

Jan. 13, 2015

### PhD defense

2010 – 2015

### PhD in Physics

École Polytechnique Fédérale de Lausanne (EPFL)  
Centre de Recherche en Physique des Plasmas (CRPP)

2007 - 2009

### Master of Science (MSc) in Physics

École Polytechnique Fédérale de Lausanne (EPFL)  
Master's Thesis at the United Kingdom Atomic Energy Authority (UKAEA),  
Culham, Oxford.  
*Numerical simulation of the anomalous diffusion of fast ions in the presence of fishbone instabilities in tokamaks.*

2004 - 2007

### Bachelor of Science (BSc) in Physics

École Polytechnique Fédérale de Lausanne (EPFL)

## Professional Experience

2007 – 2014

### Teaching Assistant (EPFL)

EPFL, Lausanne, Switzerland

Sep. 2009 – June 2010

### Physics Teacher in a secondary school (Cameroon)

For my civilian service, I taught physics in a secondary school of a deprived neighborhood of the biggest city of Cameroon.

## Publications

### First author

A. Bovet, A. Fasoli, K. Gustafson, P. Ricci, P. & I. Furno, **Non-diffusive transport regimes for suprathermal ions in turbulent plasmas**. Submitted to *Phys. Rev. Lett.*

A. Bovet, A. Fasoli & I. Furno, **Time-resolved measurements of suprathermal ion transport induced by intermittent plasma blob-filaments**, *Phys. Rev. Lett.*, vol. 113, num. 22, p. 225001, 2014

A. Bovet, M. Gamarino, I. Furno, P. Ricci, A. Fasoli, K. Gustafson, D. E. Newman and R. Sanchez. **Transport equation describing fractional Lévy motion of suprathermal ions in TORPEX**. *Nucl. Fusion*, vol. 54, num. 10, p. 104009, 2014.

A. Bovet, I. Furno, A. Fasoli, K. Gustafson & P. Ricci, **Three-dimensional measurements of non-diffusive fast ion transport in TORPEX**, in *Plasma Phys. Controlled Fusion*, vol. 55, num. 12, p. 124021, 2013.

A. Bovet, I. Furno, A. Fasoli, K. Gustafson & P. Ricci. **Investigation of fast ion transport in TORPEX**, in *Nucl. Fusion*, vol. 52, num. 9, p. 094017, 2012.

## Co-author

A. Fasoli, F. Avino, A. Bovet, I. Furno and K. Gustafson et al. **Basic investigations of electrostatic turbulence and its interaction with plasma and suprathermal ions in a simple magnetized toroidal plasma**, in *Nuclear Fusion*, vol. 53, num. 6, p. 063013, 2013.

W. W. Heidbrink, H. Boehmer, R. McWilliams, A. Preiwisch and Y. Zhang et al. **Measurements of interactions between waves and energetic ions in basic plasma experiments**, in *Plasma Physics and Controlled Fusion*, vol. 54, num. 12, p. 124007, 2012.

K. Gustafson, P. Ricci, A. Bovet, I. Furno and A. Fasoli. **Suprathermal ion transport in simple magnetized torus configurations**, in *Physics of Plasmas*, vol. 19, num. 6, p. 062306, 2012.

## Book

Perrone, D. et al. (2013). **Nonclassical Transport and Particle-Field Coupling: from Laboratory Plasmas to the Solar Wind**. In Balogh, A., Bykov, A., Cargill, P., Dendy, R., Dudok de Wit, T., Raymond, J. (Eds.), *Microphysics of Cosmic Plasmas* (pp 157-194 ). Springer.

## Conferences

### Oral

A. Bovet, F. Avino, A. Fasoli, I. Furno, K. Gustafson and P. Ricci, **Non-diffusive suprathermal ion transport associated with blobs in TORPEX plasmas**, 56th Annual Meeting of the APS Division of Plasma Physics Volume 59, Number 15, New Orleans, Louisiana, USA, October 27–31, 2014

### Invited Speaker

A. Bovet, F. Avino, A. Fasoli, I. Furno, K. Gustafson, J. Loizu and P. Ricci, **Experimental and numerical studies of suprathermal ion transport**, 40th European Physical Society Conference on Plasma, Espoo, Helsinki, Finland, July 1-5, 2013

### Student Poster Prize

A. Bovet, A. Fasoli, I. Furno, K. Gustafson and P. Ricci. **Investigation of suprathermal ion transport in TORPEX**. 39th EPS Conference on Plasma Physics, Stockholm, Sweden, 2012.

## Skills

### Languages

French (Mother tongue), English (Advanced), German (Basic knowledge)

### Softwares

Linux, Windows, MacOS, Office Suite, Adobe Suite, LaTeX, Emacs, Vim, Gimp

### 3D/Visualization

Blender, VisIt

### Programming

C++, Fortran, MPI, MATLAB, IDL, Mathematica, netCDF, HDF5